

**Quantitative Assessment of the Effect of Copper Chills on Casting/Chill
Interface Behavior and the Microstructure of Sand Cast A319 Alloy**

by

Farzaneh Farhang Mehr

B.A., Iran University of Science and Technology, 2008

A THESIS SUBMITTED IN PARTIAL FULFILLMENT OF THE REQUIREMENTS FOR
THE DEGREE OF

MASTER OF APPLIED SCIENCE

in

The Faculty of Graduate Studies

(Materials Engineering)

THE UNIVERSITY OF BRITISH COLUMBIA

(Vancouver)

November 2012

© Farzaneh Farhang Mehr, 2012

Abstract

Although the demand for A319 alloy has increased in recent years, thermal fatigue resistance of the alloy is still one of the most important challenges in engine applications, especially in the newer generation of engines in which cylinder spacing has been reduced. According to the previous studies there are several parameters that improve thermal fatigue resistance such as: low SDAS, fine grain size, low porosity level, and low intermetallic content.

Cooling rate has a direct effect on the shape, size, and distribution of the microstructural phases, as well as on the scale of the dendrites, and pore size. High cooling rates can improve thermal fatigue resistance, as a result of fine microstructure and small pore size. On the other hand, thin sections of a mold may not properly fill and “Cold Shuts” may result, if high cooling rates are applied.

One approach to balance these phenomena is to use a water-cooled chill where water cooling is activated part way through the casting sequence. This type of chill causes a lower cooling rate initially, when the filling procedure is occurring, and after filling, the cooling rate increases to reduce the microstructure size. The results show that this method has the potential to both avoid cold shuts and miss-runs and improve the cast microstructure farther into castings remote from the chill.

A mathematical model has been developed in “ANSYS CFX 12.0” to evaluate the effectiveness of this concept quantitatively. The model simulates the behavior of the Casting/chill interface

and also predicts the cooling rates resulting from different casting conditions when using solid chill and water-cooled chill.

Table of Contents

Abstract	ii
Table of Contents	iv
List of Tables	vi
List of Figures	vii
Acknowledgment.....	xiii
Dedication	xiv
1. Introduction.....	1
2. Literature review	6
2.1. Bonded Sand Precision Casting	6
2.2. Factors Influencing the Fatigue Performance of Cast Components	8
2.3. Porosity	11
2.4. The Solidification Sequence of A319 Including Nucleation and Growth Processes in Solidification	13
2.5. Chill technology	21
2.6. Casting/Mold Interfacial Heat Transfer	24
2.7. Quantification of Casting/Mold Interfacial Heat Transfer Coefficient.....	26
3. Scope and Objective	32

4.	Experimental Procedure.....	34
4.1.	Experimental Methodology	34
4.2.	Experimental Results and Discussion.....	43
5.	Development of the Computational Model.....	72
6.	Results and Discussion	93
7.	Sensitivity Analysis	119
8.	Summary and Conclusion.....	129
	References	132

List of Tables

Table 1.1: Composition range of A319 Alloy	2
Table 4.1: Composition of A319 alloy	38
Table 4.2: The Conditions of the Castings.....	39
Table 4.3: Metallography procedure.....	42
Table 5.1: Mesh Statistics	78
Table 5.2: Initial conditions of the castings	84
Table 7.1: List of sensitivity analysis factors being investigated	119

List of Figures

Figure 1.1: Top view of 2.0 L cylinder head [28].....	4
Figure 1.2: A picture of V8 engine block [12].....	4
Figure 2.1: Schematic of molding process in sand casting [31]	7
Figure 2.2: Aluminum-Silicon phase diagram [3]	14
Figure 2.3: Nucleation model used in the microscopic calculation of equi-axed solidification. At a given undercooling (a), ΔT_1 , the density of nuclei, n_1 , within the liquid is given by the integral (c) of the distribution (b) [66].	17
Figure 2.4: sketch of ingot structure showing chill zone, columnar zone, equi-axed zone [31] ..	18
Figure 2.5: Schematic summary of single-phase solidification morphology [67].....	19
Figure 2.6: Graph showing a comparison between the modeled heat-transfer coefficient and experimentally determined values for the unidirectional solidification vertically upward of an Al-7%Si alloy casting [81]	30
Figure 2.7: comparison of measured and calculated temperatures within the copper chill at a point 75 mm from the casting-chill interface [81]	31
Figure 4.1: Dimensioned drawing of wedge and riser (all dimensions are in mm).....	34
Figure 4.2.a: Dimensioned drawing of solid chill (all dimensions are in mm)	36
Figure 4.3: The water-cooled and solid chills.....	37
Figure 4.4: The position of the thermocouples used for temperature recording.....	38
Figure 4.5: Water cooling system	40
Figure 4.6: Solidified wedge, water cooled chill condition	41

Figure 4.7: Solidified wedge, solid chill condition.....	41
Figure 4.8: Temperature variation with time for various distances from chill and within the chill for Casting 1.....	45
Figure 4.9: Temperature variation with time for various distances from chill and within the chill for Casting 2.....	45
Figure 4.10: Temperature variation with time for various distances from chill and within the chill for Casting 3.....	46
Figure 4.11: Temperature variation with time for various distances from chill and within the chill for Casting 4.....	46
Figure 4.12: Temperature variation with time at various heights, monitoring the buoyancy effect for Casting 1.....	48
Figure 4.13: Temperature variation with time at various heights, monitoring the buoyancy effect for Casting 2.....	48
Figure 4.14: Temperature variation with time at various heights, monitoring the buoyancy effect for Casting 3.....	49
Figure 4.15: Temperature variation with time at various heights, monitoring the buoyancy effect for Casting 4.....	49
Figure 4.16: Comparison of solid chill condition at 5 mm from chill, varying chill temperature	50
Figure 4.17: Comparison of solid chill condition at 50 mm from chill, varying chill temperature	51
Figure 4.18: Comparison of solid chill condition at 5 mm from chill, varying super heat.....	52
Figure 4.19: Comparison of solid chill condition at 50 mm from chill, varying super heat.....	52
Figure 4.20: Variation in temperature with distance from chill and within the chill.....	54

Figure 4.21: Variation in temperature with distance from chill and within the chill.....	56
Figure 4.22: Variation in temperature with distance from chill and within the chill, for the first 500 seconds.....	56
Figure 4.23: Cooling curve comparison between “Solid chill” and “Standard Water-Cooled chill” conditions.....	57
Figure 4.24: Cooling curve comparison between “Solid chill” and “Standard Water-Cooled chill” conditions.....	58
Figure 4.25: Cooling curve comparison between “Solid chill” and “Standard Water-Cooled chill” conditions.....	58
Figure 4.26: Cooling curve comparison between “Solid chill” and “Delayed Water-Cooled chill” conditions.....	60
Figure 4.27: Cooling curve comparison between “Solid chill” and “Delayed Water-Cooled chill” conditions.....	61
Figure 4.28: Cooling curve comparison between “Solid chill” and “Delayed Water-Cooled chill” conditions.....	61
Figure 4.29: The variation of SDAS with distance from the chill.....	62
Figure 4.30: The variation of SDAS with cooling rate between liquidus and eutectic temperatures.....	65
Figure 4.31: The variation of SDAS with cooling rate between solidus and liquidus temperatures.....	66
Figure 4.32: The microstructure of a) Casting 1 and b) Casting 5 at 5 mm distance from the chill.....	67
Figure 4.33: The microstructure of a) Casting 1 and b) Casting 5 at 10 mm distance from the chill.....	68

Figure 4.34: The microstructure of a) Casting 1 and b) Casting 5 at 30 mm distance from the chill	69
Figure 4.35: The microstructure of a) Casting 1 and b) Casting 5 at 50 mm distance from the chill	70
Figure 4.36: The microstructure of a) Casting 1 and b) Casting 5 at 150 mm distance from the chill	71
Figure 5.1: The meshed geometry of solid chill condition, Z is the vertical axis in the experiments	75
Figure 5.2: The meshed geometry of water-cooled condition, Z is the vertical axis in the experiments	76
Figure 5.3: Fraction solid and fraction liquid as functions of temperature [99]	79
Figure 5.4: Density as a function of temperature [99]	80
Figure 5.5: Modified density vs. temperature graph used in the modeling	80
Figure 5.6: Effective thermal conductivity as a function of temperature [99].....	81
Figure 5.7: Effective thermal conductivity as a function of temperature	82
Figure 5.8: Effective specific heat as a function of temperature	83
Figure 5.9: Effective specific heat as a function of temperature used for modeling	84
Figure 5.10: The schematic of the boundaries defined for the solid chill conditions.....	85
Figure 5.11: The schematic of the boundaries defined for the water cooled chill conditions	86
Figure 5.12: The schematic of the chill/casting interface for both the solid chill, and water cooled chill conditions.....	87
Figure 6.1: Comparison between the experimental data and model predictions	96

Figure 6.2: Comparison between the experimental data and model predictions	96
Figure 6.3: Comparison between the experimental data and model predictions	97
Figure 6.4: Comparison between the experimental data and model predictions	97
Figure 6.5: Comparison between the experimental data and model predictions	98
Figure 6.6: Comparison between the experimental data and model predictions	98
Figure 6.7: Temperature dependent melt-chill interfacial heat transfer coefficient for solid chill conditions	100
Figure 6.8: The temperature variation of the interface at casting and chill domains, and the related IHTC; (a) for the first 50 seconds, (b) for 740 seconds, casting 4.....	103
Figure 6.9: The schematic of the Casting/Chill interface behavior in solid chill conditions.....	104
Figure 6.10: Time dependent melt/chill interfacial heat transfer coefficient for water-cooled conditions	106
Figure 6.11: The temperature variation of the interface at casting domain, and the time dependent IHTC, casting 5	107
Figure 6.12: The schematic of the Casting/Chill interface behavior in standard water-cooled chill condition	108
Figure 6.13: The temperature variation of the interface at casting domain, and the time dependent IHTC, casting 6.....	109
Figure 6.14: The schematic of the Casting/Chill interface behavior in delayed water-cooled chill condition	110
6.15: Comparison between model prediction and experimental data for casting 5	111
Figure 6.16: The variation of the applied IHTC with temperature	112

6.17: Time dependent IHTC comparison Between casting 4 and casting 5	113
Figure 6.18: The variation of IHTC with temperature for casting 4 and casting 5.....	114
6.19: Temperature variation with distance from the chill.....	115
Figure 6.20: Temperature dependent casting/mold heat transfer coefficient	116
Figure 6.21: The temperature of the mold adjacent to the casting as a function of time ($T_{\text{casting/mold}}$).....	116
Figure 6.22: Temperature dependent chill/mold heat transfer coefficient.....	117
Figure 6.23: Temperature of the sand mold adjacent to the solid chill surface as a function of time ($T_{\text{Chill/Mold}}$)	118
Figure 7.1: Sensitivity of thermal model to the temperature dependent chill/casting interfacial heat transfer coefficient.....	121
Figure 7.2: Sensitivity of the thermal model to the time dependent chill/casting interfacial heat transfer coefficient	122
Figure 7.3: Sensitivity of the thermal model to the temperature dependent casting/mold heat transfer coefficient	123
Figure 7.4: Sensitivity of the thermal model to the temperature dependent casting/mold heat transfer coefficient	124
Figure 7.5: Sensitivity of the thermal model to the temperature dependent chill/mold heat transfer coefficient	125
Figure 7.6: Sensitivity of the thermal model to the temperature dependent chill/mold heat transfer coefficient	126
Figure 7.7: Sensitivity of the thermal model to the sand mold temperature.....	127
Figure 7.8: Sensitivity of the thermal model to the sand mold temperature.....	128

Acknowledgment

I would like to express my deepest sense of gratitude to my research supervisor Professor Steve Cockcroft for his kind support, guidance, patience, and encouragement, which inspired me to continue my studies in this field. I would also like to give thanks to Professor Daan Maijer for his great involvement and advice during my studies.

I would like to acknowledge Nematik Canada, the industrial partner of this project, and in particular, Dr. Robert MacKay for providing the experiments with sand molds and A319 ingots.

I am grateful to Dr. Carl Reilly and Zhongkui Zhang for their valuable contributions in all the casting procedures and experimental setup. I am also thankful to my colleagues Dr. Lu Yao and Matt Roy for sharing their rich research experiences at the times of difficulties.

I am thankful to the machine shop technicians, Ross Mcleod, David Torok and Carl Ng who helped to construct the experimental apparatus for the casting procedures. Special thanks to Rudy Cardeno for his assistance to build the water-cooling system setup.

Lastly, I want to express my deepest respect and appreciation to my parents and my sisters, for their strong support and continuous encouragement, without which I couldn't complete my degree.

To:

My Parents

And

My Sisters

1. Introduction

In order to reduce fuel consumption and meet performance requirements there is a growing need in the automotive industry for weight reduction in vehicles. One way to achieve this goal is to make use of light weight alloys as a replacement for conventional iron-based alloys. A good example of this in recent years has been the switch to aluminum alloys for the cylinder heads and engine blocks displacing traditional cast-iron. The widespread commercial adoption of aluminum alloys in automotive power plants has been steady starting first with 4-cylinder engines, then to six-cylinder and finally, more recently, high-powered V8 engines. Among aluminum foundry alloys, A319 is commonly used in engine blocks and cylinder heads of gasoline engines in North America. The success of this heat treatable alloy and its derivatives (nominal composition given below in Table 1.1) stems from its excellent castability, high strength-to-weight ratio, high thermal conductivity, good corrosion resistance and ability to be recycled [1-24]. However, despite good adaptation, there remain additional opportunities and challenges for cast aluminum powertrain components in applications demanding increased fatigue performance. One opportunity lies in adaptation in diesel engine applications – e.g. “Despite having firmly established themselves in this application, aluminum castings are poised for yet future growth, notably in the diesel engine cylinder block area where many designs today are still based on iron” [17]. In addition, the next generation of smaller, high-output, turbo-charged, four-cylinder, gasoline engines require increased fatigue performance, which represents a challenge for aluminum engine block manufacturers.

Table 1.1: Composition range of A319 Alloy¹

Alloying Element	Si	Fe	Cu	Mn	Mg	Zn	Ti	Sr
Balance (Wt%)	8.10- 8.75	0.27- 0.59	2.60- 2.95	0.7 · Fe- 0.44	0.31-0.4	0.4- 0.8	0.12- 0.16	0.004 max

The increased demand for fatigue resistance has initiated a significant effort toward improving the mechanical properties of cast aluminum alloy products [25,26]. In the absence of altering alloy chemistry or heat treatment technology one viable way to improve mechanical performance and in particular fatigue performance is through increasing the cooling rate during solidification [18,27]. According to prior studies, increased cooling rates during solidification can result in reduced Secondary Dendrite Arm Spacing (SDAS), grain size, micro-porosity size distributions, and inter-metallic size distributions all of which result in improved fatigue resistance [2,18,20]. The drawback of this approach is that it requires reduced pour superheat and more aggressive cooling, which tends to result in an increase in the occurrence of cold-shuts. Cold shuts arise during filling of the mold when there is insufficient fluidity in the metal to allow flow into narrow pathways within the mold or the complex mixing (and fusion) of two metal free surfaces when they meet [3]. From the standpoint of overall product quality one would want low initial cooling rates/high super heat to avoid cold-shuts followed by high cooling rates to improve the microstructural qualities identified to enhance fatigue performance. This challenge can potentially be met for cylinder blocks cast using the precision sand casting process by the careful design and placement of a chill within the mold. The chill can be preheated to avoid mis-runs

¹ Chemical composition provided by “Nemak Canada”

and satisfy proper mold filling, then can increase the cooling rate by activating water cooling within the chill after the mold is filled to produce a fine microstructure [17].

When designing automotive casting parts, it is of high importance to have accurate information related to how the alloy solidifies at different cooling rates and to determine the subsequent influences of varying microstructural scale on mechanical properties. This knowledge helps the designer to ensure that the casting will have the desired mechanical properties for its intended application [18]. The complicated geometries of cylinder heads and engine blocks, examples of which are illustrated in Figures 1.1 and 1.2, consist of thick and thin sections of varying distance from the mold. Consequently, the material experiences a range of cooling rates resulting in a range of microstructure sizes and fatigue performance. In order to get a sense of the mechanical property variability many companies, including NemaK Canada, the industrial partner in this project, use a standardized wedge casting in which the narrow end of the wedge is solidified against a chill. The chill is placed within a conventional bonded sand mold, produced according to the standard manufacturing process used to produce precision bonded sand molds for engine blocks. To begin, it makes sense to first test water-cooled chill technology using a standardized wedge mold prior to moving toward a more complex geometry typical of that found within an engine block.

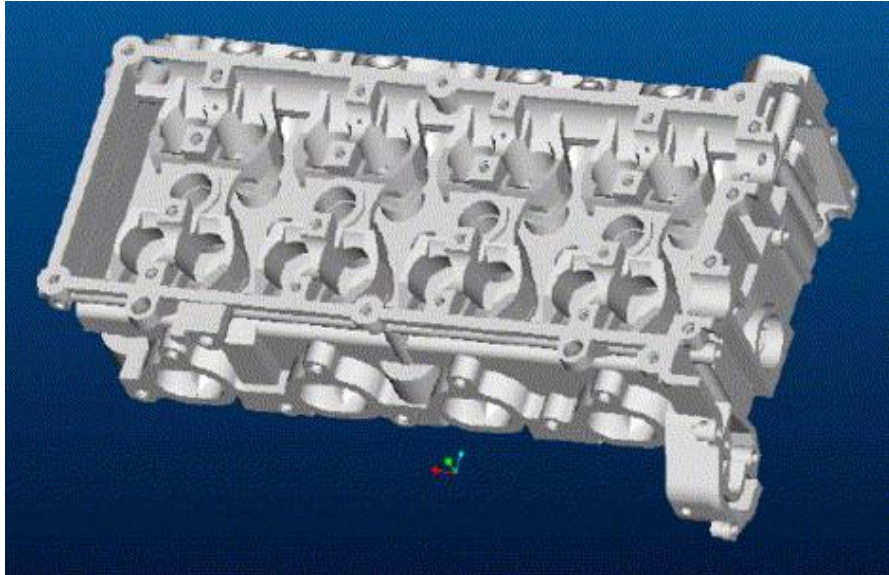


Figure 1.1: Top view of 2.0 L cylinder head [28]

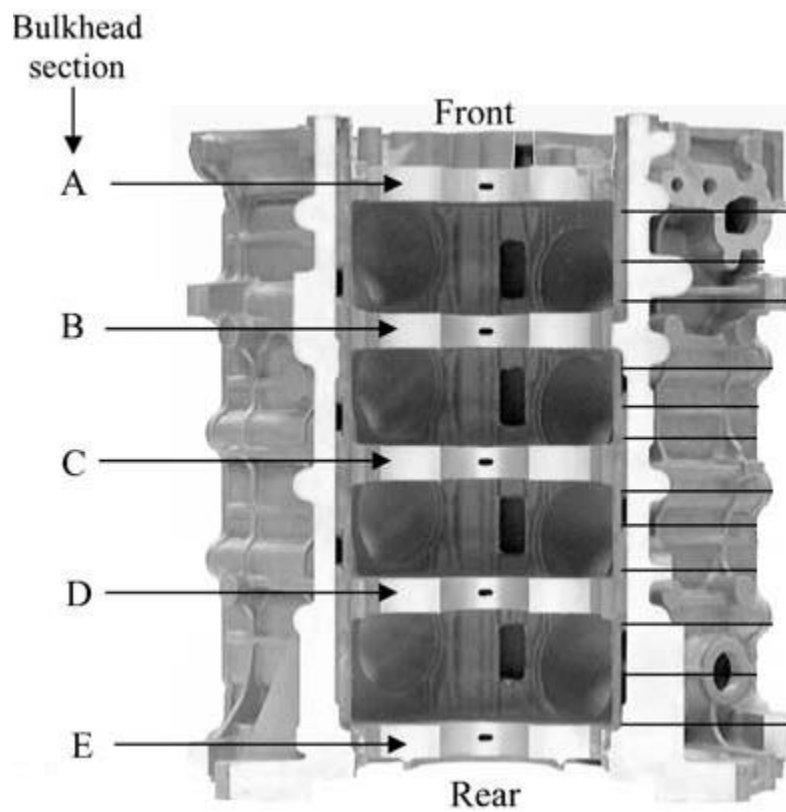


Figure 1.2: A picture of V8 engine block [12]

This research program is focused on determining quantitatively the efficacy of a water-cooled chill in transitioning from a low initial heat transfer rate (chill preheated, no water cooling) to a high heat transfer rate (water cooling) using the standard Nematik wedge-chill mold for assessment. The research program entails using a combination of experimental methods and analysis using a numerical model to conduct a quantitative assessment of the performance of the water-cooled chill. The performance metrics to be quantified include cooling rate variation as a function of time and distance from the chill, the associated microstructure length scale (SDAS) variation with distance from the chill and a quantitative assessment of the behavior of the interface (between the chill and casting) with time.

2. Literature review

Precision sand casting is a flexible casting procedure that is widely used in the production of cylinder heads and engine blocks for the automotive sector. However, owing to recent trends toward higher specific power density in gasoline engines and to light weight diesel engines there is a need to enhance the ability of the precision sand casting process to produce products with a higher fatigue performance. High fatigue performance in thick casting sections, such as a bulkhead in engine blocks, can be achieved by increasing the cooling rate during solidification. Toward this goal the literature will cover the following areas: 1) a review of the precision bonded sand casting; 2) factors influencing the fatigue performance of cast components; 3) the solidification sequence of A319 including nucleation and growth processes in solidification; 4) porosity formation in solidification of cast alloys including shrinkage feeding in solidification of cast alloys; 5) the influence of cooling rate on solidification microstructure morphology; 6) the influence of pour temperature on the solidification of cast alloys including the mechanism for the formation of cold shuts in shape casting processes; and finally 7) heat transport process and techniques for the simulation of heat transfer in casting processes.

2.1. Bonded Sand Precision Casting

Precision sand casting (using silica or zircon type sand) is used extensively in the production of automotive parts such as cylinder heads and engine blocks cast with the A319 alloy [3,5,29]. The advantages of the precision sand casting process include that it is low-cost, it lends itself to automation, and it is highly flexible in the design of the cast parts [30]. Figure 2.1 schematically illustrates a typical mold layup and the resulting final cast product. The two sections, also

illustrated in the figures, show the ability of this process to cast components with varying internal and external geometry.

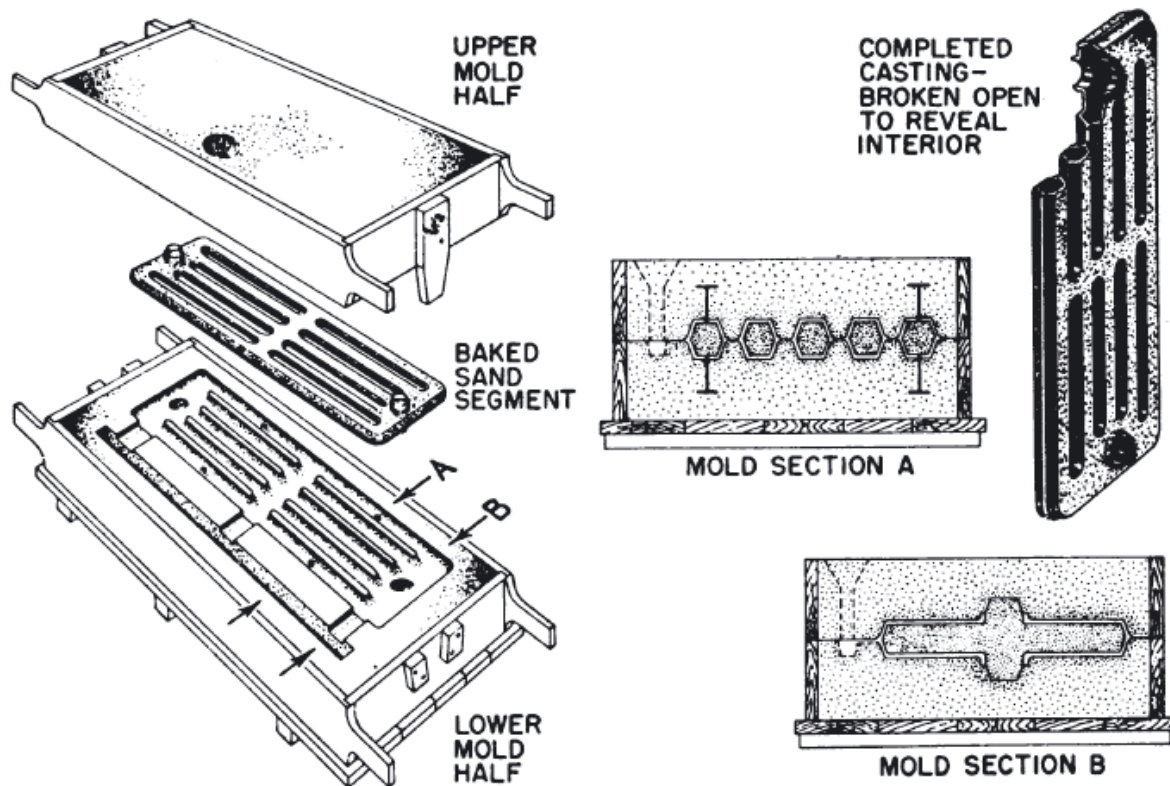


Figure 2.1: Schematic of molding process in sand casting [31]

The sand casting process consists of the following stages:

- i. Fabrication of the mold in silica or zircon sand, which includes the desired pattern to be cast and the gating system to deliver the metal to the mold;
- ii. Pouring
- iii. Solidification and cooling; and
- iv. Removal of the solidified product from the mold [29,30,32].

The resultant product is a raw casting that is then further processed to remove the gating system and then machined to the desired surface quality and component dimensions specified for the part [3,32]. The process allows for the production of intricate shapes with near-net dimensions hence its widespread use for production of engine blocks and cylinder heads [32,33].

Despite many advantages, it suffers from one notable disadvantage namely low heat extraction rates as a result of the relatively low thermal conductivity of sand. For example, the bulkhead section in an engine block experiences the highest cyclic compression and tensile stresses during in service operation, yet material exhibits relatively poorer fatigue performance. This arises because it is typically the thickest in cross-sectional size and experiences relatively slow solidification rates due to the low thermal conductivity of the mold. The relatively slow cooling rates during solidification result in larger SDAS, dendrite cell size distributions and eutectic lamella spacings (including intermetallic β -Al₅FeSi platelets) all of which contribute to a reduction in fatigue performance [5,23,24,34]. To compensate for the low heat transfer rates, a metallic chill (usually made of cast iron, steel or copper) may be placed in the molding system directly in contact with the bulkhead to facilitate increased heat transfer and a finer cast microstructure [5,35,36].

2.2. Factors Influencing the Fatigue Performance of Cast Components

Failure occurring under conditions of cyclic loading is called “fatigue failure”, which can have very severe consequences as component failure is often catastrophic and occurs suddenly without warning. Fatigue can be defined as:

“The process of progressive localized permanent structural change occurring in a material subjected to conditions that produce fluctuating stresses and strains at some point or points and that may culminate in cracks or complete fracture after a sufficient number of fluctuations”[37].

Fatigue is considered to be the most common mechanism by which engineering components fail, and it accounts for at least 90% of all service failures attributed to mechanical causes [2,15,36,37].

The fatigue process consists mainly of four important stages:

- 1) Nucleation or micro-crack initiation
- 2) Structurally dependent crack propagation (often called the "short crack" or "small crack" phase)
- 3) Macro-crack propagation or stable crack growth that can be characterized by linear elastic fracture mechanics, elastic-plastic fracture mechanics, or fully plastic fracture mechanics
- 4) Unstable or fast crack growth resulting in catastrophic fracture.

The fatigue fracture surface generally consists of three main regions that correspond to fatigue crack initiation, fatigue crack growth and fast fracture. From the point view of fatigue life, the crack propagation dominates the low-cycle fatigue (LCF) life, and crack initiation controls the high-cycle fatigue (HCF) life [12,15,36,37].

Due to their widespread application in structural components, the fatigue and fracture behavior of cast Al–Si alloys have been extensively studied. It has been reported that fatigue resistance of the alloy depends greatly on discontinuities in the microstructure [26,36,38]. Low SDAS, fine grain size, low porosity level (size and number), fine eutectic phase, and low volume fraction of coarse inter-metallics all contribute to an increase in the fatigue life of the alloy [39-42].

According to the previous studies, several other parameters including high elastic limit and tensile strength, and narrow stress/strain hysteresis loop will also improve fatigue resistance of the alloy [1,26,36,39,40,42]. Whereas, in applications involving thermal cycling leading to thermal stresses both a high thermal conductivity and low thermal expansion coefficient can enhance resistance to fatigue failure [2,41].

Aluminum alloy castings are prone to pore formation owing to the large volumetric shrinkage associated with solidification that may be up to 7% [38,43]. Several studies [34,44-48] have shown that porosity is the major cause for rejection of the Aluminum-Silicon castings in structural applications involving cyclic loading. Both large individual pores and clusters of small pores create a high stress concentration region adjacent to this microstructural defects, and act as crack initiation sites that greatly reduce the crack initiation stage. It has been concluded in a number of studies that, at a given stress, the fatigue life is dominated by the propagation of a crack that initiates from a pore, or a cluster of closely spaced pores, after a relatively small number of cycles [9-11,16,21,32,49]

2.3. Porosity

Generally, two types of porosity may occur in cast aluminum, when classified by the size of the pores:

1) Macro-Scale Porosity:

A series of interconnected cavities resulting from the liquid volume contraction accompanying solidification, associated with liquid encapsulation. Macro-shrinkage voids are generally confined to the thermal center of a section, but can extend to the casting surface and are generally greater in size than 1mm in equivalent radius [23,49-52].

2) Micro-Scale Porosity:

Is defined as a series of discrete, separate cavities less than 1 mm in equivalent radius that form as a consequence of hydrogen bubble precipitation during solidification and/or liquid encapsulation at high solid fractions [15,32,50,52].

Starting first with macro-scale porosity, in cases where directional solidification is lost in a casting and significant regions of liquid encapsulation occur (large pockets of liquid become surrounded by solid material), significant voids ('macro-shrinkage') can form as the volumetric shrinkage associated with solidification causes the pressure within these regions to drop below the vapor pressure of aluminum. Good casting design including the strategic placement of ingates, risers, chills and/or insulation can generally avoid most liquid encapsulation and therefore macro-shrinkage formation [43,48].

In contrast, the avoidance of micro-scale porosity is not so straightforward and generally occurs in all aluminum alloy castings in spite of achieving good directional solidification – i.e. no liquid encapsulation. There are two mechanisms for the formation of micro-scale porosity: one related to changing solubility of hydrogen associated with the liquid-to-solid transformation in aluminum; and the other related to the isolation of small inter-dendritic pockets of liquid within the mushy zone at high solid fractions [23,53].

In directionally solidified castings hydrogen-based micro-porosity can form adjacent to or within the two-phase mushy zone if the hydrogen content within the liquid exceeds a threshold. The hydrogen solubility in aluminum is about 0.7 (mL)/100 (cm³) at the liquidus at atmospheric pressure and 0.05 (mL)/100 (cm³) at the solidus [23]. During solidification, hydrogen is rejected from solidifying metal into the liquid, and if the solubility limit in the liquid is exceeded together with an overpressure associated with nucleation, hydrogen bubbles can nucleate and grow [9,15,52]. The solubility limit in the liquid is dependent on the liquid pressure, which can vary from the bulk liquid pressure at low solid fractions, to a lower pressure dependent on the pressure drop occurring within mushy zone at high solid fractions. The pressure drop within the liquid-to-solid phase change interval arises due to the need to feed liquid to compensate the volume decrease associated with solidification through a semi-solid structure in which the permeability decreases with increasing solid fraction. Thus, the inter-dendritic liquid experiences a hydrogen concentration increase and a pressure drop, both of which generally increase with increasing fraction solid [43]. Conditions conducive to hydrogen pore nucleation and growth can occur within the mushy in castings in which the initial concentration of hydrogen in the bulk

liquid is well below the solubility limit. Studies have shown that long freezing range alloys tend to be more prone to micro-pore formation [48,52,54].

In regard to the second mechanism for the formation of micro-scale porosity, the development of the cast microstructure with increasing fraction solid generally allows for mass feeding through interconnected liquid channels until high solid fractions at which point mass feeding ends and small inter-dendritic pockets of liquid become isolated. Shrinkage-based micro-porosity will form in association with the small isolated pockets of inter-dendritic liquid as the pressure within them will drop below the vapor pressure of aluminum as the liquid solidifies [12,24,43]. This microstructural defect can be found in most castings, where the diameters of the pores range from a few microns to 1 (mm) when viewed on a polished plane [32,43]. The size distribution of both inter dendritic, hydrogen-based, micro-porosity and shrinkage-based, micro-porosity, scales with the microstructure – e.g. dendrite cell size and primary and SDAS [7,8,22,35,45,55]. Obviously, hydrogen-based micro-porosity that forms within the bulk liquid ahead of the solidification front and either floats or is pushed by the solidification front will be large and independent of the microstructural length scale.

2.4. The Solidification Sequence of A319 Including Nucleation and Growth Processes in Solidification

Moving on to solidification and the development of the as-cast structure, alloy A319 is a heat treatable, hypoeutectic Al-Si alloy with two main solidification stages:

- i. Formation of primary aluminum dendrites
- ii. Development of two-phase Al-Si eutectic and intermetallic phases [6].

The amounts of silicon and copper vary within the A319 alloy. Generally, copper contributes to strength, and silicon improves castability. The nominal range of Silicon in composition is reported to be from 5.5 to 9%, and copper from 2 to 4.5% [23,50,56-58]. The type of casting procedure and component application dictates the silicon and copper contents. For those applications requiring a lower dispersed porosity in sand cast applications the optimum alloy would be the one with a higher Si concentration and a lower Cu concentration [57,59]. The specific chemistry provided by Nemak shows that the silicon range in the alloy used for this research is 8.10-8.75%.

The binary aluminum-silicon phase diagram shown in Figure 2.2 displays a simple system with a eutectic at 12.6 wt% Si and 577°C [23].

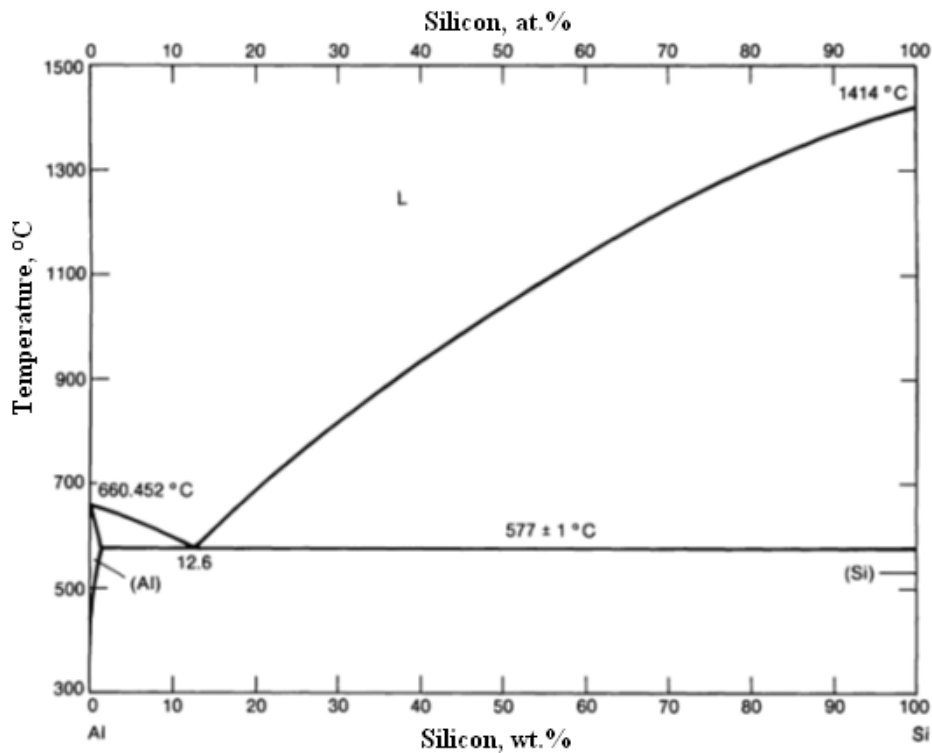


Figure 2.2: Aluminum-Silicon phase diagram [3]

In the more complex multi-component A319 alloy systems, a variety of inter-metallics form prior to, during and after the formation of the main Al-Si eutectic [4,60]. The sequence of solidification and the formation of secondary phases in Al-Si-Cu foundry alloys can be described as follows:

- 1) Solidification begins with the formation of primary α -Aluminum dendrites at approximately 615°C. As the primary α -Aluminum dendritic network develops (increasing solid fraction) there is an associated increase in the concentration of silicon and copper in the inter-dendritic liquid. Variability in the SDAS and curvature effects lead to a gradual coarsening of SDAS during primary phase growth.
- 2) At about 560°C the main Aluminum-Silicon eutectic begins to form, leading to a further increase in Copper content in the remaining liquid.
- 3) This is followed by the formation of Mg_2Si and $Al_8Mg_3FeSi_6$, which happens at approximately 540°C.
- 4) Inter-dendritic, blocky $CuAl_2$ with $\beta-Al_5FeSi$ platelets form at around 525°C, and finally;
- 5) Eutectic $CuAl_2$ forms at about 507°C with scattered α -Al and $Al_5Mg_8Cu_2Si_6$ if Mg is present [6,10,11,32,33,51,59,61].

The morphology and distribution of the eutectic Al-Si phase can influence fatigue performance and can be modified by the addition of Sr [2]. In the modified microstructure, large Si needles change to fine fibers. In addition, the other inter-metallics adopt various morphologies, and can significantly affect alloy mechanical properties. For example, in the presence of iron, the faceted plate-like $\beta-Al_5FeSi$ phase will form which severely reduces the mechanical properties (e.g.,

fatigue life and ductility). The plate-like morphology of β -intermetallics can be altered into a less harmful form such as script-like α -Al₈Fe₂Si or α -Al₁₅(Fe,Mn)₃Si₂ through the addition of modifiers (e.g., Mn, Sr, Cr, Al-Ti and TiB₂) [2,4,60,62].

Phase transformations in alloys are controlled by a combination of nucleation and growth processes. Solidification begins with nucleation of the primary phase, which is the process of creation of a cluster of atoms of crystalline structures of a critical size from the melt wherein the subsequent addition of atoms to the crystal results in a net reduction in the system energy. There are two types of nucleation:

- i. Homogeneous nucleation: where the clusters of atoms in a melt form free of any impurities.
- ii. Heterogeneous nucleation: where solidification is started on a foreign surface that can be one or a combination of the mold surface, oxide skin, or particles suspended in the melt. The foreign particles can be unintentional impurities or deliberate additions for the purpose of enhancing desired microstructure [63-65]

In both cases the rate of nucleation is strongly dependent on the temperature or the amount of undercooling ΔT , where ΔT is defined as the difference in temperature between the equilibrium liquidus temperature and the melt temperature. Thévoz *et. al.* have developed an empirical nucleation model, summarized in Figure 2.3, based on a distribution of nucleation sites which become activated at different under-coolings [66].

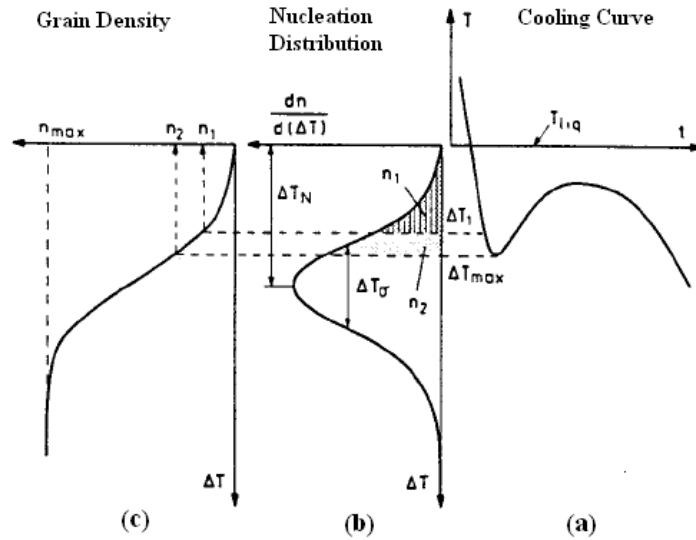


Figure 2.3: Nucleation model used in the microscopic calculation of equi-axed solidification. At a given undercooling (a), ΔT_1 , the density of nuclei, n_1 , within the liquid is given by the integral (c) of the distribution (b) [66].

As can be seen in Figure 2.3.a, the grain density at a certain undercooling, ΔT_1 , can be calculated by the integral of the nucleation site distribution from zero undercooling to ΔT_1 (Figure 2.3.b).

Once a stable crystal has formed, the crystal begins to grow by the addition of atoms to the crystal. Growth is generally limited by a combination of mass and heat transport, with the latter dominating in most industrial alloys systems. The classical picture of the grain structure of a casting is shown schematically in Figure 2.4. The outer zone is called the chill zone, which contains randomly oriented dendrites, the middle section is the columnar zone, which contains dendrites oriented with the direction of heat flow and the central part is the equi-axed zone, which again contains randomly oriented dendrites. Figure 2.4 illustrates the transition from various morphologies that can arise due to the interplay between the evolving thermal field

within the casting and nucleation and growth processes. In grain refined aluminum alloys, the dominant grain morphology is dendritic equi-axed, over a broad range of cooling conditions [33,67].

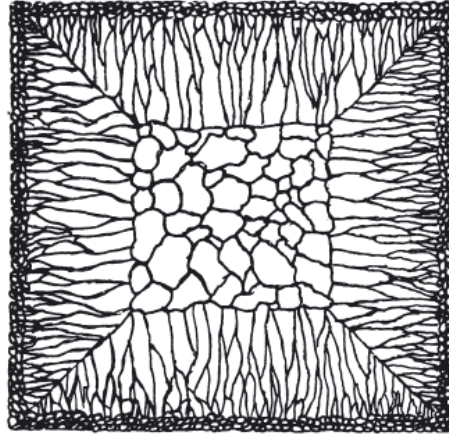


Figure 2.4: sketch of ingot structure showing chill zone, columnar zone, equi-axed zone [31]

The diagram shown in Figure 2.5 summarizes the influence of the temperature gradient, G , and growth rate, V , on the as-cast microstructure for a given hypothetical alloy. Note that under unidirectional heat flow conditions, the product of G and V yields the cooling rate, appearing as lines sloping downward from left-to-right on the diagram. According to the diagram, at low growth velocities and high thermal gradients plane-front growth occurs; at low growth velocities and intermediate thermal gradients cellular growth occurs; and at low growth velocities and low thermal gradients dendritic growth occurs. High velocities tend to favor equiaxed structures, except at high gradients, and generally for a given morphology there is a reduction in the length scale – i.e. secondary and primary dendrite arm spacings become smaller – with increasing cooling rate [67].

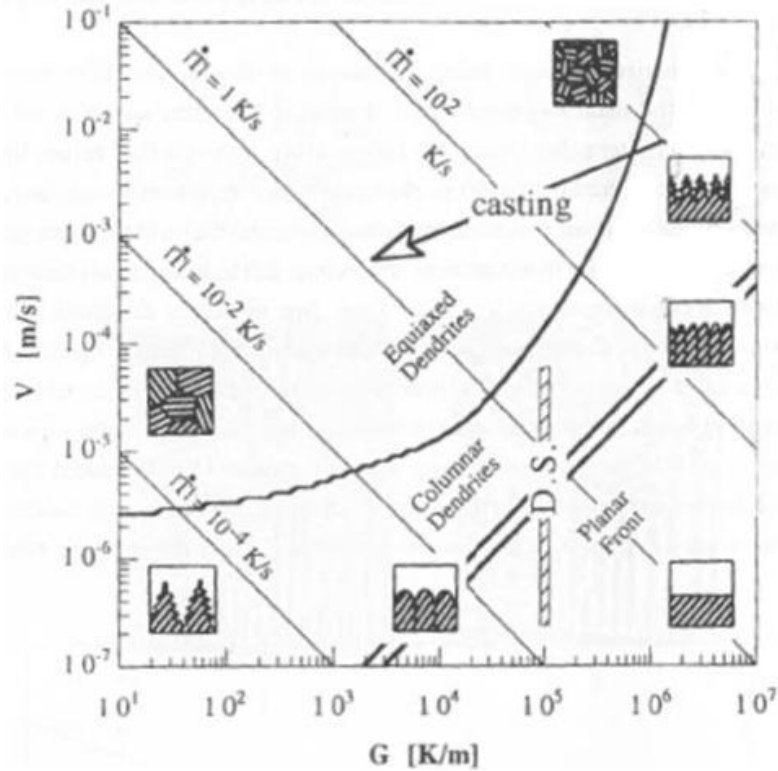


Figure 2.5: Schematic summary of single-phase solidification morphology [67]

Control of the cast structure is a key requirement in the foundry industry. One aspect, the grain size, is an important quality characteristic from the standpoint of mechanical performance of the casting. As previously alluded to, a fine-grained structure in a casting, results in good fatigue performance by the fact that virtually all of the microstructural discontinuities scale with the grain size. Moreover, it is desirable to have small grains with globular dendrite morphology in order to facilitate late-stage liquid feeding to reduce the occurrence of unfavorable micro-porosity, as previously discussed [41,57,63,68].

The grain size is dependent on the availability of nucleation sites, and on the cooling rate at which the melt is solidified. In the context of the former, the addition of heterogeneous nucleation sites via a grain refiner is one effective treatment that reduces grain size and improves

the quality of the castings. Grain refining additions commonly used in the aluminum industry include Al-Ti and Al-Ti-B master alloys [41,58,63,68]. On the other hand, for a given alloy chemistry, increasing the cooling rate results in larger undercooling leading to the activation of a greater number of heterogeneous nucleation sites within a given population that is illustrated schematically in Figure 2.5. Moreover, to facilitate increased mass transport the primary Dendrite Arms Spacing (DAS) and Secondary Dendrite Arm Spacing (SDAS) decrease. Relationships of the following form have been found to provide reasonable fit:

$$SDAS = at_f^n = b(CR)^{-n} \quad (2.1)$$

where the exponent “ n ” is in the range of $\frac{1}{3}$ to $\frac{1}{2}$ for the SDAS and generally very close to $\frac{1}{2}$ for DAS. In Equation 2.1, t_f is the solidification time, a and b are fitting parameters, CR is the cooling rate ($^{\circ}\text{C/s}$) [2,31,33,55,69].

The dendrite arm spacing (DAS) may be measured to quantify the “Microstructural fineness”. Silicon particles are usually characterized by an aspect ratio. Steps taken to achieve fine dendrite size also alter the eutectic silicon, in that the particle size and aspect ratio are reduced [36,61].

Both types of microstructural discontinuities discussed previously scale with cooling rate. For the case of hydrogen-based porosity, higher cooling rates lead to smaller dendrite arm spacings and finer microstructure, reducing the effective diffusion interface area [21,24,48]. Moreover, high cooling rates result in high temperature gradients, which lead to easier liquid feeding. Hence, there will be a reduction in shrinkage porosity when increasing the cooling rate [53,70].

Unfortunately, those process conditions that are conducive to the development of fine grain size and dendrite morphology - namely cold, high conductivity mold materials and low pour superheat - can lead to the occurrence of “cold shuts”.

Cold shuts occur when solidification progresses too fast or there is excessive loss of superheat during mold filling. This leads to blockage of small sections and to insufficient fluidity to allow mixing in regions where two free surfaces meet leading to a seam or entrained oxide film in the casting [3,71]. A cold shut may appear as a crack or seam with smooth, rounded edge [72]. The causes of cold shuts are:

- i. Poor flow patterns due to inappropriate gating
- ii. Excessively thin walls in the part design
- iii. Process variables such as: low mold temperature, low melt superheat, and long mold filling times [3].

Cold shuts are serious sources of stress concentration and often act as crack nuclei for fatigue fractures. This discontinuity can reduce the strength of a part to an extent that it undergoes fracture under a single application of load [71,72].

2.5. Chill technology

The complicated geometries of many cast products such as cylinder heads and engine blocks (cast via the precision sand casting process) consist of thick and thin sections at varying distance from in-gates. Consequently, the material experiences a range of cooling rates resulting in a range of microstructural discontinuities size and fatigue performance. One approach to achieve

high fatigue resistance in thicker casting sections, such as the bulkhead in engine blocks, is to allow the casting component to make contact with a metallic chill [3,5-7,32,35,51,73-75]. Because of the comparatively large thermal mass and high conductivity compared with sand, the chill acts to increase heat transfer from the solidifying metal thereby increasing the cooling rate.

In 2009, MacKay *et. al* [5,17,24] reported on the use of “*a combination of controlled filling (Cosworth casting process) and increased solidification rate caused by a cast iron and copper chill*” in order to enhance the ultimate tensile strength, elongation and high cycle fatigue performance of a cast component by virtue of a reduction in the length scale of the microstructure of the cast product. Several research groups [7,51] have studied the effect of copper chill on the size, morphology and distribution of microstructural features (such as SDAS, porosity, inter-metallics, eutectic phase, etc.) in cast aluminum-silicon alloys, and hence on fatigue properties. Generally, all these studies mention the fact that:

“The microstructure of the solidified casting becomes progressively coarser with increased distance from the chill.” [7]. Some other investigations [4,8,12,35,76,77] have reported the same results when employing cast iron and steel chills.

In 1991, Kumar *et. al* [78] developed a model to evaluate the transient heat flux across the casting-chill interface as a function of thermo-physical properties of the chill material and its thickness for two aluminum alloys, one with a eutectic composition and the other with a long freezing range (Al-3%Cu-4.5%Si). For this purpose, copper, cast iron and steel chills, each in four different thicknesses and exposed to ambient conditions at one end, were used in the experiments. The thermal histories at different locations in the chill obtained during the

experiments were used to validate the model. Gafur *et. al* [79] conducted a similar experiment for solidification of square bars made of commercially pure aluminum with different super heats, exposed to cast iron chills with different thicknesses. They reported that both chill thickness and melt superheat have a significant effect on the rate of temperature elevation in the chill. In addition, another set of experiments with two different size iron chills were completed by M. Dash and M. Makhoulf [12] in order to investigate the effect on solidification rate, size, and volume fraction of microstructural constituents.

In 2012, Schneider *et. al.* designed a casting experiment with a simplified cylinder head geometry using a copper chill to investigate the effect of chilling on the microstructure of the casting. They reported shorter solidification times and hence, smaller SDAS in the chilled regions [80]. All of these studies clearly point to the efficacy of chill technology in enhancing heat transport and reducing the length scale of the microstructure. They also point to the effect of chill size (thermal mass) on capacity to enhance heat transport. There have been limited studies on the role of gap formation in the capacity of chills to remove heat.

Several studies have made an attempt to understand the heat transfer mechanism at the metal-mold interface which can be characterized by:

- 1) An interfacial heat flux (q)
- 2) Interfacial heat transfer coefficient (h) [61,79].

The interfacial thermal contact resistance, which affects the rate at which heat is extracted from the melt to the chill and mold and the casting microstructure, is strongly influenced by:

- 1) The thermo-physical properties of the casting and the mold material
- 2) Roughness of the mold and the chill surfaces
- 3) The geometry of the metal-mold (chill) interface
- 4) The orientation of the casting–mold interface with respect to gravity (contact pressure)
- 5) Initial temperature of the mold and the chill
- 6) Metal pouring temperature
- 7) Mold coatings [61,73,81-86].

2.6. Casting/Mold Interfacial Heat Transfer

In addition to mold temperature, mold thermal conductivity and metal superheat, the development of the contact resistance at the casting/mold interface plays a critical role in heat transport particularly with regards to chill technology. Generally, during metal casting processes, the contact between the mold and the metal varies with time owing to the interplay between thermal contraction of the casting and thermal expansion of the mold. Consequently, the resistance to heat flow that develops at the interface (expressed mathematically as $1/h$ where h is the heat transfer coefficient) remarkably affects the solidification rate of metal, especially in die castings and sand castings that involve chills [87,88].

When the melt first contacts the mold surface (or chill), the heat transfer coefficient is generally high because of the good contact (wetting) of the mold by the melt. Rapid cooling of the metal at the interface causes a large undercooling and large number of nuclei to form and grow leading to a chill zone in the casting microstructure [87,89]. The development of the cast structure generally leads to a gradual reduction in heat transport due to the formation of small asperities on the cast

surface leading to a loss in contact. As solidification continues, a point is reached where mass feeding ends and the casting begins to thermally contract. The development of a gap leading to the rapid loss of heat transport (increase in resistance) then depends on several factors including:

- i. The relative thermal expansion coefficients of the casting metal and mold material (the mold material expands due to an increase in temperature)
- ii. The presence of mechanical constraints related to geometry (for example the casting may surround the mold and therefore contract onto the mold limiting gap formation); and
- iii. The presence of sand molding binders, coatings or lubricants that evolve gas resulting in the formation of a gap at the interface;

The formation of a gap results in a decrease in heat transport, which is generally believed to be proportional to the size of the gap owing a shift to conductive heat transport within the fluid in the gap in combination with radiation. Heat transfer in this step is mainly governed by conduction across the “air-gas” mixture. The contribution of radiation heat transfer is usually believed to be negligible to the overall heat transfer coefficient in the case of low melting point alloys such as aluminum alloys [61,81-84,87,88,90].

The development of the interface gap and the associated resistance to heat transport is complex and hence, it is necessary to develop a mathematical model to enable calculation of the evolution of the thermal contact resistance at the metal-mold interface based on thermocouple data [88].

2.7. Quantification of Casting/Mold Interfacial Heat Transfer Coefficient

To date no specific correlation is available for the estimation of interface heat transfer coefficient between casting and chill surfaces from fundamental principles. From a general review on this subject, three methods have been suggested to estimate the interfacial heat transfer coefficient:

- 1) To measure the size of the gap formed between the casting and the chill and convert this gap size to an appropriate heat transfer coefficient.
- 2) To conduct temperature measurements in the casting and the chill at several chosen locations, and use a mathematical model of heat conduction to derive the interfacial heat transfer coefficient based on trial-and-error variation of the heat transfer coefficient.
- 3) To conduct temperature measurements in the casting and the chill at several chosen locations, and use the inverse method to derive the interfacial heat transfer coefficient.

After the use of the first method in 1920, researchers [77,81,82,84,85,87,91-93] noticed that both the casting and the chill move during casting.

The resistance to heat flow at the casting-chill interface is usually defined as a time dependent function, due to the time dependency of the plasticity of the solidifying metal and the oxide growth on the metal surface [85].

Wang and Matthys [86] have reported that a widely used method for the estimation of thermal contact resistance is to release a droplet of molten metal onto a solid surface, measure the temperature of the droplet, and fit the data to a numerical or analytical heat transfer model to calculate thermal contact resistance [84].

Ho *et. al.* [94] suggested that it is possible to calculate the interfacial heat transfer coefficient by determining the gap thickness. They simulated the solidification of various castings in different molds and noted the difficulties caused by lack of material property data. It should be noted that it is possible to get useful numerical solutions for the temperature distribution in solidifying castings only if the interface heat transfer coefficients are known with sufficient accuracy [87].

Isaac *et. al.* [95] studied the formation and distribution of air gaps formed during the solidification of castings in metallic molds. They determined that the value of interfacial heat transfer coefficient is time dependent, and decreases as the solidification within the mold progresses. Their research results show that thermal contact resistance increases when the surface curvature and the rate of solidification increase [87].

Chiesa [96] obtained interfacial heat transfer coefficients for various die mold coating conditions. His results demonstrated that thermal contact resistance exists even during the mold filling when the metal is still in the liquid state.

Kulkarni [82] studied the thermal behavior of hollow cylindrical castings for aluminum base alloys using the FEM technique. Kumar [78] reported that the heat flux is an exponential function of time.

Kang *et. al.* [97] obtained the heat-transfer coefficient between a heating plate and a roller during the direct rolling process for steel by the trial-and-error method. For this purpose, they used FEM to solve a two-dimensional transient heat-conduction problem.

Pokorny *et. al.* [98] also used the trial and error method to determine the metal-mold interfacial heat transfer coefficient in an AZ91D magnesium alloy casting, to develop a visco-plastic deformation model which predicts hot tear evolution in the alloy.

Griffiths [81,90] developed a model to predict the interfacial heat transfer coefficient for a water-cooled copper chill casting during unidirectional solidification - vertically upward, vertically downward, and horizontal - of a cylindrical Al-7% Si alloy. In his research, the heat transfer coefficient was derived from the chill and melt thermocouple data by an explicit finite difference method to the inverse heat conduction solution. It was concluded that the vertically upward casting procedure was associated with the highest heat transfer coefficients.

For the vertically up-ward case, the chill and casting surface roughness parameters were measured by an RS Surtronic 200 surface profileometer, and added as:

$$R_z = \sqrt{R_{z(chill)}^2 + R_{z(casting)}^2} \quad (2.2)$$

to determine the mean separation formed between the casting and the chill surfaces. The casting surface adjacent to the chill was also examined. The results showed that while the chill surface was planar, the casting surfaces were convex. The main height of convexity was reported to be 12 μm . The overall heat-transfer coefficient was then calculated from the sum of heat transfer coefficients for the contact areas and for the parts that were separated because of the gap formation.

Figure 2.6 compares the experimentally determined and modeled heat transfer coefficients, and Figure 2.7 shows the agreement between the calculated and measured temperatures in the chill and the casting. The author has reported that:

“A precise agreement cannot be expected because of the wide scatter in the experimentally determined heat-transfer coefficients and because of the many assumptions and estimations involved in the model. Nonetheless, because an important feature of the model was the inclusion of the deformation of the initial solidified skin of the casting, the agreement obtained supports the suggestion that this was a significant factor in the transfer of heat between the casting and the chill.”

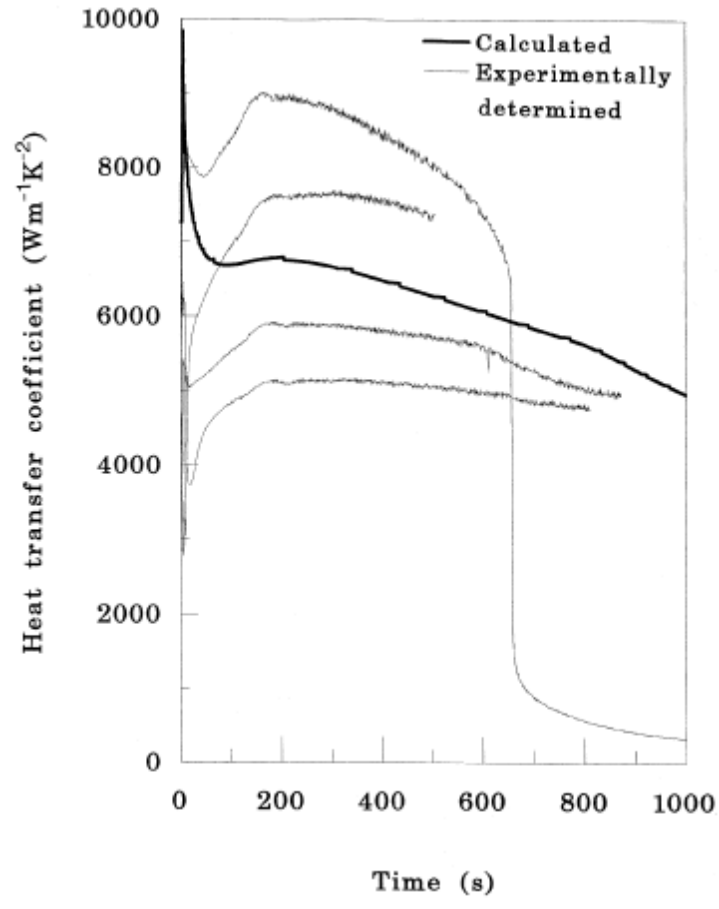


Figure 2.6: Graph showing a comparison between the modeled heat-transfer coefficient and experimentally determined values for the unidirectional solidification vertically upward of an Al-7%Si alloy casting [81]

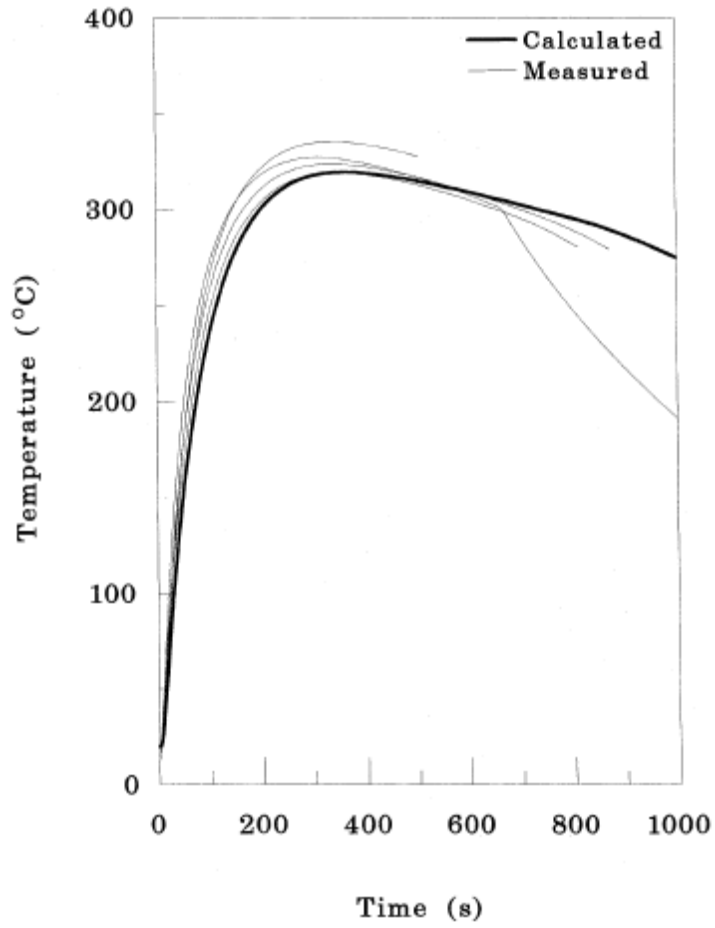


Figure 2.7: comparison of measured and calculated temperatures within the copper chill at a point 75 mm from the casting-chill interface [81]

3. Scope and Objective

The objective of this research is to calculate quantitatively the efficacy of a “Water-Cooled Chill” in terms of its ability to facilitate a transition in cooling from an initial slow cooling rate to fast cooling while material within proximity to the chill is undergoing solidification. A wedge-shaped casting made using the same precision sand casting process used to manufacture blocks and cylinder heads for gasoline-based drive trains will be used for this assessment. The wedge molds have been provided by “Nemak Canada”. The geometry of the casting and molding system is based on a standard format used by Nemak to assess microstructure and property variation with cooling rate. The ultimate goal of this work will be to support the development of delayed water-cooled chill technology to improve the fatigue performance of A319 in small, four-cylinder, turbocharged engine block applications. To achieve this goal, a combination of experimental and analytical methods will be used.

In the experimental part of this research, bonded sand wedge molds instrumented with thermocouples and configured with two different chills, one with and the other without water cooling (both also instrumented with thermocouples) will be used to acquire temperature data within the casting at varying distances from the chill and within the chill. Experiments will be conducted under a range of chill preheat temperatures and with varying delay times for water-cooling. Samples will be taken from the casting for metallography and for characterization of the SDAS. Details related to the experimental methodology will be presented in Chapter 4.

The analytical component of the work will focus on an assessment of the interface heat transfer (interface between the casting and the chill) using a conventional heat transfer model developed with the commercial software package “ANSYS CFX”. In this part of the work, the numerical model has been used to evaluate the variation in the heat transfer coefficient with temperature using a trial-and-error approach (a trial temperature and/or time dependent function for the heat transfer coefficient is input to the model and the results from the model compared with measured temperature responses. This process is continued until the model predictions agree with the thermocouple measurements to within an error tolerance). Details related to the numerical model development and application to the wedge sand casting will be presented in Chapter 5.

Finally, as previously described in the introduction section, the water-cooled chill performance metrics to be quantified include cooling rate variations as a function of time and distance from the chill, the associated microstructure length scale (SDAS) variation and, the variation in the heat transfer coefficient. These parameters will be evaluated for the solid chill and the water-cooled chill, with and without delay.

4. Experimental Procedure

4.1. Experimental Methodology

To simulate the broad range of solidification rates experienced in cast cylinder heads and engine blocks, a standard, wedge-shaped casting, shown in Figure 4.1, has been designed by “Nemak Canada” Ltd. The casting is used to assess the variation in microstructure (SDAS) and mechanical properties as a function of distance from the thin end (decreasing cooling rate).

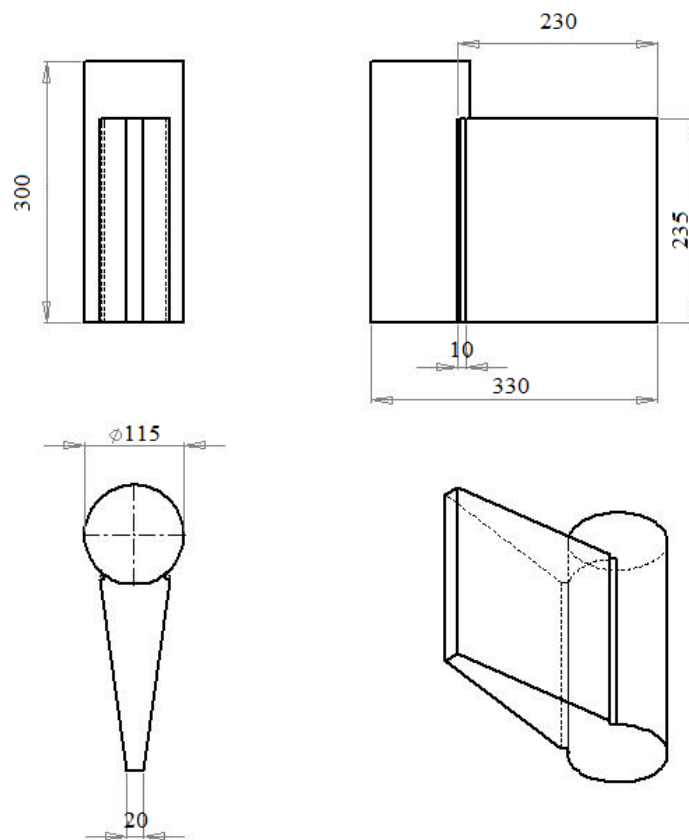


Figure 4.1: Dimensioned drawing of wedge and riser (all dimensions are in mm)

A photograph of $\frac{1}{4}$ of the casting showing the wedge pattern, riser, in-gate and down-sprue is shown in Figures 4.6 and 4.7. The mold was made from bonded silica sand and was fabricated by Nematik using their standard precision sand molding system. A total of ten molds were provided by Nematik to support the research program.

As can be seen from Figures 4.6 and 4.7, the mold is designed to allow solidification horizontally from the narrow end of the wedge toward the large end, which is attached to a large oversized riser. Note also that there is a void space at the narrow end of the wedge to facilitate placement of a chill to accelerate heat transport. In order to design the chills to be utilized in this program, and ensure that they would provide the desired heat extraction capabilities, a model of the casting process including the chills was developed with ANSYS CFX. In particular, the size of the cooling channel to be employed in the water-cooled chill, and its position with respect to the interface were determined with the aid of modeling results. It was also concluded that in order to achieve a high heat extraction capacity, the chill material should have high thermal diffusivity. Hence, the chill was made out of copper as opposed to steel or cast iron that are commonly used in chill technology.

Figure 4.2 (a) and (b) show the two chills – solid and water-cooled, respectively – that resulted from the computational analysis. Figure 4.3 shows a picture of the chills as fabricated. Three holes were drilled into the chills to facilitate placement of thermocouples (Type-K) to within 2 mm of the interface with the casting to measure the variation of the temperature with time during casting.

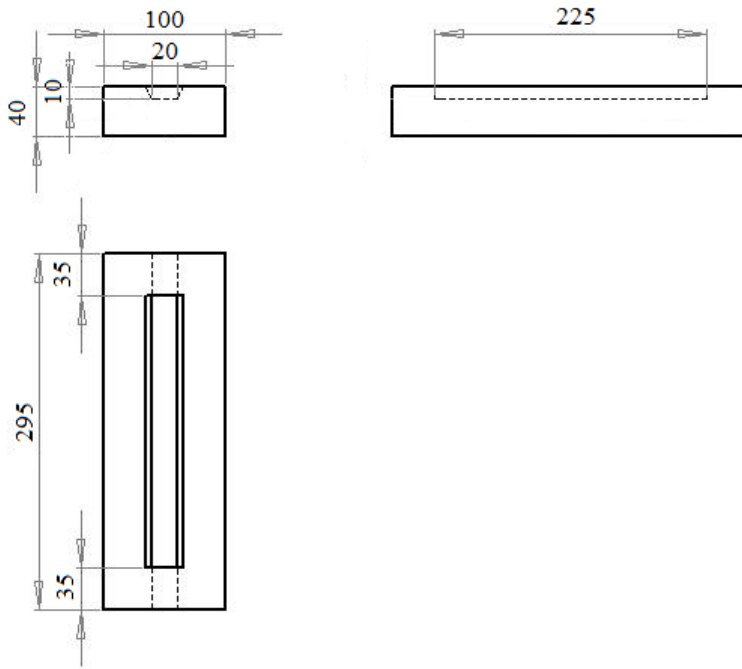
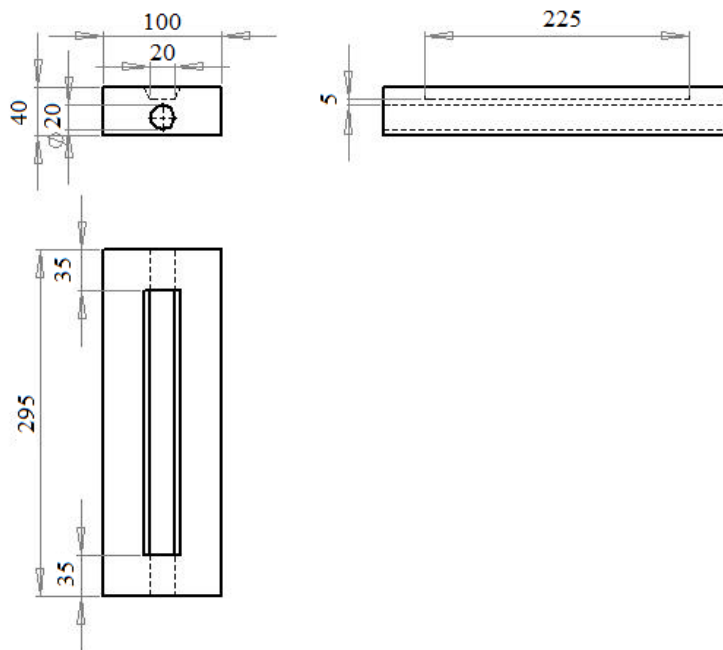


Figure 4.2.a: Dimensioned drawing of solid chill (all dimensions are in mm)



4.2.b: Dimensioned drawing of “water-cooled” chill (all dimensions are in mm)



Figure 4.3: The water-cooled and solid chills

Prior to each casting, eight type-K thermocouples were installed in the mold cavity. A pattern was fabricated with a steel plate to ensure consistency in placement of the thermocouple within the mold cavity. Four of the eight mold thermocouples were placed at the mid height of the mold cavity to measure temperature at different distances from the chill (at 5, 10, 30, and 50 mm). These measurements enabled the investigation of the variation in cooling rate with distance from the chill. The other four thermocouples were placed in the cavity at a distance of 50 mm from the chill but with varying heights. The objective of monitoring the vertical variation of temperature was to assess the effect of fluid flow on the evolution of temperature within the casting (as driven by buoyancy differences associated with temperature gradients in the liquid). The temperature-time data for the eight in-mold thermocouples and 3 in-chill thermocouples (also Type-K) was recorded at a frequency of 2 Hz, with the use of Lab View software.

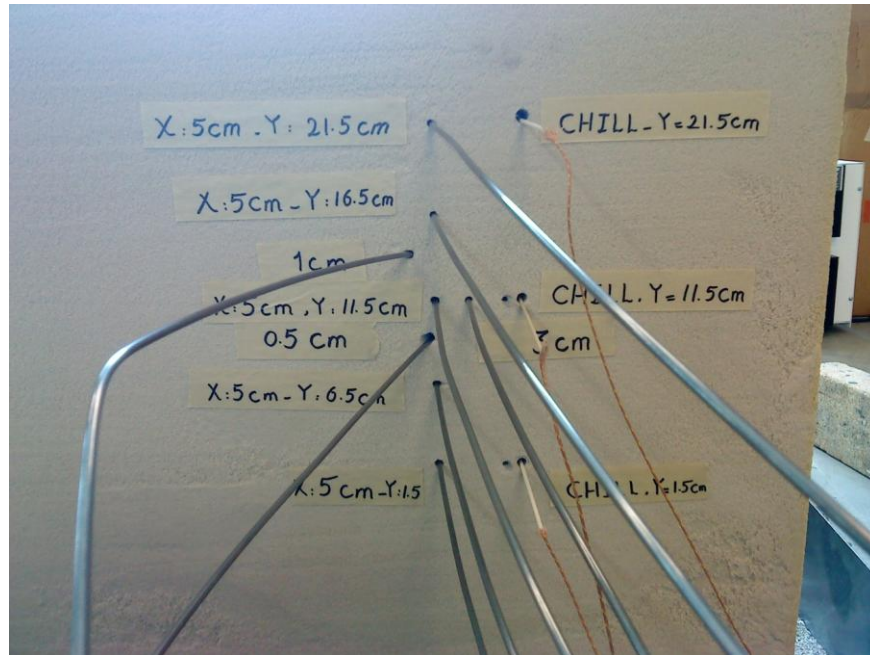


Figure 4.4: The position of the thermocouples used for temperature recording

Prior to casting the two halves of the mold were clamped together. In order to fill each mold, batches of in excess of 18kg of A319 alloy provided by Nemak, with the composition indicated in Table 4.1 were melted in a silicon carbide crucible in an electrical, top-loading, furnace. The furnace was set to a temperature of 800°C. Prior to pouring, argon was injected into the bottom of the melt for 15 minutes through a stainless steel lance with a porous graphite head in order to degas the melt.

Table 4.1: Composition of A319 alloy¹

Alloying Element	Si	Fe	Cu	Mn	Mg	Zn	Ti	Sr
Balance (Wt%)	8.10-8.75	0.27-0.59	2.60-2.95	0.7-Fe-0.44	0.31-0.4	0.4-0.8	0.12-0.16	0.004 max

¹ Chemical Composition provided by “Nemak Canada”

The casting conditions employed for each experiment are shown in Table 4.2. With one exception, Casting 1, the pouring procedure started at a temperature of 740 ± 5 °C. The pour temperature was measured by a Type-K Thermocouple probe inserted into the melt. It took approximately 20 seconds to pour the melt into the mold cavity. In those cases where the chills were preheated, Castings 1-3 and 6, they were put in an electrical furnace to reach the designated temperature, and placed in the mold cavity, just prior to pouring.

The water-cooling system for the water-cooled chills is shown schematically in Figure 4.5. The water flow rate for the experiments was set to 50 (L/min) and measured with an in-line water flow meter. The temperature of the water was fairly constant at approximately 10°C. In the standard water-cooled experiments, the water flow started simultaneously with the metal pouring procedure, and in delayed water-cooling, it started 10 seconds after the completion of pouring process.

Table 4.2: The Conditions of the Castings

	Casting 1	Casting 2	Casting 3	Casting 4	Casting 5	Casting 6
Cooling conditions	Solid Chill	Solid Chill	Solid Chill	Solid Chill	Standard water cool	10 s delayed water cool
Pouring temperature (°C)	780	740	740	740	740	740
Chill temperature (°C)	175	160	115	20	20	115

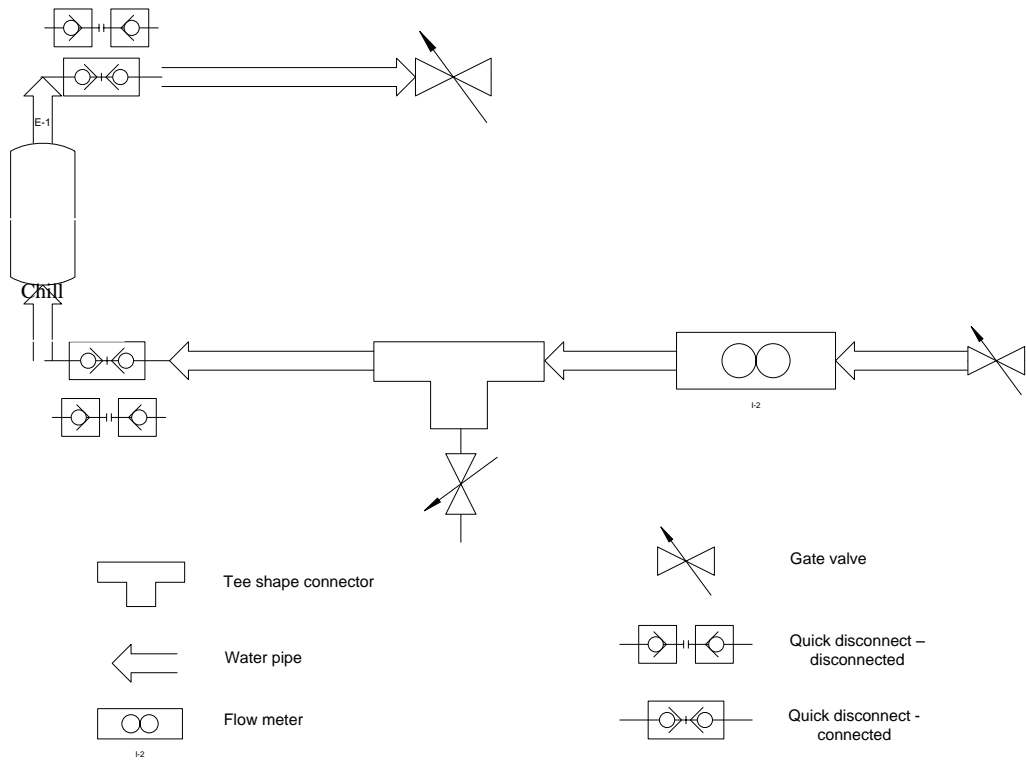


Figure 4.5: Water cooling system



Figure 4.6: Solidified wedge, water cooled chill condition



Figure 4.7: Solidified wedge, solid chill condition

Five metallographic specimens at 5, 10, 30, 50, and 150 mm from the chill were taken from the central vertical plane of Castings 1 and 5. Casting 1 and 5 were chosen as they experienced the lowest and highest cooling rates, respectively, in order to measure and compare the SDAS sizes and derive a mathematical relationship between SDAS size and cooling rate. The metallographic samples were polished down to 0.1 μm with the standardized polishing procedure summarized in Table 4.3, and etched using 0.5% HF solution. Metallographic images were taken with a “Nikon¹ EPIPHOT 300” optical microscope, equipped with a QImaging² digital camera. “UTHSCSA Image tool” software was used to measure the “SDAS”. SDAS analysis at each height for the two casting conditions consists of 40 measurements. The mean value calculated by the software is reported as the SDAS size, and also, the standard deviation of the measurements are reported.

Table 4.3: Metallography procedure

Polishing stage	Substance	Duration
Grinding	Silicon carbide grinding paper: 180, 220, 320, 400, 600, 800, 1200 grit	10 minutes for each stage
Fine polish	6 μm Polish cloth with 6 μm diamond suspension	15 minutes
Final polish	1 μm Polish cloth with 1 μm diamond suspension	15 minutes
Etch	0.5% HF solution	15 seconds

¹ Nikon is the trademark of NIKON Corporation, Tokyo, Japan.

² QImaging is the trademark of Qimaging Corporation, Surrey, BC, Canada.

4.2. Experimental Results and Discussion

4.2.1. Solid Chill Castings

The cooling curves from the thermocouple data obtained from the castings are presented in Figures 4.8 to 4.22 along with the solidus and liquidus lines, which have been added to the plots to aid in identifying when solidification begins and when it is complete.

Figures 4.8 – 4.11 show the thermocouple data for the solid chill experiments. All of the thermocouple results show an initial rapid drop in temperature at all of the thermocouple positions in the casting for the first 200 to 1000 s. The rate of temperature drop then significantly slows until approximately 2500 s at which point there is a moderate increase in the cooling rate. The increase after 2500 s is likely related to the completion of solidification within the wedge and the end of latent heat evolution. Looking at the variation in cooling rate with distance from the chill, there is large variation in the initial cooling rate with the trend showing a decrease in cooling rate with increasing distance from the chill as would be expected, due to the finite thermal diffusivity of A319. The large initial cooling rates directly adjacent to the chill lead to large temperature gradients in the casting and reflect the large heat fluxes that occur when the hot metal first contacts the comparatively cold chill. At longer times the temperature gradients in the casting significantly decrease reflecting a much lower rate of heat transfer to the chill and a shift to the transport of the heat being limited by conduction through the sand mold.

Based on the liquidus and the solidus temperatures included in the graphs, the solidification times at 5 mm distance from the chill range between 46 to 295 s, and at 50 mm distance from the chill between 657 to 1489 s.

Turning to the chill thermocouples, there is an initial rapid increase in temperature, reflecting a high initial rate of heat transfer from the casting to the chill. The temperature in the chill then peaks and slowly decreases in step with the rate of change of temperature in the casting. A comparison of the temperatures recorded at various positions within the chill indicates that there is only a small temperature variation present along the length of the chill, likely related to buoyancy effects that are discussed in more detail in a subsequent section.

There are several additional observations that can be made: firstly, the decrease in the cooling rate in the casting corresponds to the chill approaching its peak temperature in all of the tests. This would appear to indicate that some of the loss in cooling rate could be attributed to a loss in the capacity of the chill to continue to act as a sink for heat. Secondly, there is a relatively large difference between the thermocouple temperature in the casting located 5mm from the chill interface and the thermocouples located in the chill 2mm from the casting interface. This difference likely reflects the development of the gap, which leads to an increase in the thermal resistance across the chill/casting interface. This factor will also limit the ability of the chill to extract heat. The mechanism(s) contributing to the reduction in heat transfer will be investigated further in Chapter 6, Modeling Results and Discussion.

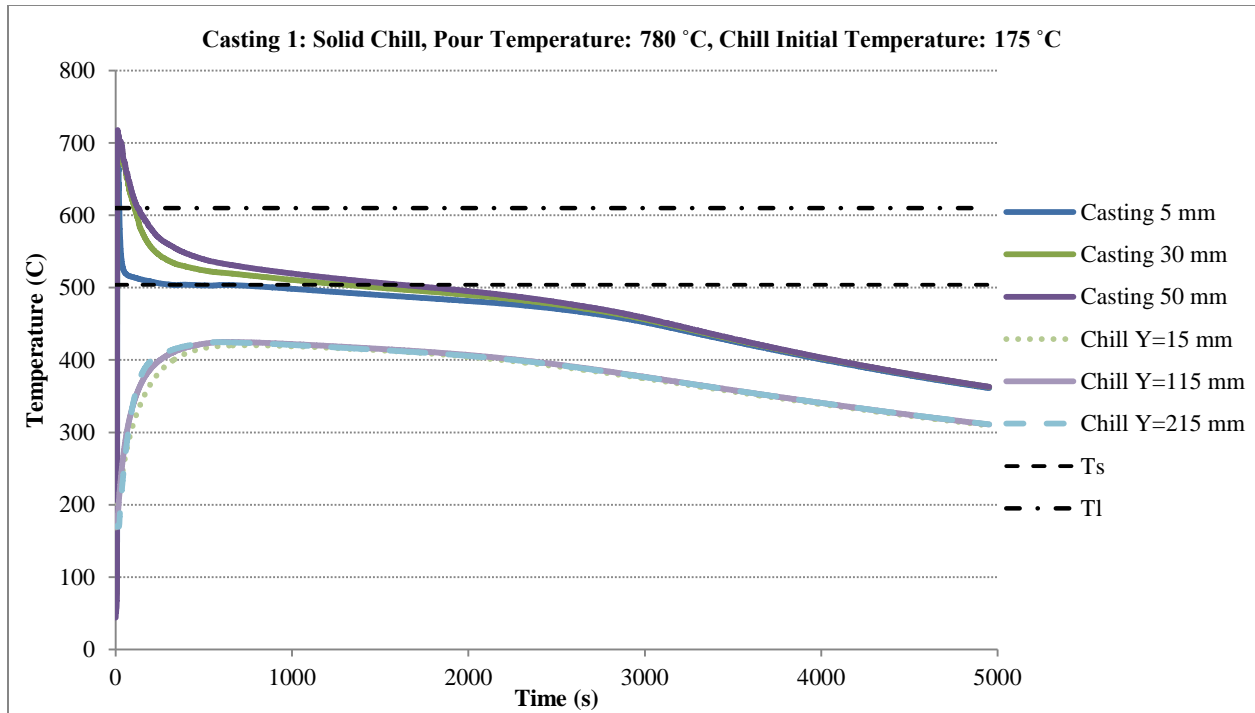


Figure 4.8: Temperature variation with time for various distances from chill and within the chill for Casting 1

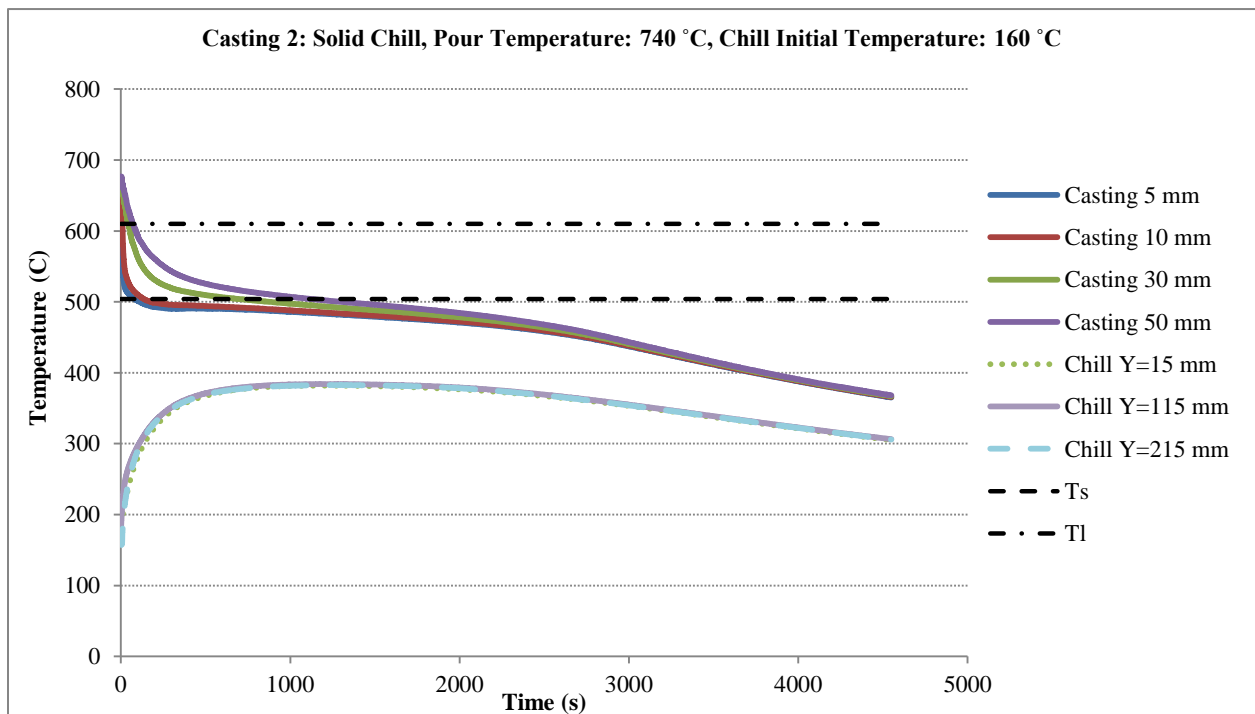


Figure 4.9: Temperature variation with time for various distances from chill and within the chill for Casting 2

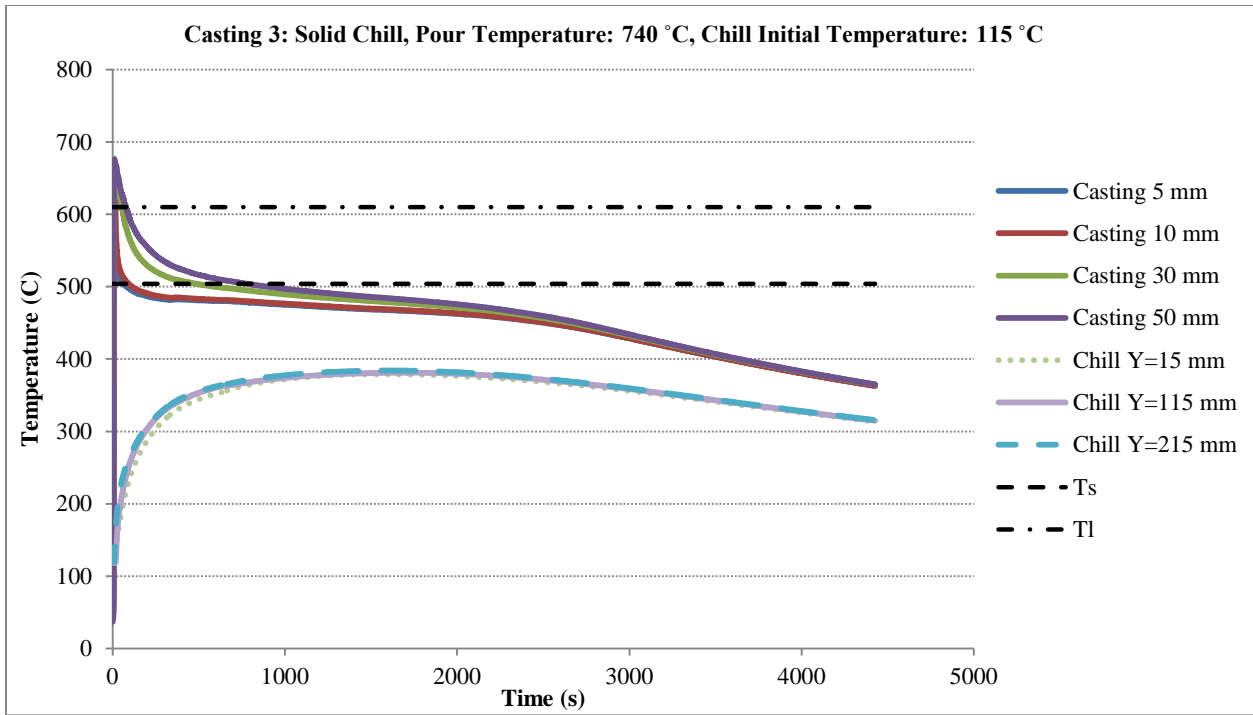


Figure 4.10: Temperature variation with time for various distances from chill and within the chill for Casting 3

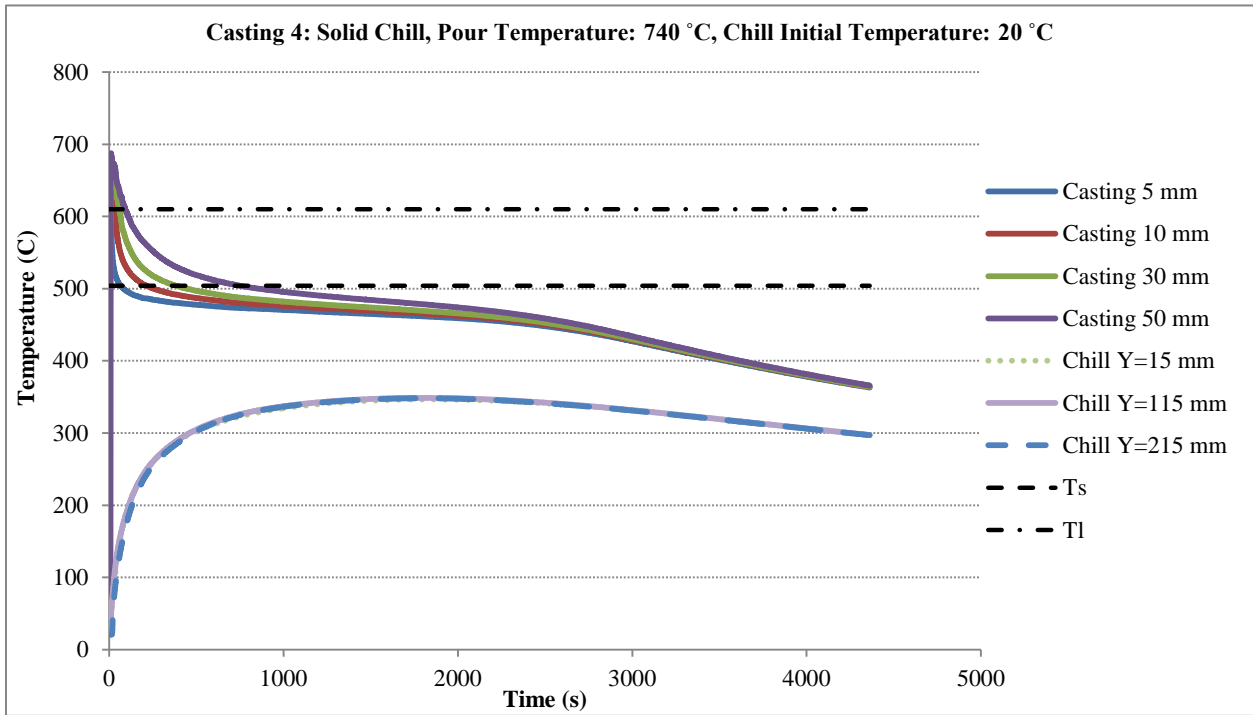


Figure 4.11: Temperature variation with time for various distances from chill and within the chill for Casting 4

Effect of Buoyancy on Temperature in the castings - As previously described, some of the thermocouples were placed in the casting for the purpose of assessing the impact of fluid flow on heat transport. Figures 4.12 – 4.15 show the variation in temperature with time, at 50mm from the chill, and at heights of 15, 65, 115, 165 and 215 mm from the bottom of the casting for castings 1 through 4, respectively.

The graphs show that the melt at the bottom is slightly colder than the melt at the top as indicated by the higher cooling rate observed at the 15 mm height in the case of castings 1-3, and the 15 and 65 mm heights in the case of casting 4. This is because the colder, denser liquid adjacent to the chill sinks to the lower part of the mold and pushes the hotter, less dense melt up away from the chill, developing a re-circulating flow pattern.

Since the buoyancy effect did not cause a significant variation in the cooling curves for the thermocouples located at mid-height, fluid flow was not included in the mathematical models for the sake of computational efficiency. This is discussed in greater detail in Chapter 5.

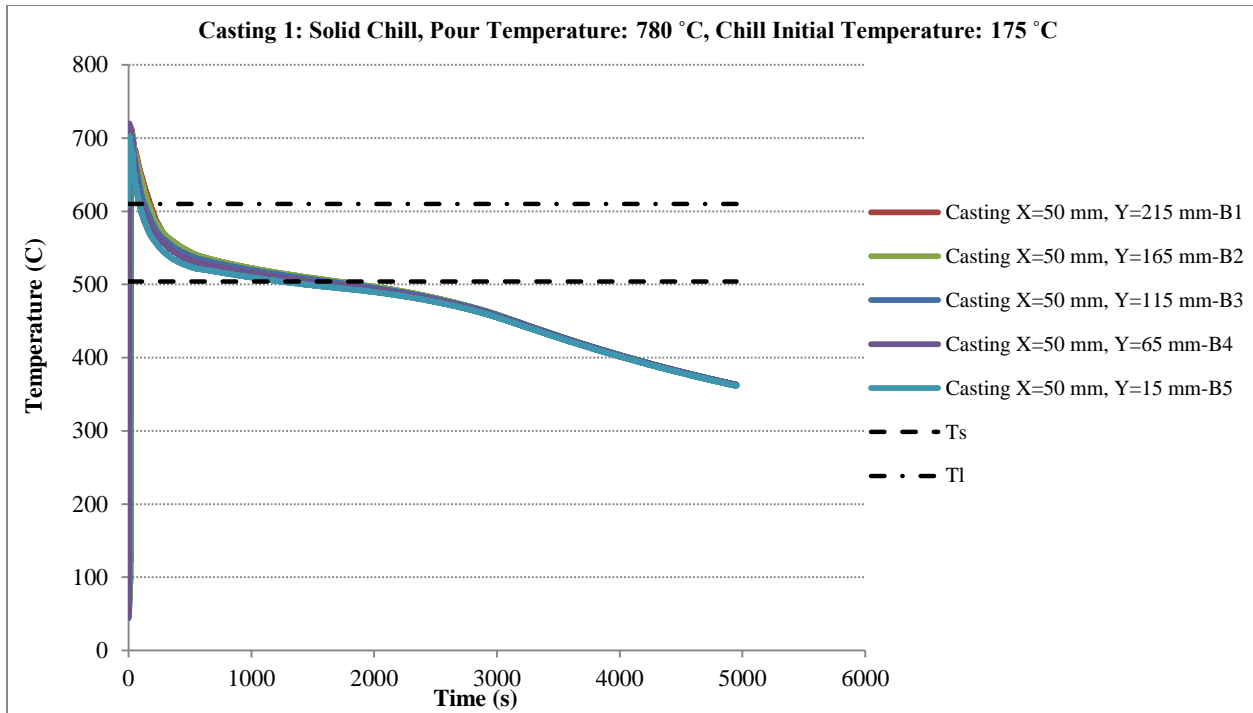


Figure 4.12: Temperature variation with time at various heights, monitoring the buoyancy effect for Casting 1

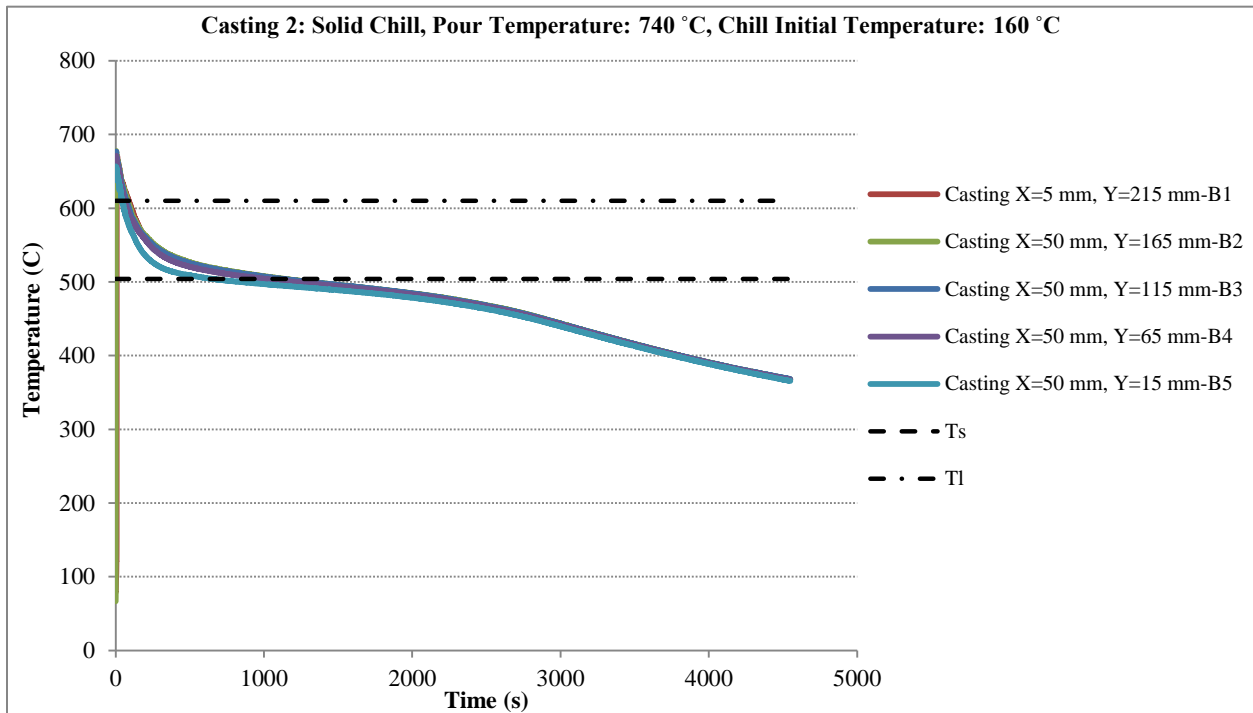


Figure 4.13: Temperature variation with time at various heights, monitoring the buoyancy effect for Casting 2

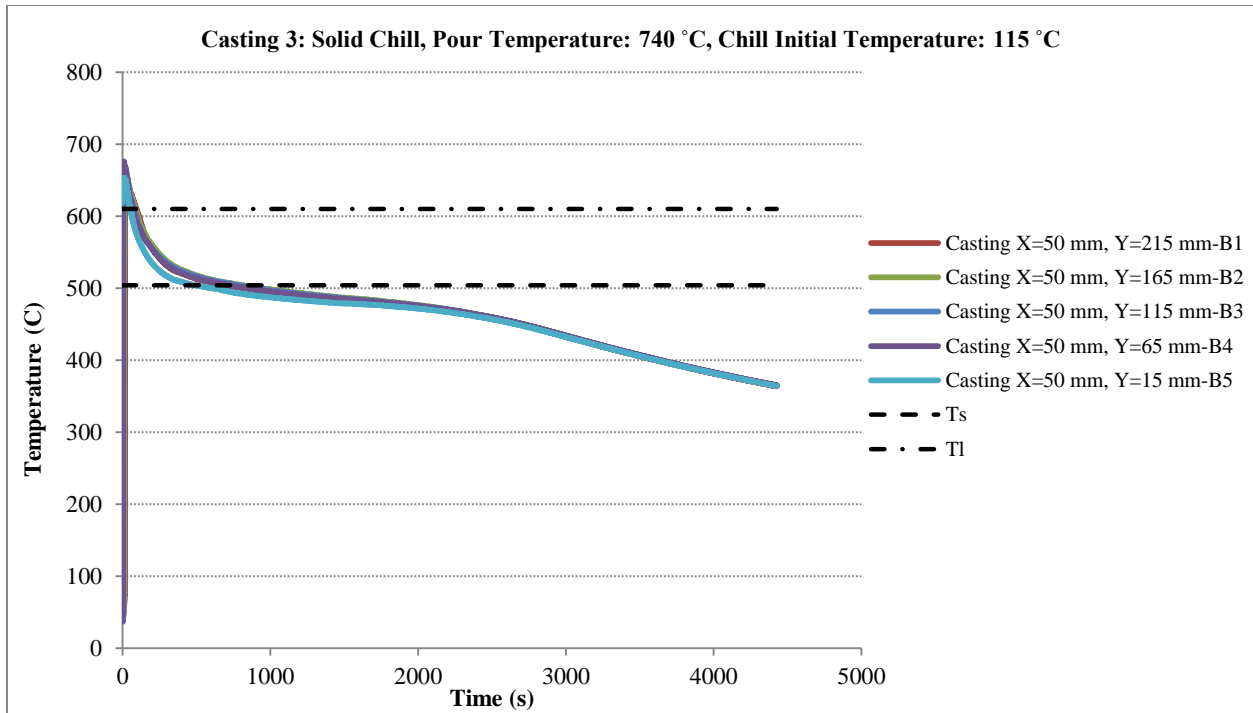


Figure 4.14: Temperature variation with time at various heights, monitoring the buoyancy effect for Casting 3

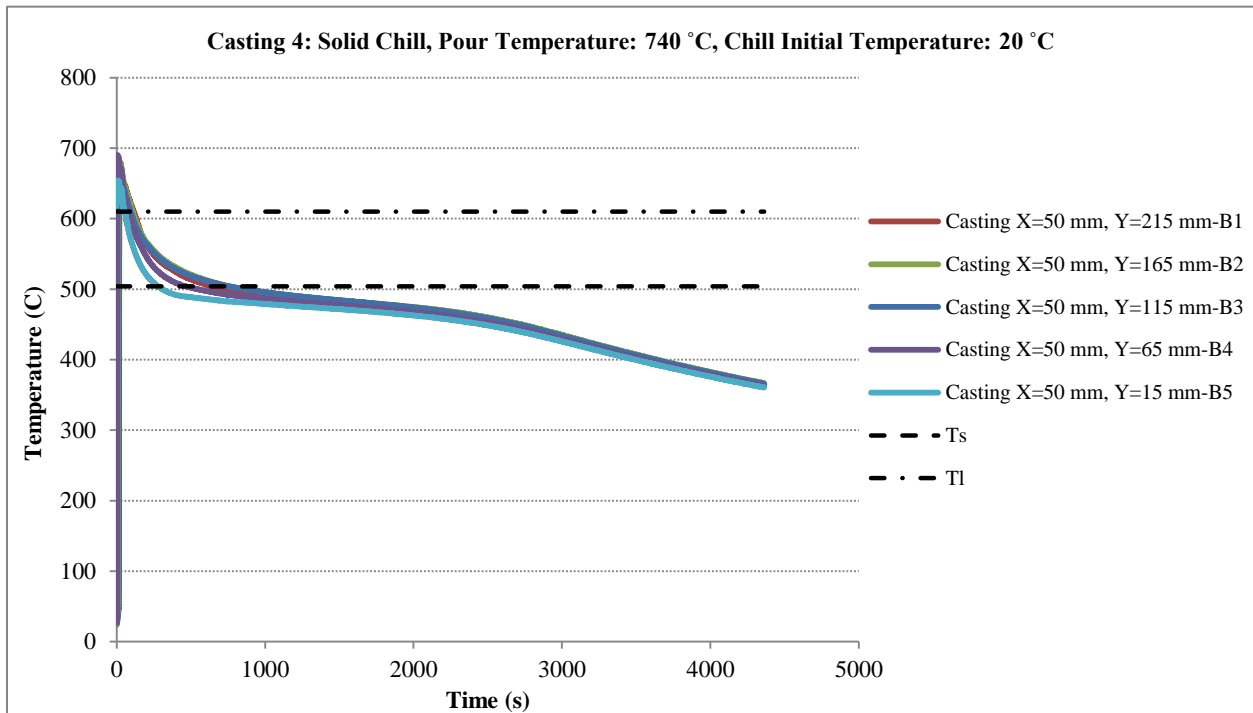


Figure 4.15: Temperature variation with time at various heights, monitoring the buoyancy effect for Casting 4

Effect of Chill Initial Temperature - The thermocouple results for castings 2, 3, and 4, are compared to assess the effect of chill temperature. Figures 4.16 and 4.17 contain the cooling curves for thermocouples located at 5 and 50 mm, respectively. From the cooling curves in Figure 4.16 and 4.17, it can be observed that a change in the initial chill temperature, results in only a small change in the cooling curves at the beginning of the solidification interval and a larger effect toward the end as the temperature approaches the solidus temperature. The observed trend is a decrease in the cooling rate with increasing initial temperature. Comparing Figures 4.16 and 4.17, it can be seen that the cooling rate differences are more significant at the positions farther from the chill.

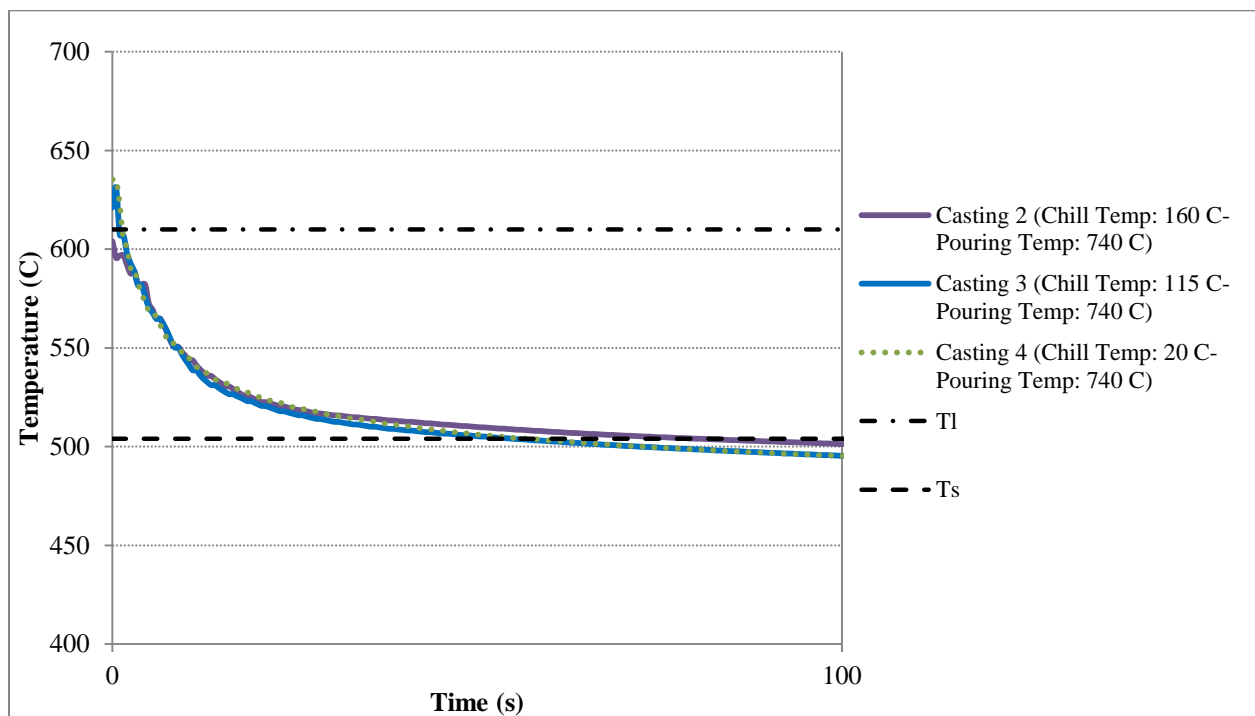


Figure 4.16: Comparison of solid chill condition at 5 mm from chill, varying chill temperature

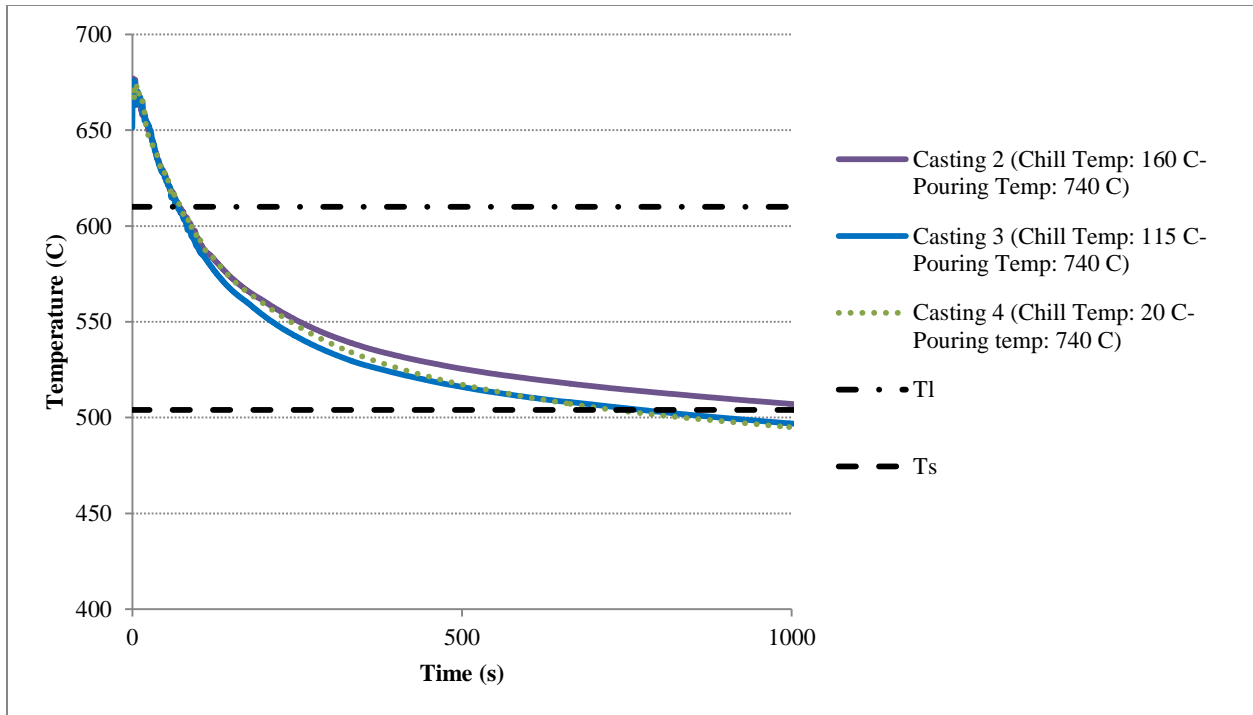


Figure 4.17: Comparison of solid chill condition at 50 mm from chill, varying chill temperature

Effect of Super Heat – To assess the effect of pour superheat, casting 1 and casting 2, which have approximately the same chill temperature, but different pouring temperatures are compared. Figures 4.18 and 4.19 contain the cooling curves for the thermocouples located at 5 and 50 mm from the chill, respectively, for the above-mentioned castings. The amount of super heat has a moderate effect on cooling rate, as is shown in Figures 4.18 and 4.19. This is due to the fact that the mass of the casting is relatively large (18 kg), and so, the change in the super heat has a moderate influence on the amount of heat to be extracted. The trend is to longer solidification times with increase in pour superheat.

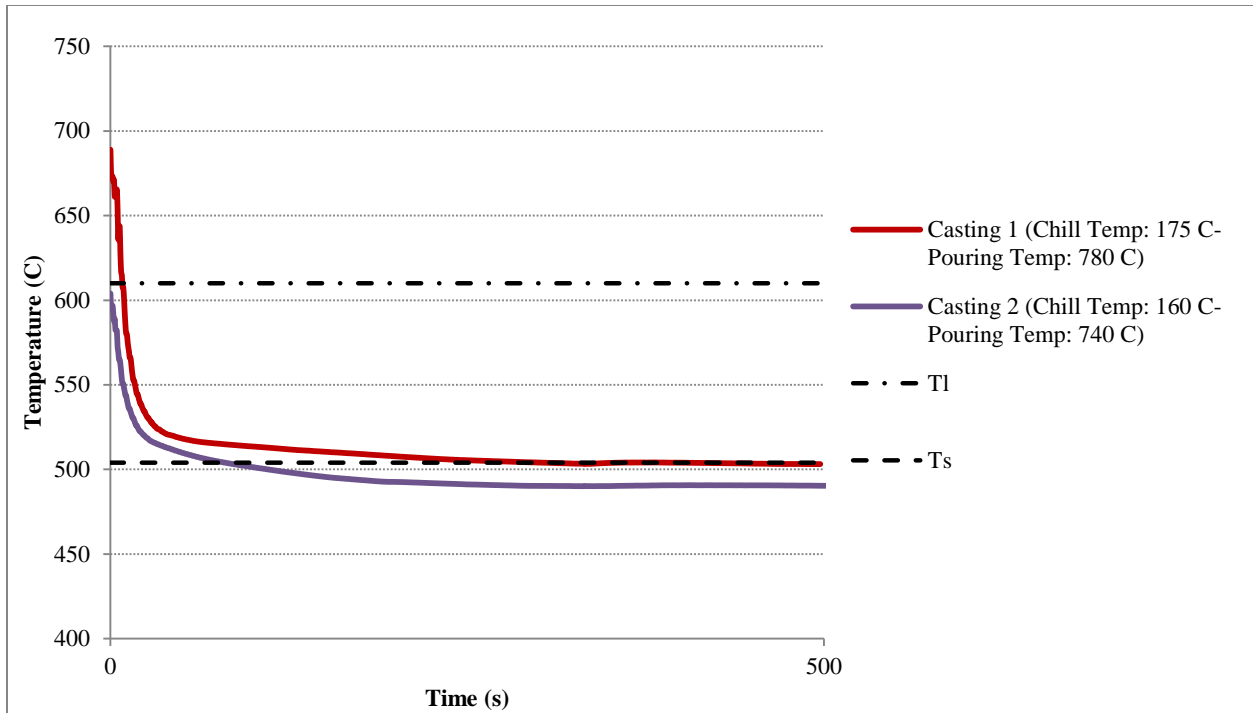


Figure 4.18: Comparison of solid chill condition at 5 mm from chill, varying super heat

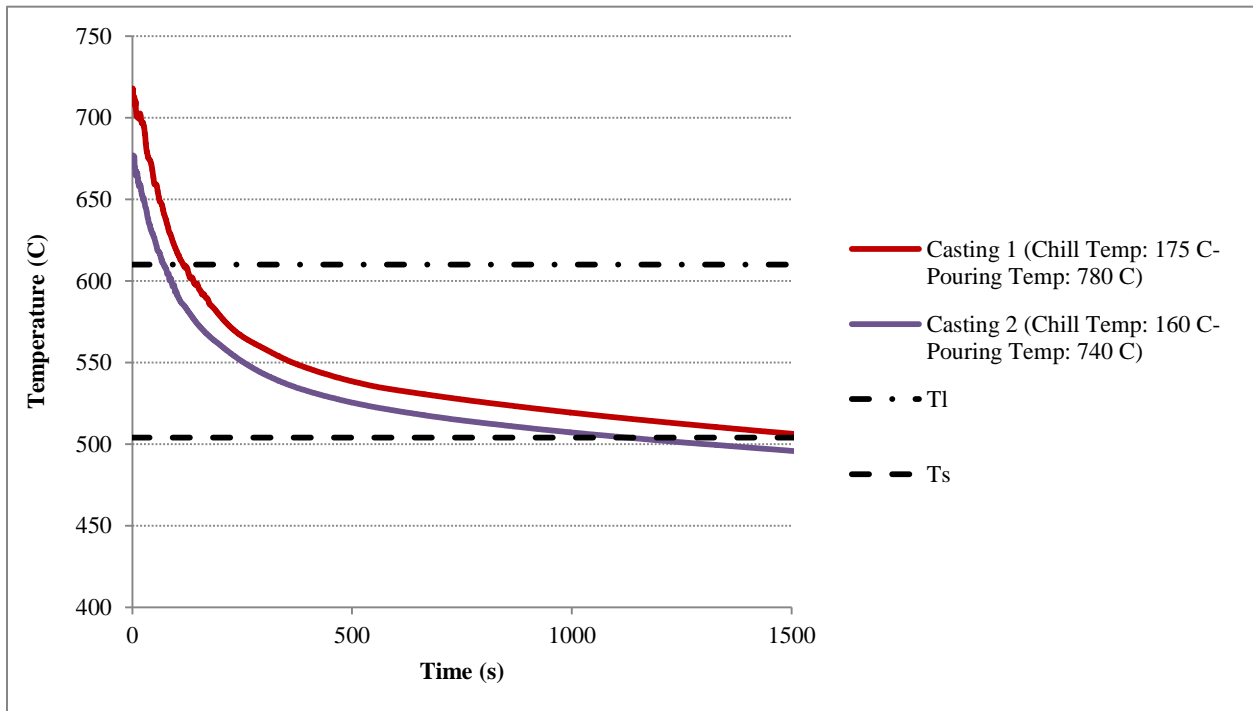


Figure 4.19: Comparison of solid chill condition at 50 mm from chill, varying super heat

4.2.2. Water-Cooled Chill Castings

Figure 4.20 and 4.21 present the results for the water-cooled chill castings. Figure 4.20 shows the results for the standard water-cooled casting and 4.21 for the delayed water-cooled casting. The graphs show a steep temperature drop for the first 500 to 1500 s. The cooling rate gradually decreases up to approximately 2000 s at which point it increases again, likely because the wedge has fully solidified and the “release of the latent heat” has ceased. In comparison to the solid chill experiments a high cooling rate is maintained for a much longer time with the water-cooled chill.

The graphs show a strong dependence of cooling rate with distance from the chill for times less than 2000 seconds, which again is for a much longer duration than in the case of the solid chill. This indicates that a large amount of heat is extracted by the cold chill for a sustained period of time. Beyond 2500 seconds, there is a reduction in the thermal gradient indicating a drop in the rate of heat extraction.

Turning to the graphs for the chill temperatures, they show a small initial increase to a maximum of 70 °C in the first 30 s and then drop to 30 °C where they remain largely unchanged. This is despite the large temperature drop in the casting. This behavior is very different than was observed for the solid chill and reflects the high heat extraction capacity of the water cooling. As is shown in Figure 4.20, there exists a small temperature difference between the three thermocouples located at different heights in the chill in the first 500 s, due to the buoyancy effect.

There is a large difference in temperature between the thermocouples located in the chill and those close to the interface in the casting from the beginning of the casting process. This is because of the resistance at the interface and the high capacity of the water-cooled chill to extract heat, which maintains the chill at a low temperature. The formation of a gap at the interface is less obvious than for the solid chill, but may be what causes the temperature to drop in the chill at approximately 30 s. A more detailed analysis of the development of the interface resistance is presenting in Chapter 6.

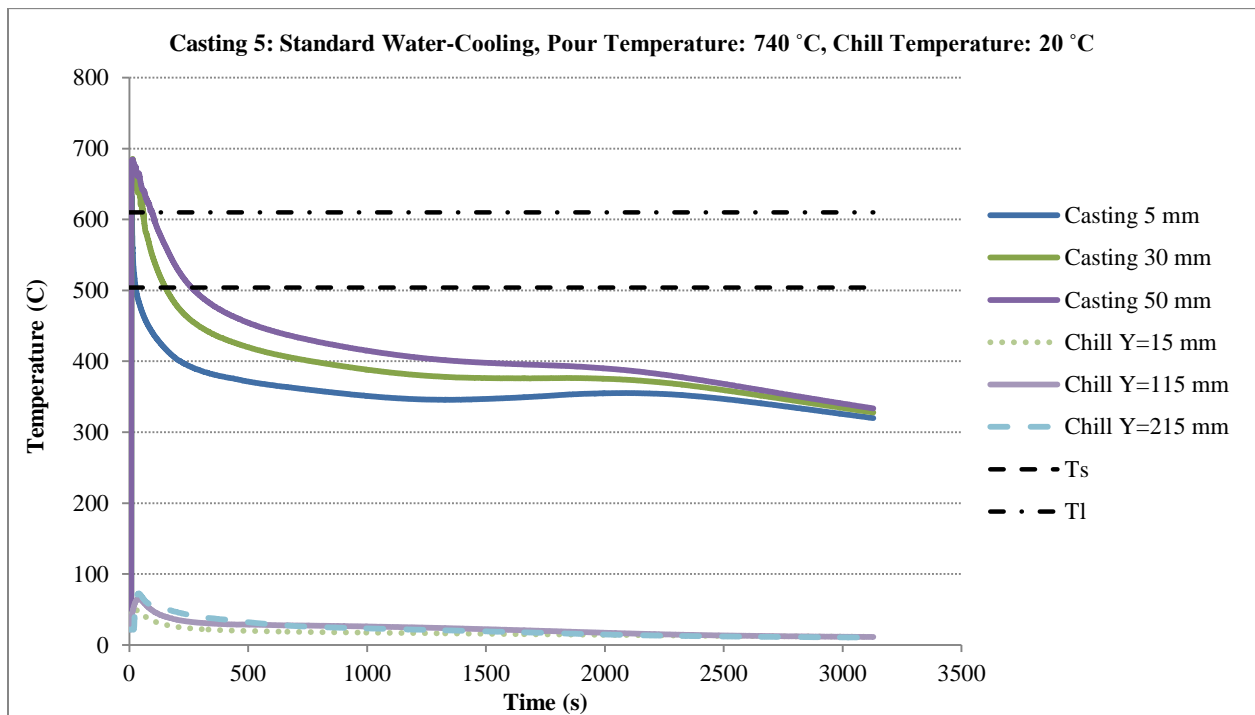


Figure 4.20: Variation in temperature with distance from chill and within the chill¹

¹ The 1 cm data is not inserted due to thermocouple failure during the experimental procedure

Similar to the solid chill castings, no temperature variation with height was observed for the thermocouples located above mid-height in the case of casting 5.

Figure 4.21 presents the cooling curves for the delayed water-cooled experiment. The graphs show a steep temperature drop for the first 500 to 1500 s similar to what was observed in the standard water-cooled experiment. However, on close inspection there are some significant differences. Referring to Figure 4.22, which shows an expanded view of the first 500 seconds, it can be seen that the cooling rate for the 5 mm and 10 mm thermocouples is reduced for the first 30 s and then increases reflecting the effect of the water-cooling being switched on, 10 seconds after the mold is filled. From 500 to 2000 s the rate of temperature change decreases. During this time, there can be seen a reduction in the thermal gradients with distance from the chill, as would be expected.

Another significant difference is that the chill temperature increases to a maximum of 230 °C during the early part of casting reflecting the absence of water-cooling in the first 10 seconds after the mold cavity is filled. As can be seen from the curves, there is a large difference in temperature between the thermocouples located in the chill and those close to the interface in the casting similar to what was observed in the solid chill. The formation of a gap at the interface in this case is not apparent compared to the drop in temperature in the chill due to the introduction of water-cooling.

Similar to the solid chill and standard water-cooled chill castings, no temperature variation with height was observed for the thermocouples located above mid-height in the case of casting 6.

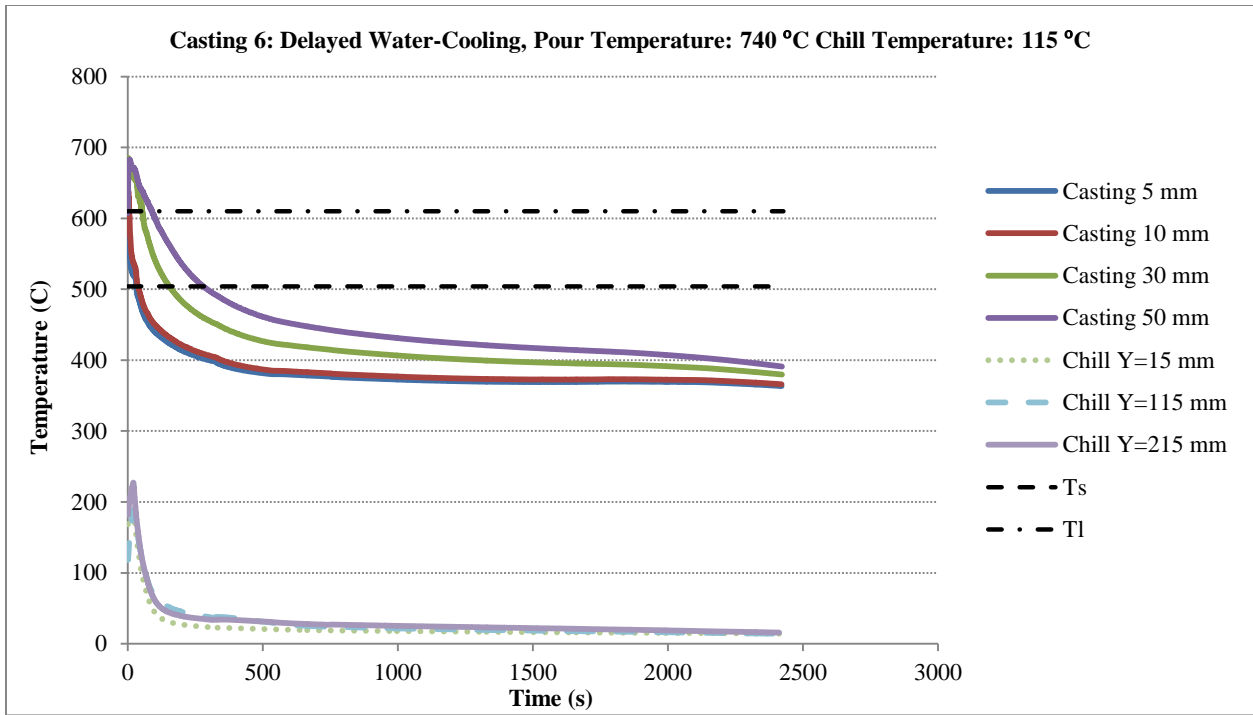


Figure 4.21: Variation in temperature with distance from chill and within the chill

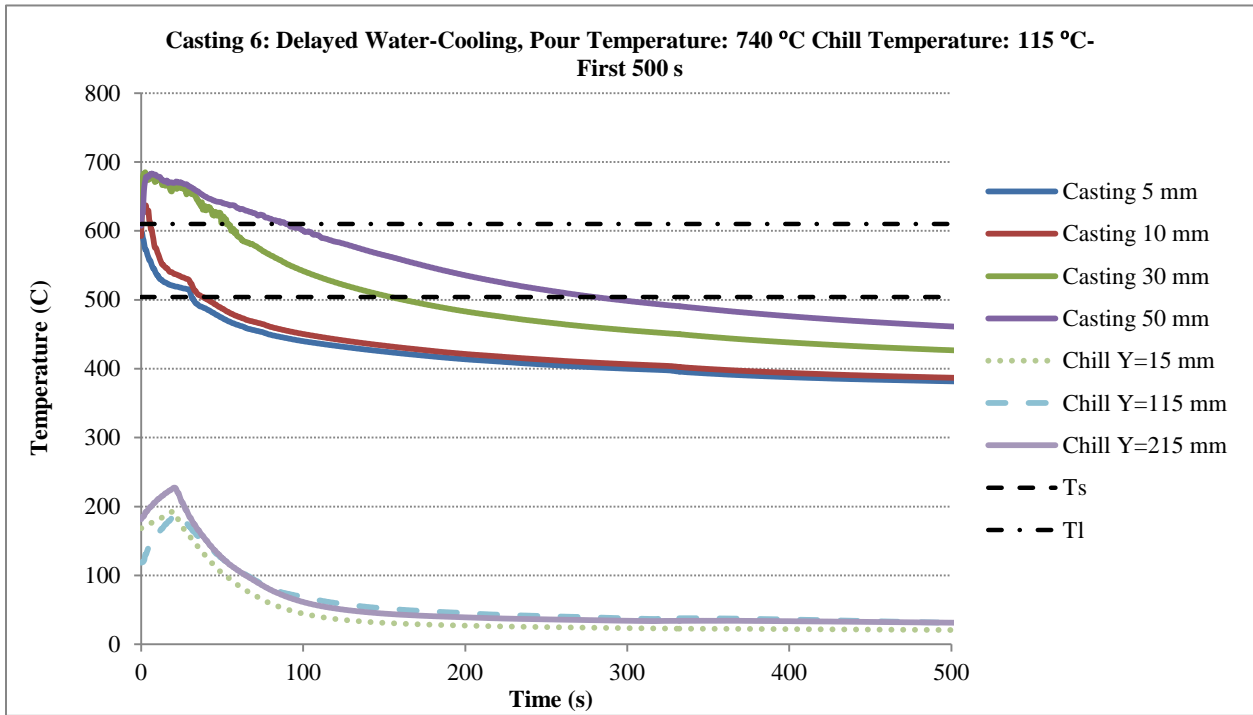


Figure 4.22: Variation in temperature with distance from chill and within the chill, for the first 500 seconds

4.2.3. The Effect of Water Cooling on Cooling Rate

Figures 4.23 – 4.25 present a comparison between the thermocouple results for casting 4 and casting 5. Casting 4 employed a solid chill and casting 5 the standard water-cooled chill. Both castings had the same casting conditions (i.e. same pouring temperature and same initial chill temperature). Figure 4.23, 4.24, and 4.25 present the results for the thermocouples located at 5, 30, and 50 mm from the chill, respectively. The cooling curves are limited to the temperature range between solidus temperature and liquidus temperature. These graphs show that increasing the heat extraction capacity of the chill by means of water-cooling results in a significant increase in the cooling rate of the casting and a reduction in the solidification time, which results in finer microstructures as presented in a subsequent section. The solidification time at 5 mm is reduced from 46 to 13 s, at 30 mm from 328 to 93 s, and for 50 mm from 657 to 166 s.

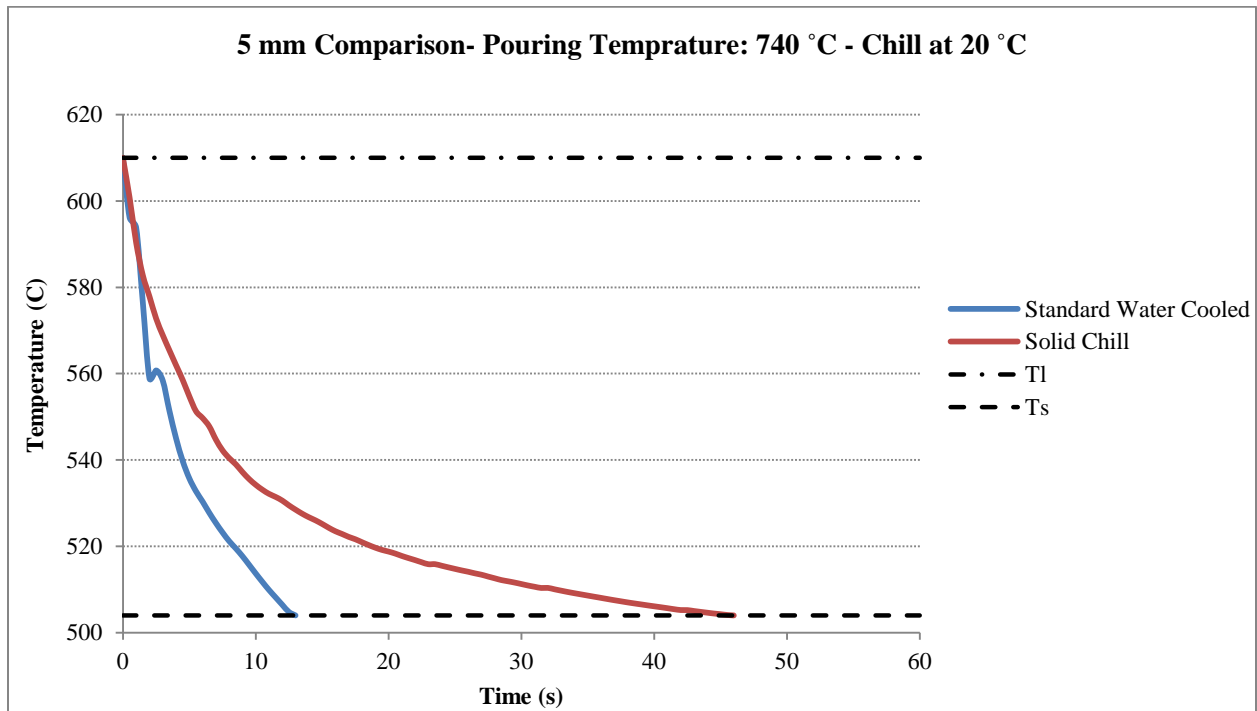


Figure 4.23: Cooling curve comparison between “Solid chill” and “Standard Water-Cooled chill” conditions

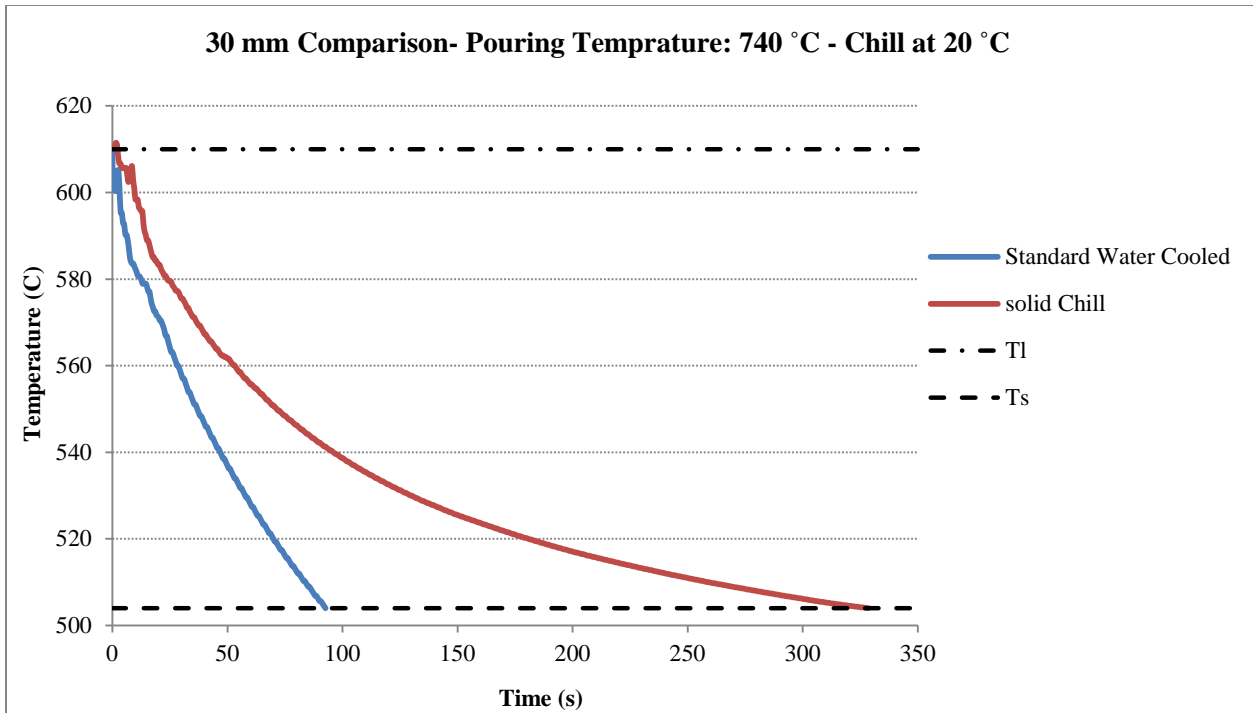


Figure 4.24: Cooling curve comparison between “Solid chill” and “Standard Water-Cooled chill” conditions

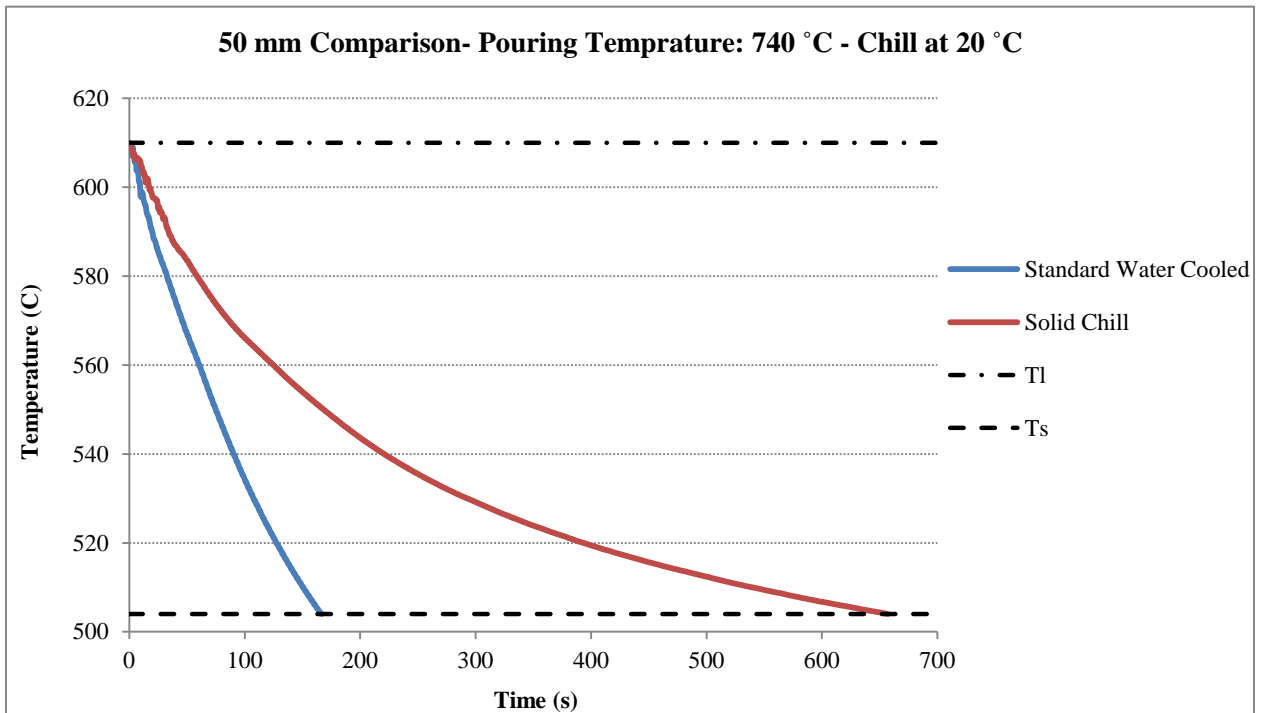


Figure 4.25: Cooling curve comparison between “Solid chill” and “Standard Water-Cooled chill” conditions

4.2.4. Effectiveness of Delay Time

To investigate the effectiveness of delaying the cooling in achieving a reduced initial cooling rate in the thermocouples in proximity to the chill and increasing the cooling rate for the thermocouples located farther from the chill the results from castings 3 and 6 have been compared. The results for the thermocouple located at 5 mm from the chill are presented in Figure 4.26 and the results for 30 and 50 mm are presented in Figures 4.27 and 28, respectively. The cooling curves are limited to the temperature range between solidus and liquidus temperatures. The casting conditions with respect to the pour temperature and initial chill temperature are the same. As can be seen in Figure 4.26, prior to the start of water-cooling at 30 s, the thermocouples located at 5 mm distance from the chill show that the cooling rates are the same in the two castings and that the delay time has been effective in maintaining the cooling rate the same as the solid chill in the thermocouples located at 5 mm from the chill.

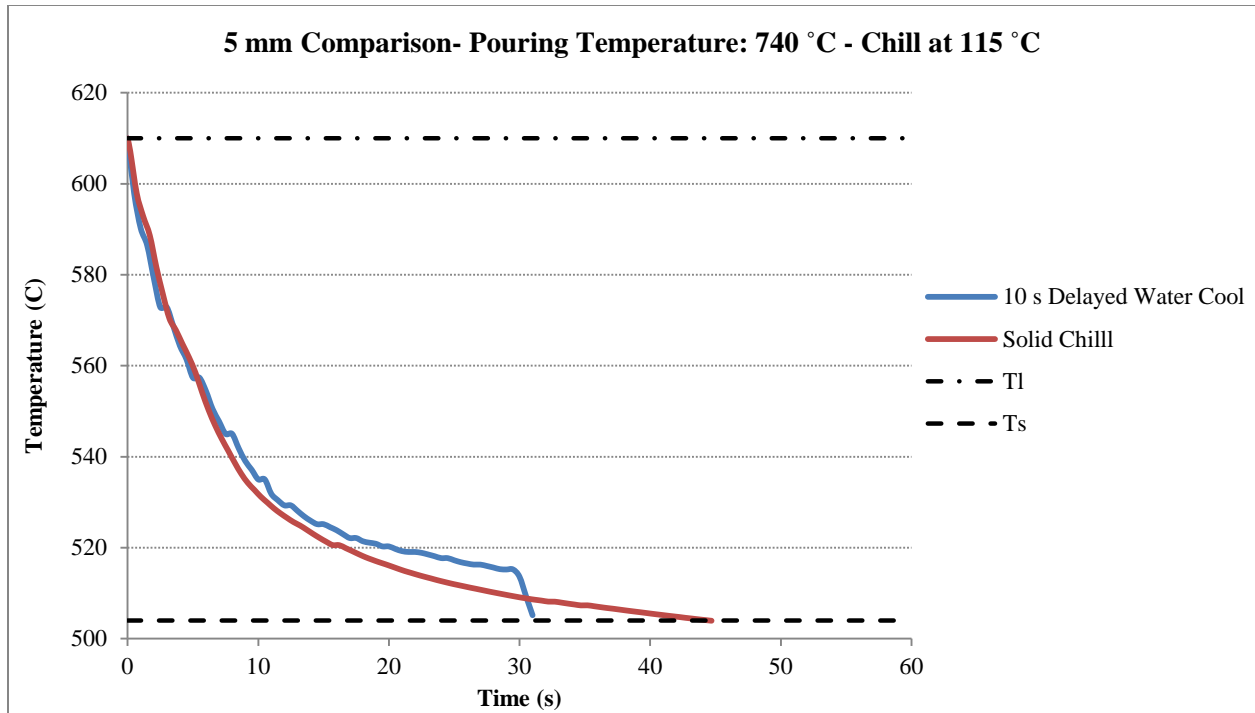


Figure 4.26: Cooling curve comparison between “Solid chill” and “Delayed Water-Cooled chill” conditions

The results presented in Figures 4.27 and 4.28 show that switching the water on after a 10 seconds delay was effective in increasing the cooling rate and decreasing the solidification time at 30 and 50 mm from the chill. The solidification time at 30 mm decreased from 427 to 101 s, and at 50 mm from 703 to 190 s. These results show that this method has the potential to both avoid cold shuts and miss-runs and improve the cast microstructure farther into castings remote from the chill.

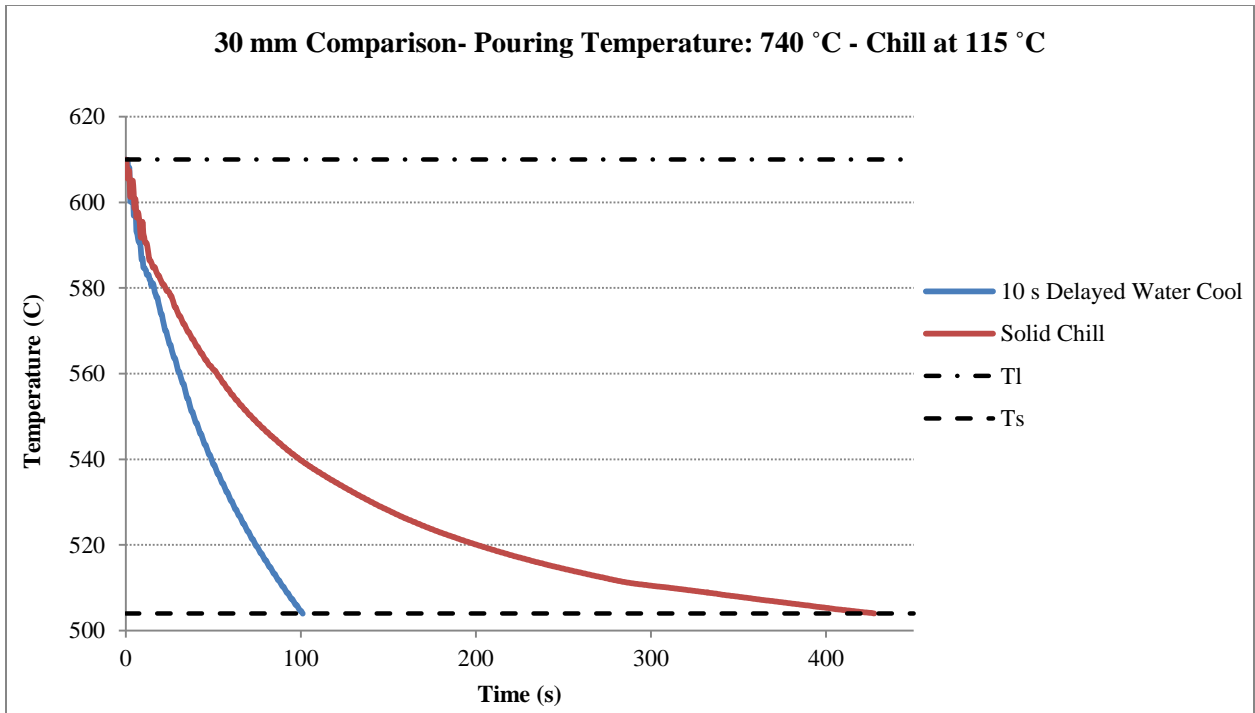


Figure 4.27: Cooling curve comparison between “Solid chill” and “Delayed Water-Cooled chill” conditions

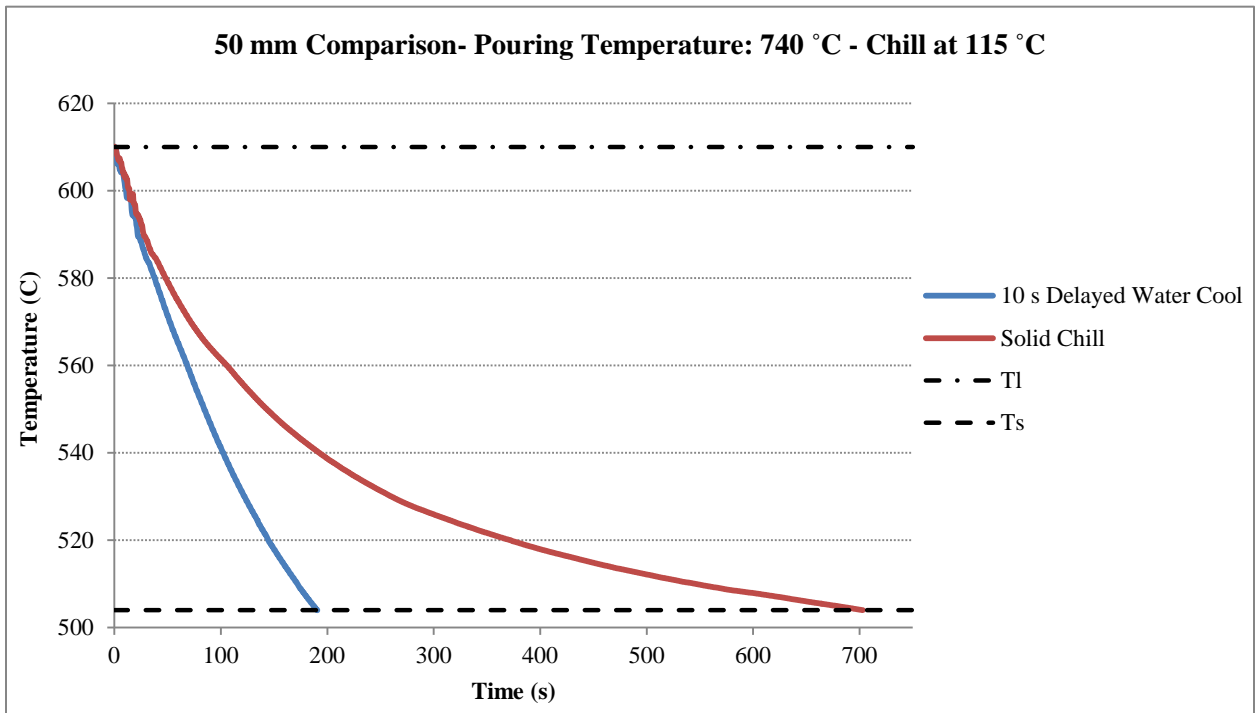


Figure 4.28: Cooling curve comparison between “Solid chill” and “Delayed Water-Cooled chill” conditions

4.2.5. SDAS Size Comparison

In order to investigate and quantify the effect of cooling rate on microstructure, a mathematical relationship between the cooling rate and SDAS size has been derived. For this purpose, five metallographic specimens at 5, 10, 30, 50, and 150 mm from the chill was taken from the central vertical plane of castings 1 and 5. Casting 1 has the lowest cooling rate, and casting 5 has the highest cooling rate among all the castings, as was discussed in previous sections.

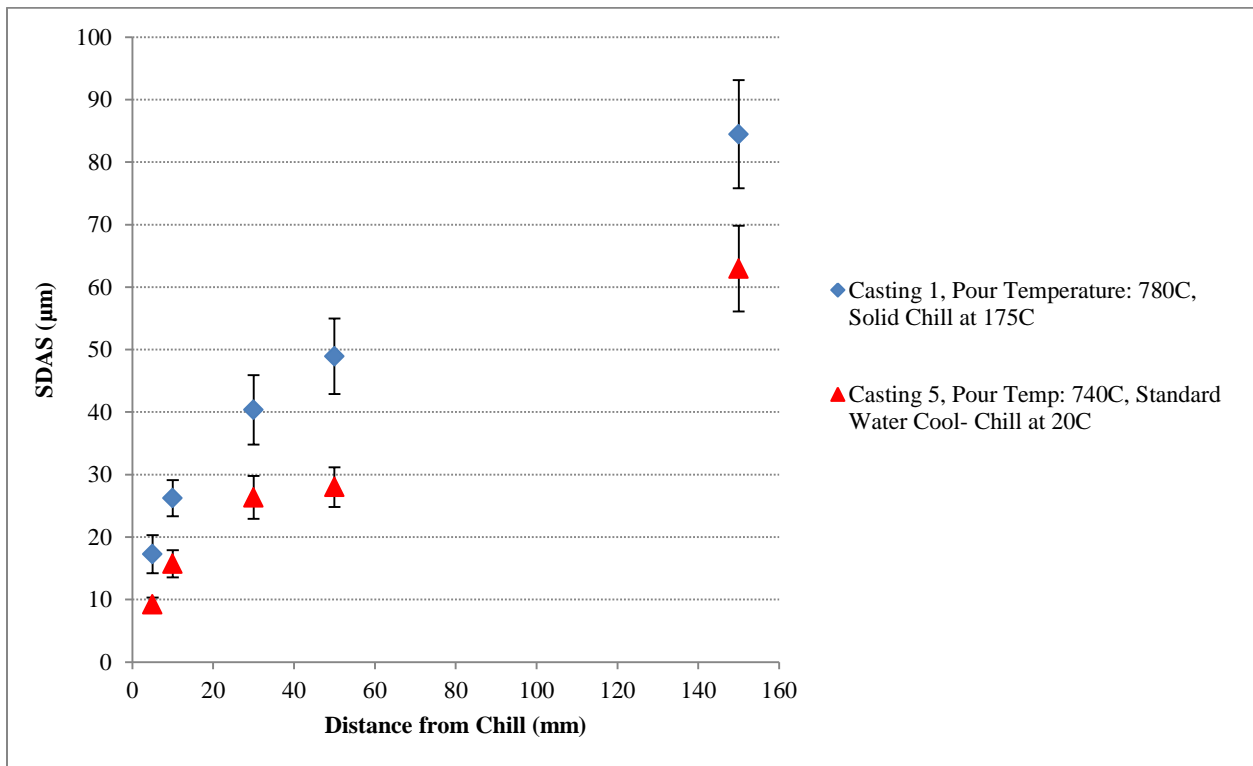


Figure 4.29: The variation of SDAS with distance from the chill

Figure 4.29 shows the SDAS size variation with distance from the chill for the case of casting 1 and casting 5. As can be seen, the microstructure of the solidified casting becomes progressively coarser with increasing distance from the chill. Also, the comparison between the results for the

two castings clearly shows that the SDAS sizes for the standard water-cooled chill condition are significantly lower than that of the solid chill case. The decreases in SDAS are more pronounced at the locations farther from the chill.

Flemings [31] suggested a mathematical relationship between SDAS and cooling rate as shown below:

$$SDAS = a(CR)^{-n}, 0.3 < n < 0.5 \quad (4.1)$$

where CR is the cooling rate ($^{\circ}C/s$), and a is a constant.

In order to calculate the cooling rate, two different approaches were used. The first approach is based on the average cooling rate prior to eutectic nucleation, and was calculated by:

$$CR = \frac{T_{Liquidus} - T_{EutecticNucleation}}{t_{Liquidus} - t_{EutecticNucleation}} \quad (4.2)$$

where $T_{EutecticNucleation}$ is the temperature ($^{\circ}C$) at which the nucleation of the Eutectic phase starts at the location being analyzed, $t_{Liquidus}$ is the time (s) at which the melt is at liquidus temperature, and $t_{EutecticNucleation}$ is the time (s) at which the melt is at the temperature of eutectic reaction. This assumes no significant change in the SDAS occurs at temperatures below the eutectic temperature.

On the other hand, it is known that growth of the α -phase and coarsening can continue after the start of eutectic reaction. Hence, the second approach is based on the average cooling rate over

the entire solidification range – i.e. from the liquidus to solidus temperatures - and was calculated by the following expression:

$$CR = \frac{T_{Liquidus} - T_{Solidus}}{t_{Liquidus} - t_{Solidus}} \quad (4.3)$$

where $t_{Solidus}$ is the time (s) at which the solidification is complete at the location being analyzed. Figures 4.30 and 4.31 show the variation of SDAS with cooling rate for the two approaches, respectively.

As can be seen from Figure 4.30, the mathematical relationship between SDAS and cooling rate given in Equation 4.2 matches the relationship suggested by Flemings quite well, yielding values for a and n of 29.25 and -0.38, respectively. The R^2 value for this fitting is 0.94.

$$SDAS = 29.25(CR)^{-0.38} \quad (4.4)$$

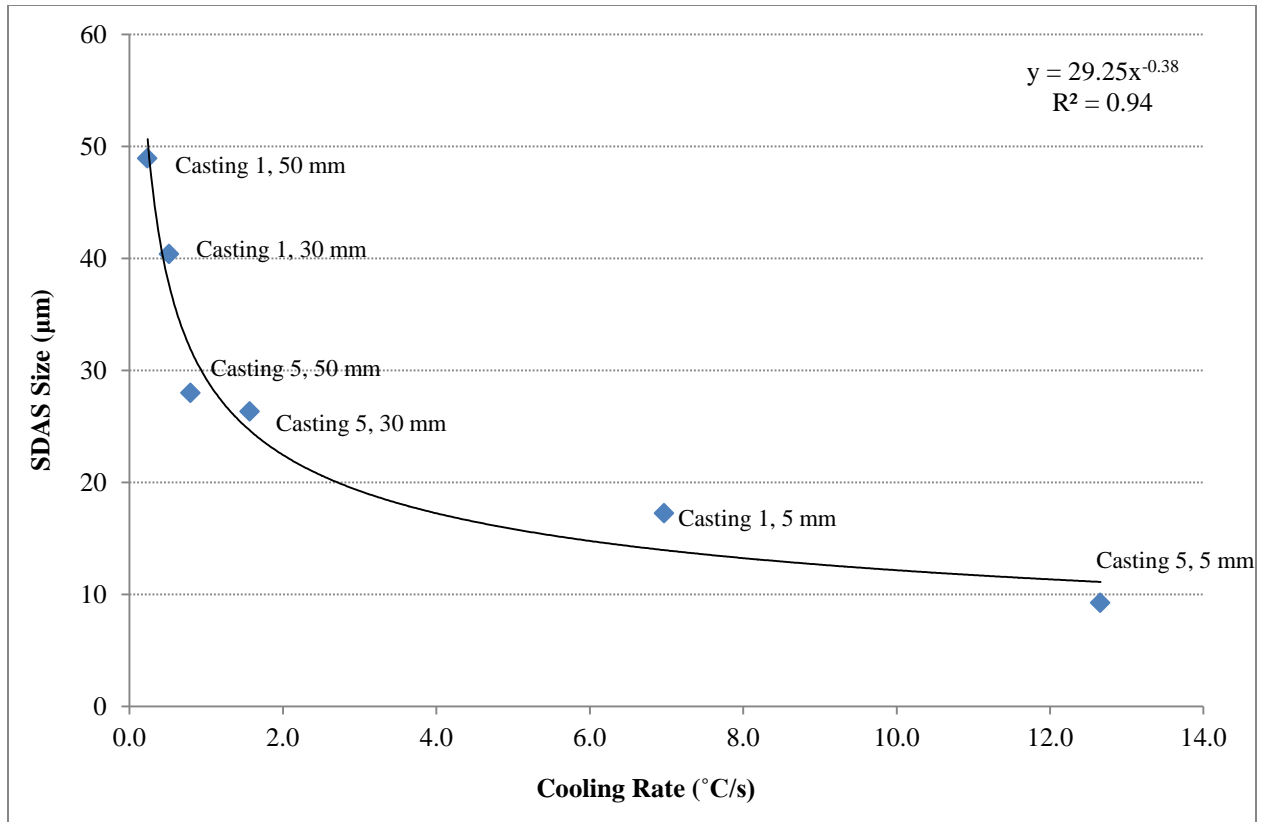


Figure 4.30: The variation of SDAS with cooling rate between liquidus and eutectic temperatures

Alternatively, Figure 4.31 shows the correlation for SDAS variation based on the cooling rate obtained from Equation 4.3. The values for a and n are 25.68 and -0.45, respectively, with an R^2 value of 0.97. Equation 4.5 shows the correlation.

$$SDAS = 25.68(CR)^{-0.45} \quad (4.5)$$

Based on the R^2 values reported for the two cases, the second approach is more suitable for calculating the cooling rate from the fitting approach.

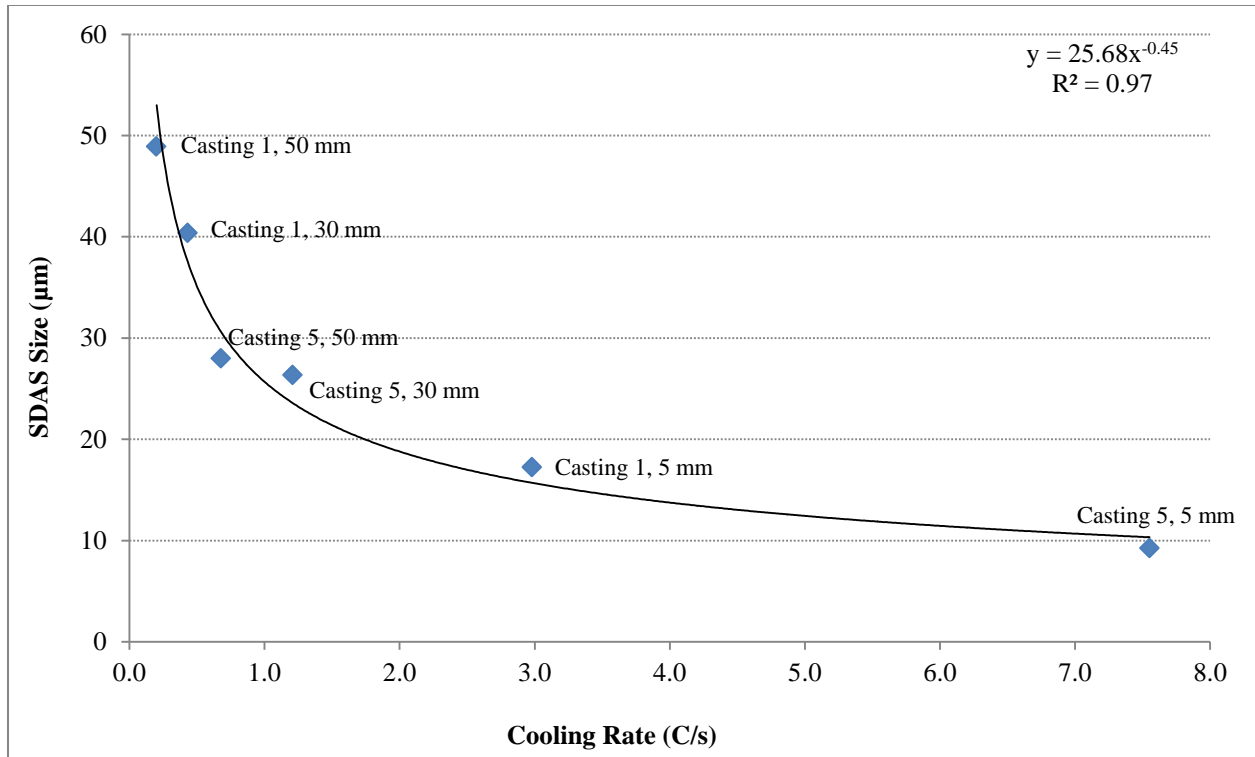


Figure 4.31: The variation of SDAS with cooling rate between solidus and liquidus temperatures

Figures 4.32 - 4.36 compare the microstructural optical microscope images at 5, 10, 30, 50, and 150 mm from the chill, respectively. In each figure, caption *a*, refers to casting 1 and caption *b* refers to casting 5. As can be observed from these figures, the dendrite arm spacings at all the above-mentioned locations for Casting 1 are obviously larger than that of Casting 5. This qualitative comparison is supported by the quantitative data previously discussed in the current section.

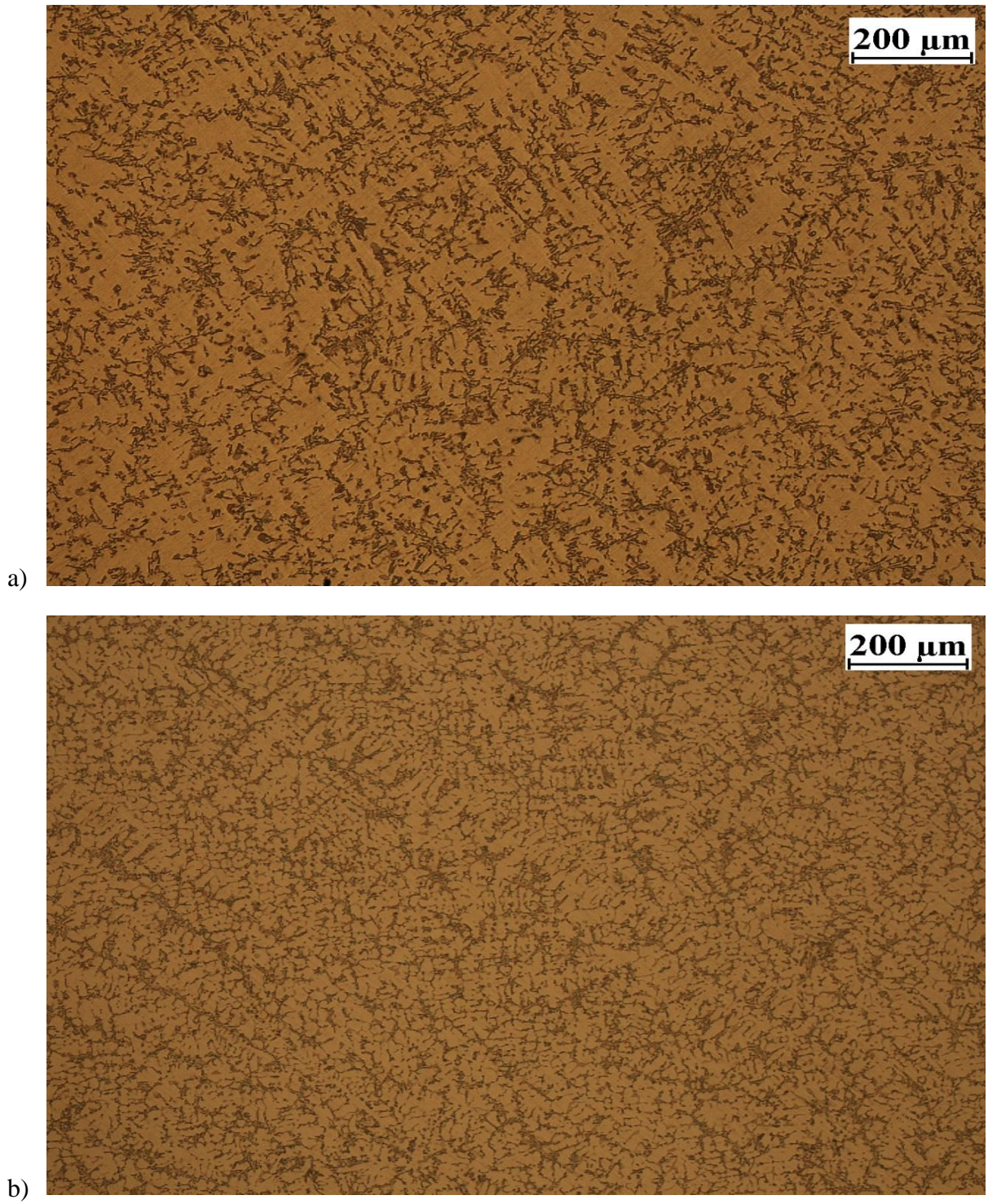


Figure 4.32: The microstructure of a) Casting 1 and b) Casting 5 at 5 mm distance from the chill

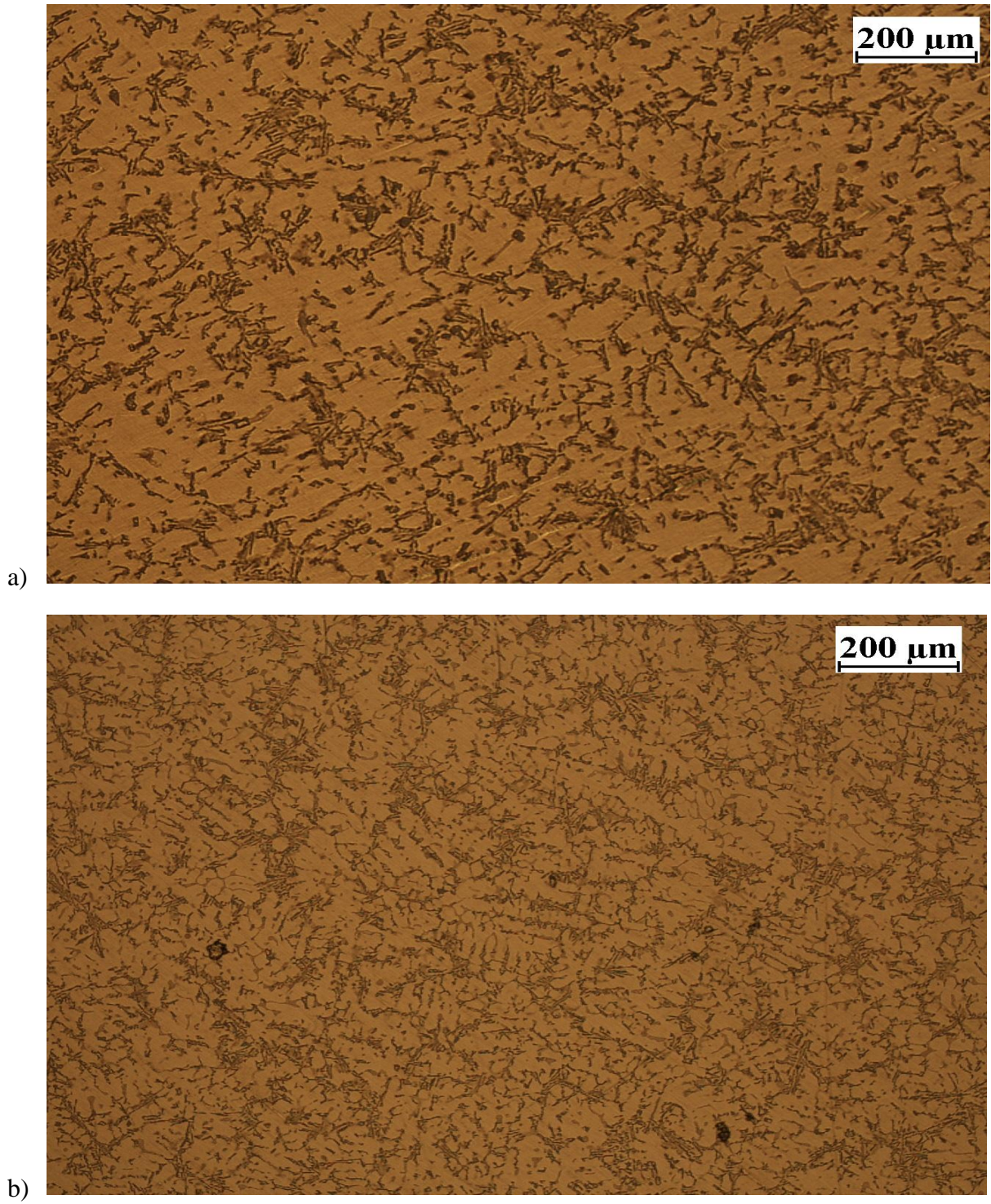


Figure 4.33: The microstructure of a) Casting 1 and b) Casting 5 at 10 mm distance from the chill

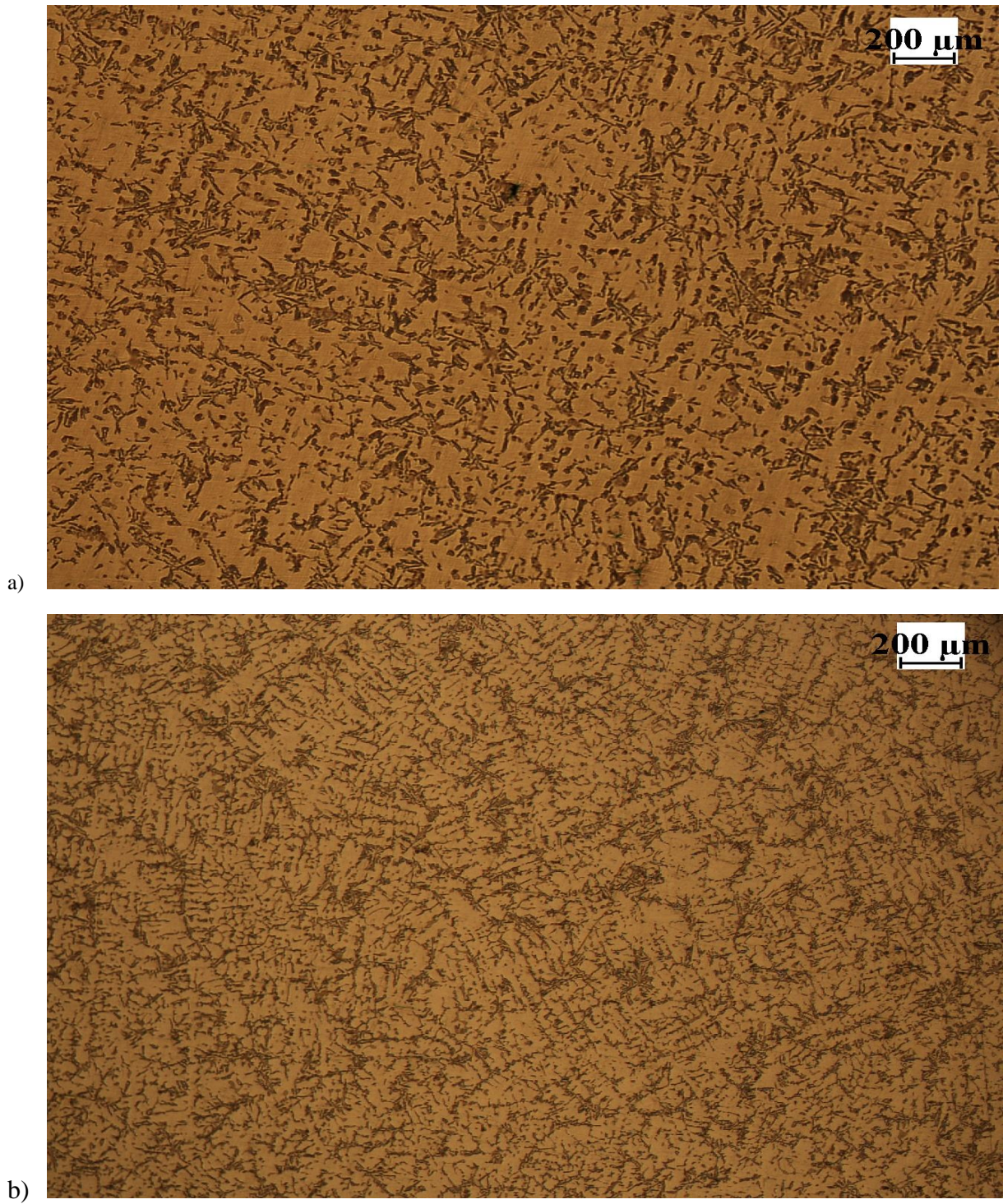


Figure 4.34: The microstructure of a) Casting 1 and b) Casting 5 at 30 mm distance from the chill

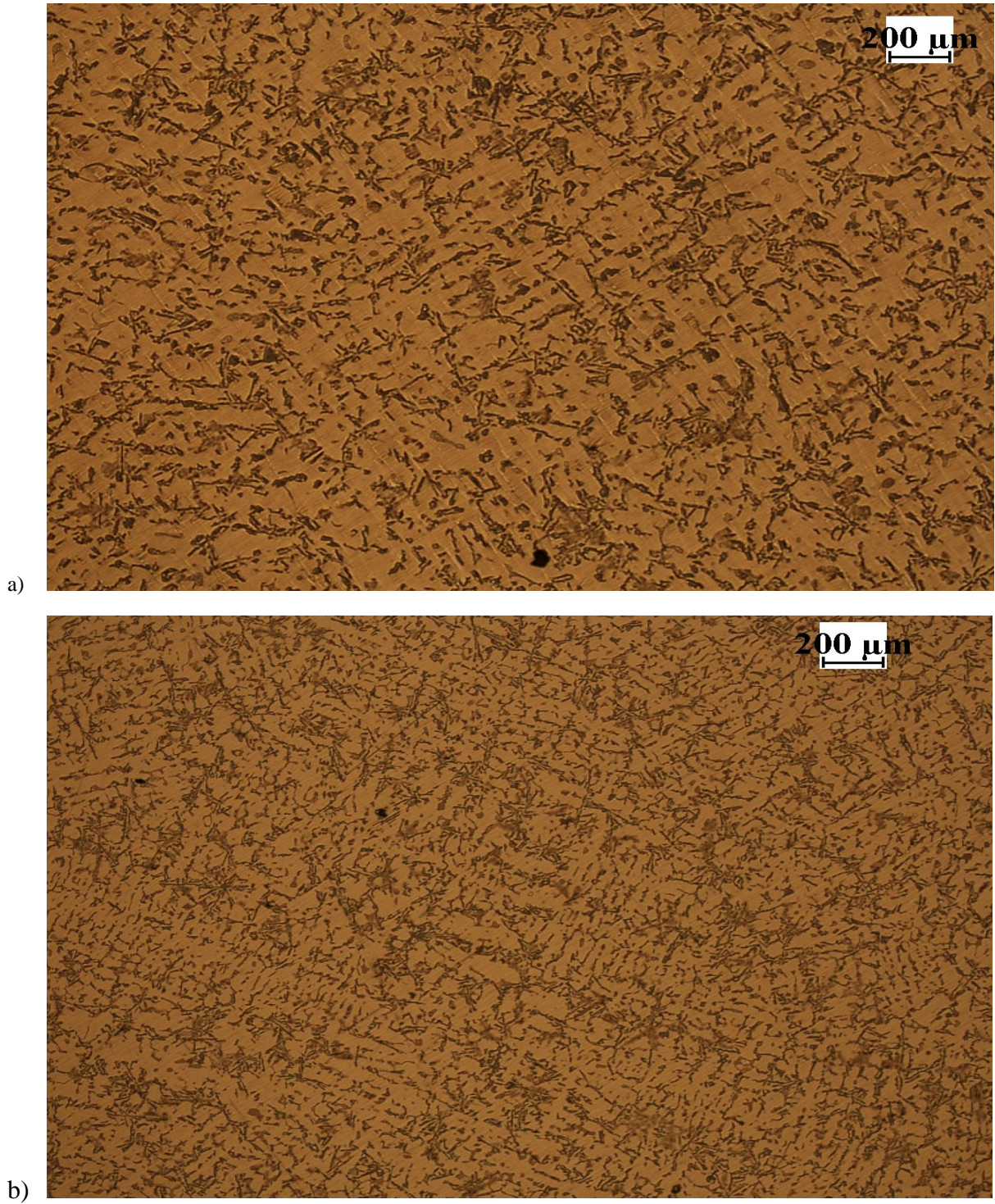


Figure 4.35: The microstructure of a) Casting 1 and b) Casting 5 at 50 mm distance from the chill

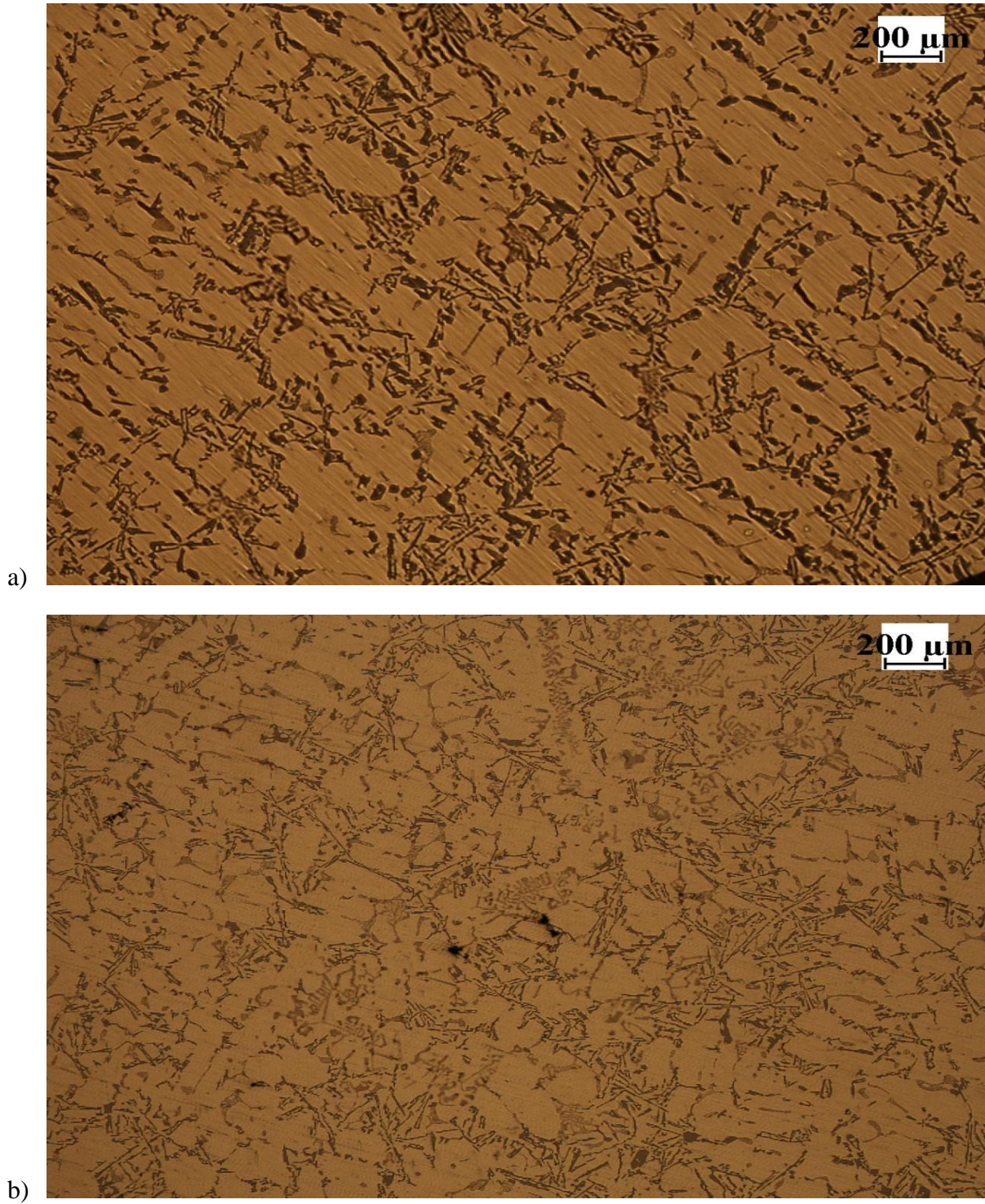


Figure 4.36: The microstructure of a) Casting 1 and b) Casting 5 at 150 mm distance from the chill

5. Development of the Computational Model

The following six steps associated with model development will be discussed in this chapter:

1) The governing equations describing conservation of energy, 2) the domain, 3) the solution technique and mesh, 4) the material properties, 5) the initial and boundary conditions, and 6) model control parameters.

5.1. Governing Equations

One of the concerns with the particular geometry used for the wedge casting, which has the chill placed at the side, is that the large gradient in temperature adjacent to the chill could give rise to a significant buoyancy force leading to a downward flow of liquid adjacent to the chill and recirculating flow within the casting. Since the thermocouple results presented in Chapter 4, section 4.2, do not show a significant change in the cooling curves with height, such as would result from a recirculating flow, fluid flow may be ignored. Hence, the model developed for analysis of the chill castings is heat transfer based, and the only conservation equation applicable in this situation is the conservation of energy, Equation 5.1:

$$\frac{\partial(\rho H)}{\partial t} = \frac{\partial}{\partial x} \left(k \frac{\partial T}{\partial x} \right) + \frac{\partial}{\partial y} \left(k \frac{\partial T}{\partial y} \right) + \frac{\partial}{\partial z} \left(k \frac{\partial T}{\partial z} \right) \quad (5.1)$$

where ρ ($\text{kg}\cdot\text{m}^{-3}$) is density, H ($\text{J}\cdot\text{kg}^{-1}$) is enthalpy, T (K) is temperature, k ($\text{W}\cdot\text{m}^{-1}\cdot\text{K}^{-1}$) is thermal conductivity, t (s) is time, and x , y , and z (m) are distance [74].

Equation 5.1 can also be expressed as:

$$\frac{\partial \bar{\rho} C'_p T}{\partial t} = \frac{\partial}{\partial x} \left(k \frac{\partial T}{\partial x} \right) + \frac{\partial}{\partial y} \left(k \frac{\partial T}{\partial y} \right) + \frac{\partial}{\partial z} \left(k \frac{\partial T}{\partial z} \right) \quad (5.2)$$

where $\bar{\rho}$ ($\text{kg}\cdot\text{m}^{-3}$) is the density of the alloy in the liquid state, mushy zone (mixture of solid and liquid), and solid state, and defined as:

$$\bar{\rho} = f_s \rho_s + f_l \rho_l \quad (5.3)$$

where f_s and f_l , defined in the subsequent section, are the fraction solid and the fraction liquid, respectively.

Also, the effective specific heat capacity, C'_p , is defined as:

$$C'_p = C_p - \frac{\partial f_s}{\partial T} L_m \quad (5.1.4)$$

In this equation C_p ($\text{J}\cdot\text{kg}^{-1}\cdot\text{K}^{-1}$) is the specific heat capacity, L_m ($\text{J}\cdot\text{kg}^{-1}$) is the latent heat of fusion.

5.2. Model Domain

The melt and chill geometries were created separately, as shown in Figure 5.1 for the solid chill and Figure 5.2 for the water cooled chill. The thermal field was assumed to be symmetric about a vertical plane bisecting the casting and hence only one-half of the geometry was considered in order to reduce the computational size of the problem. Further reductions in the computational size were obtained by limiting the analysis to a 2-D slice at approximately mid-height and by

ignoring the sand mold. Limiting the analysis to a 2-D slice was justified based on the lack of a vertical gradient observed in the thermocouple measurements. The 2-D slice is oriented as presented in Chapter 4, section 4.1. The sand mold could be ignored, as the analysis was limited to the solidification range in proximity to the chill where the mold would have a limited effect on the evolution of temperature.

ANSYS CFX does not allow the analysis of 2-D structures and hence the “2-D slice” was taken to be a planar section 2 mm in thickness.

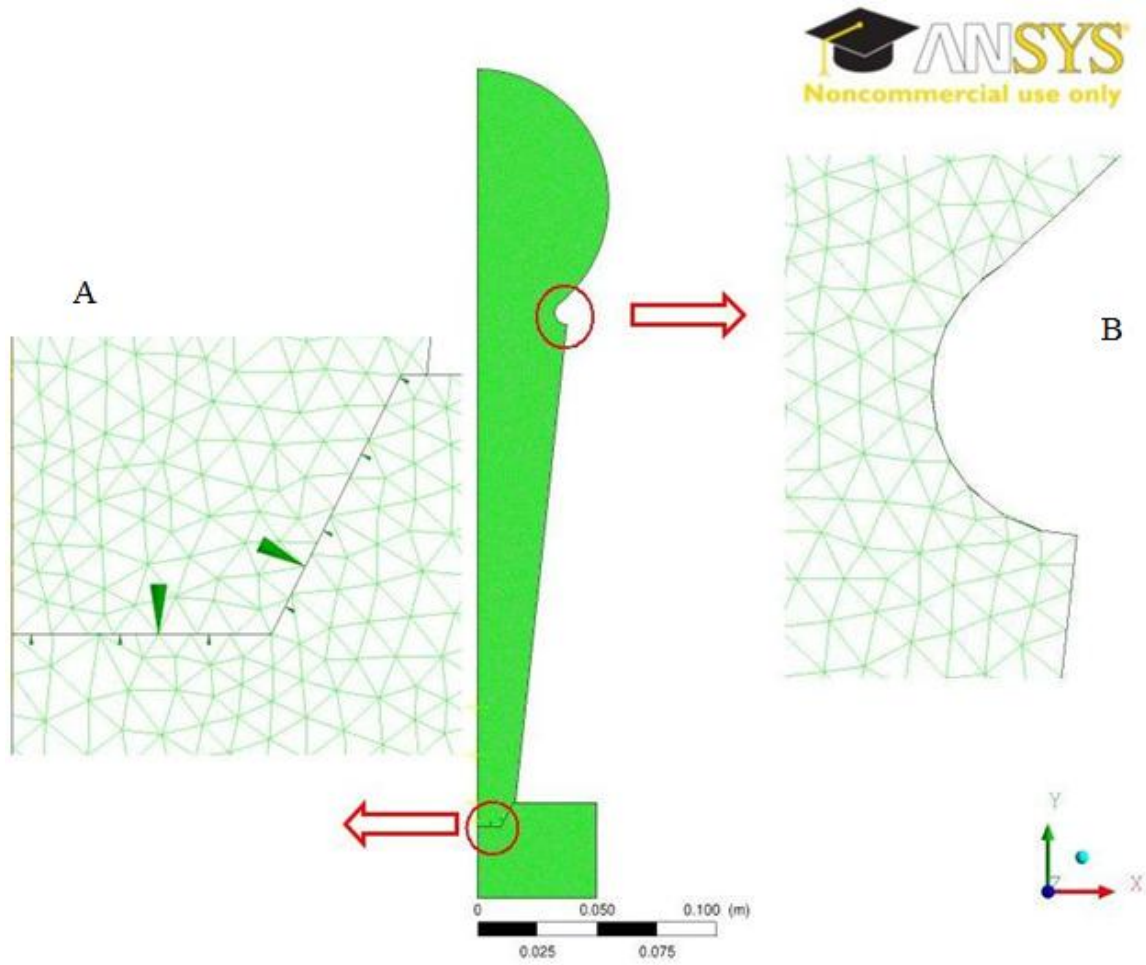


Figure 5.1: The meshed geometry of solid chill condition, Z is the vertical axis in the experiments

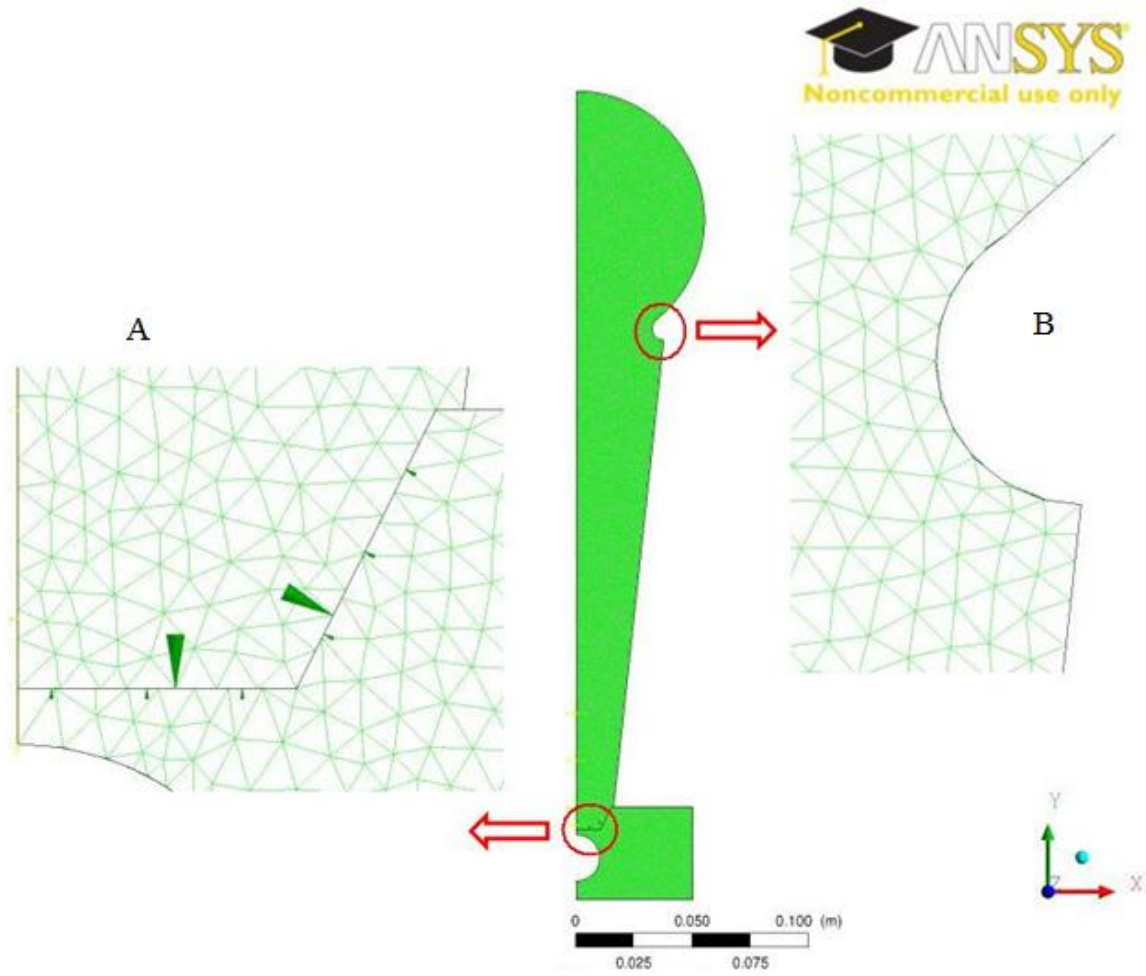


Figure 5.2: The meshed geometry of water-cooled condition, Z is the vertical axis in the experiments

5.3. Solution Technique and Mesh

The commercial computational fluid dynamics package ANSYS¹ CFX² version 12.1 was used to solve the problem subject to initial and boundary conditions, which are defined in subsequent sections. ANSYS CFX uses the finite volume method to solve Eq. 5.1 and hence the domain is discretized resulting in a mesh containing elements and nodes. To mesh the domain, the geometry created in ANSYS WORKBENCH³ was imported to ICEM CFD⁴ meshing software. The mesh statistics are shown in Table 5.1.

Figures 5.1 and 5.2 show the example mesh topographies in two areas within the domain. Expanded view “A” in both these figures shows the mesh topography at the Casting/Chill interface, and the expanded view “B” the mesh topography at a curved area. In the expanded view A, the mesh topography at the interface shows both coincident nodes – i.e. nodes belonging to the casting domain and nodes belonging to the chill domain that share the same location - and non-coincident nodes – e.g. nodes that do not share the same location.

¹ ANSYS is the trademark of ANSYS, Inc. in the United States.

² CFX is a trademark of Sony Corporation in Japan.

³ ANSYS WORKBENCH is a trademark of ANSYS, Inc.

⁴ ICEM CFD is a trademark used by ANSYS, Inc. under license.

Table 5.1: Mesh Statistics

Domain	Element Type	Number of Nodes	Number of Elements
Fluid (Wedge Geometry)	Tetrahedra	20486	88687
Solid (Solid Chill Geometry)	Tetrahedra	3998	17061
Solid (Water-Cooled Chill Geometry)	Tetrahedra	3667	15524

The domains are 2 mm in thickness

5.4. Material Properties

The properties required for this simulation are: density, latent heat, specific heat, and thermal conductivity. In addition, the evolution in solid fraction is needed, the liquidus and solidus temperatures (as defined by the evolution in fraction solid curve) and the latent heat which is set to a value, 4×10^5 ($\text{J} \cdot \text{kg}^{-1}$) [99].

Figure 5.3 shows the evolution of fraction solid and the fraction liquid for A319 as a function of temperature [99]. As can be seen the curves are slightly non-linear and the transition from primary to eutectic growth can be seen at the inflection point at approximately 582°C . From this diagram the liquidus temperature is taken to be 610°C and the solidus 504°C .

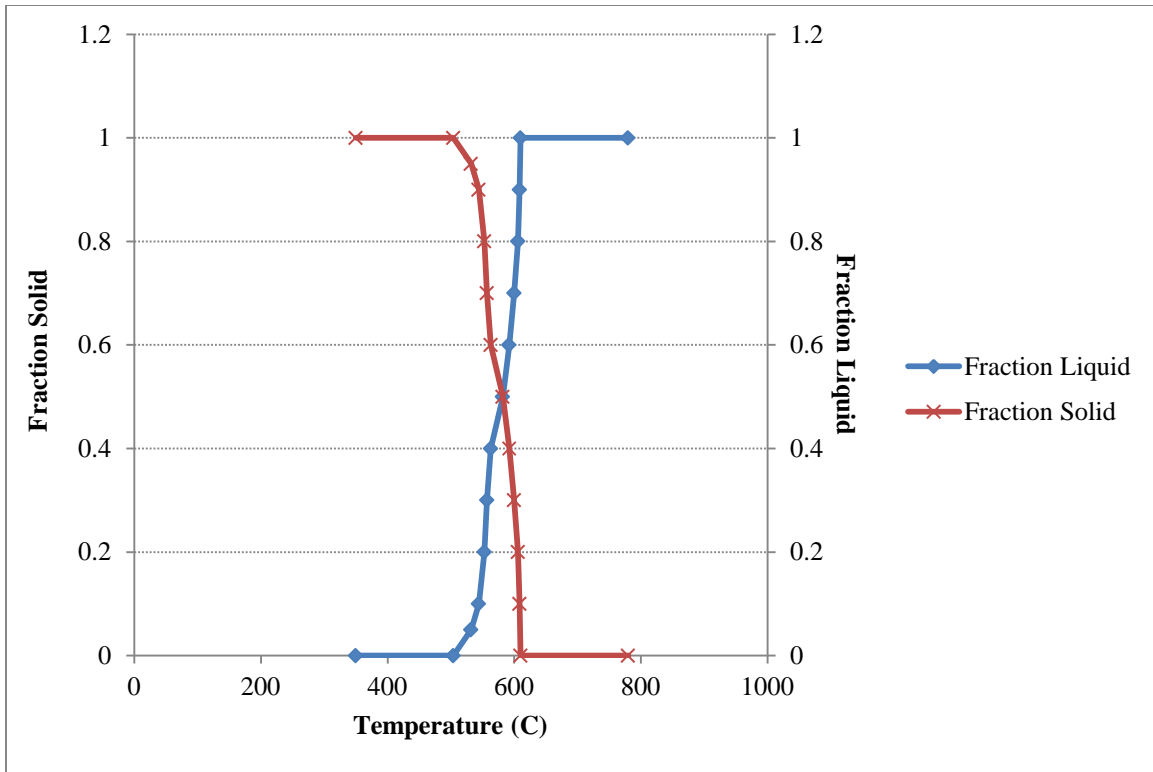


Figure 5.3: Fraction solid and fraction liquid as functions of temperature [99]

Figure 5.4 shows the variation of density versus temperature. As can be seen from this graph, no data is presented for the temperature range between the liquidus temperature and solidus temperature in the literature. For the purpose of modeling, the variation in density is assumed to be linear in this temperature range. In addition, the change in density is assumed to occur over the solidification temperature range identified in Figure 5.3. Finally, due to the constraint of constant volume mesh, the density is assumed to be constant at temperatures below the solidus temperature. The data for density input to the model is show in Figure 5.5.

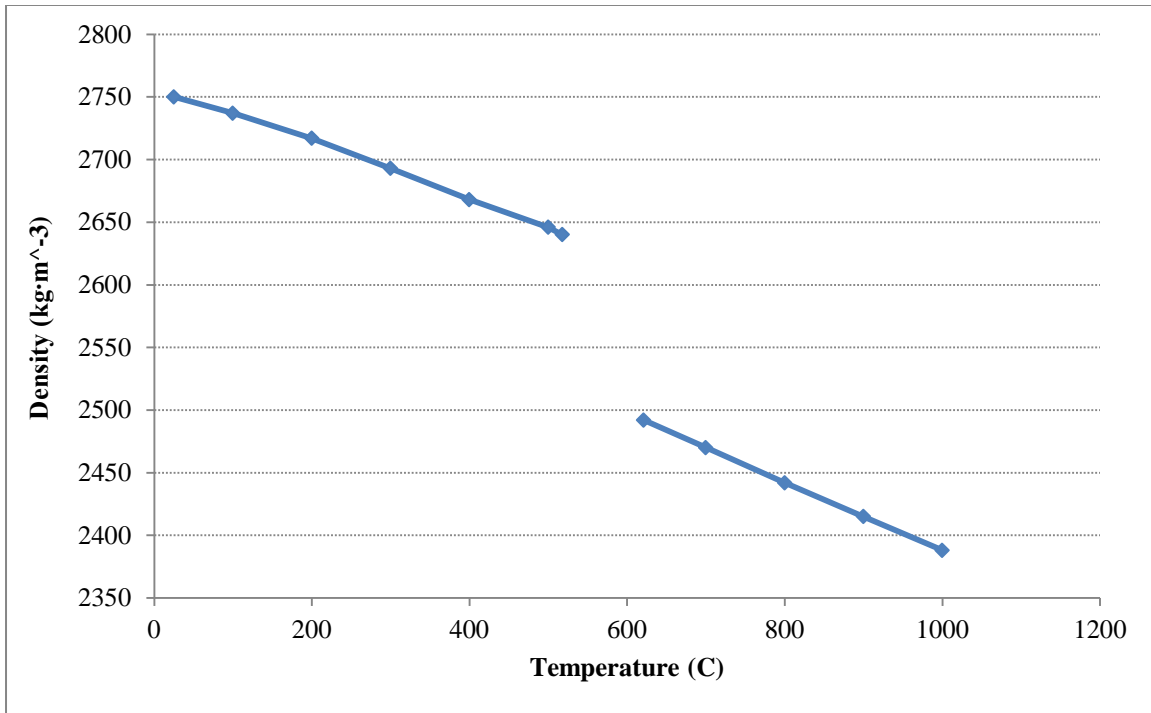


Figure 5.4: Density as a function of temperature [99]

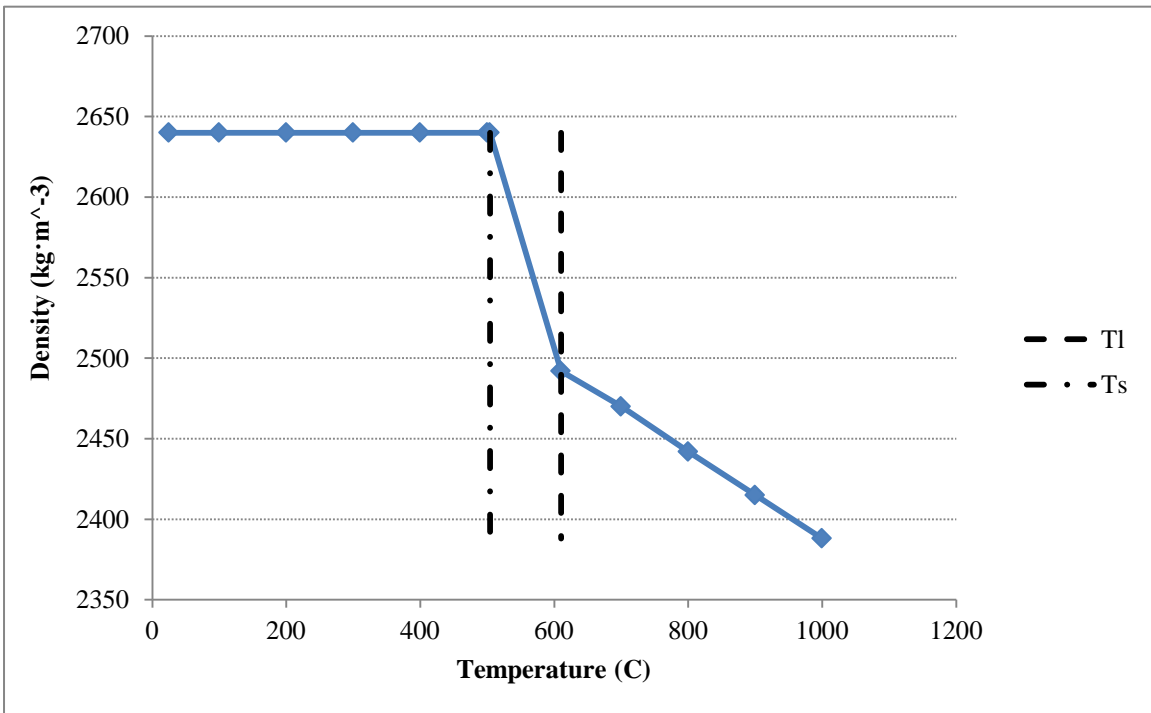


Figure 5.5: Modified density vs. temperature graph used in the modeling

Figure 5.6 shows thermal conductivity as a function of temperature [99]. As is shown in Figure 5.7, the data for the variation over the two-phase region is also not available for thermal conductivity in the reference cited. To address this, a linear variation is assumed over the phase change interval previously defined and is shown in Figure 5.7.

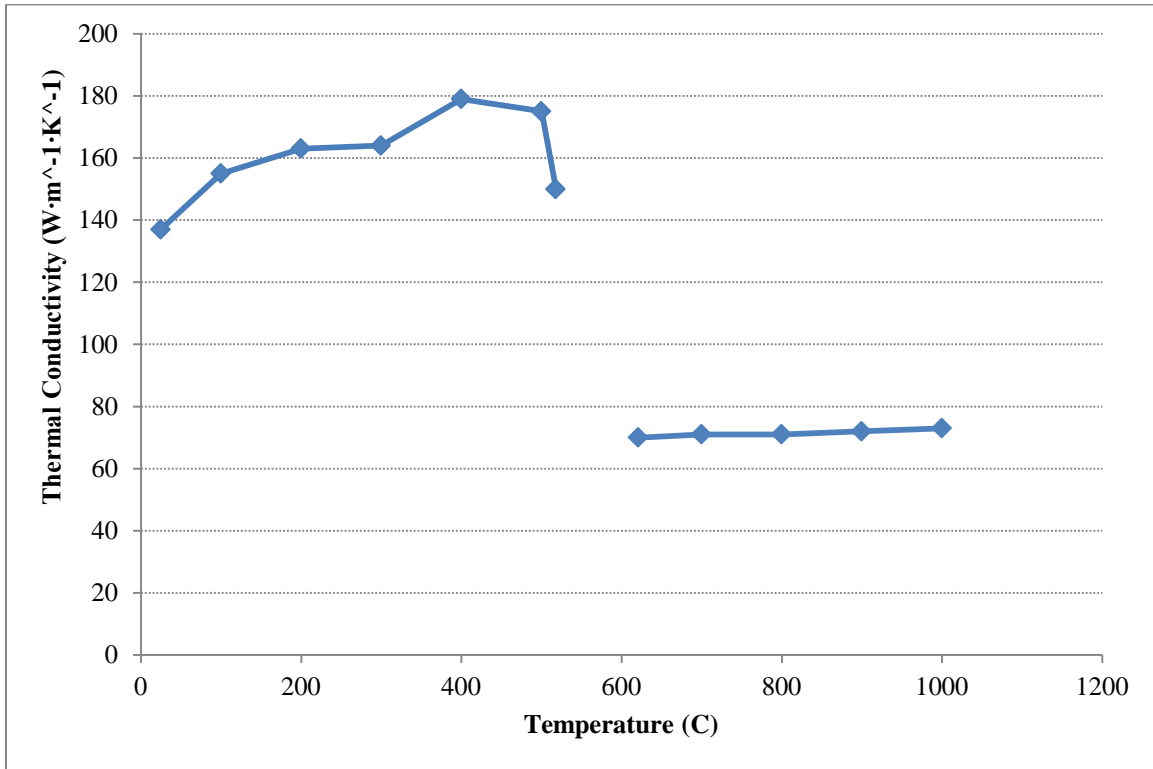


Figure 5.6: Effective thermal conductivity as a function of temperature [99]

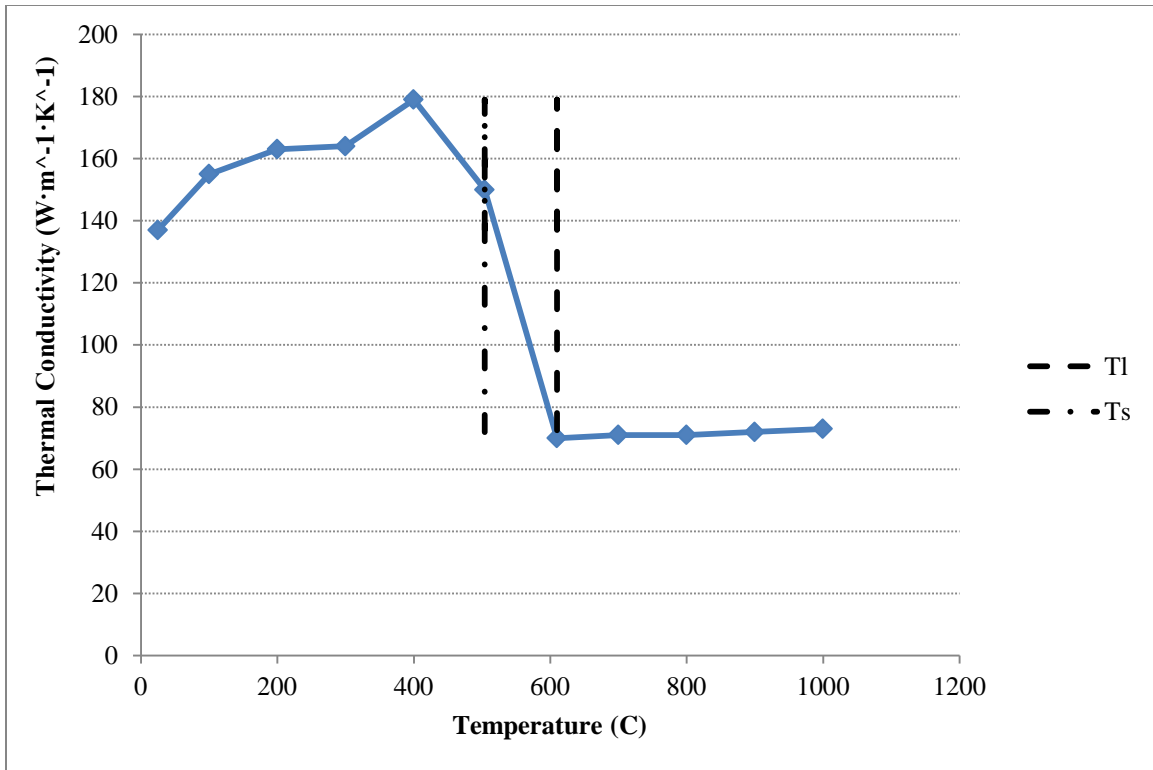


Figure 5.7: Effective thermal conductivity as a function of temperature

As was discussed in section 5.1.1, the effective specific heat capacity was used to account for the release of the latent heat during solidification as defined in Equation 5.4. Figure 5.8 shows the specific heat capacity and the effective specific heat as functions of temperature, with the later evaluated based on measured variation in fraction solid with temperature.

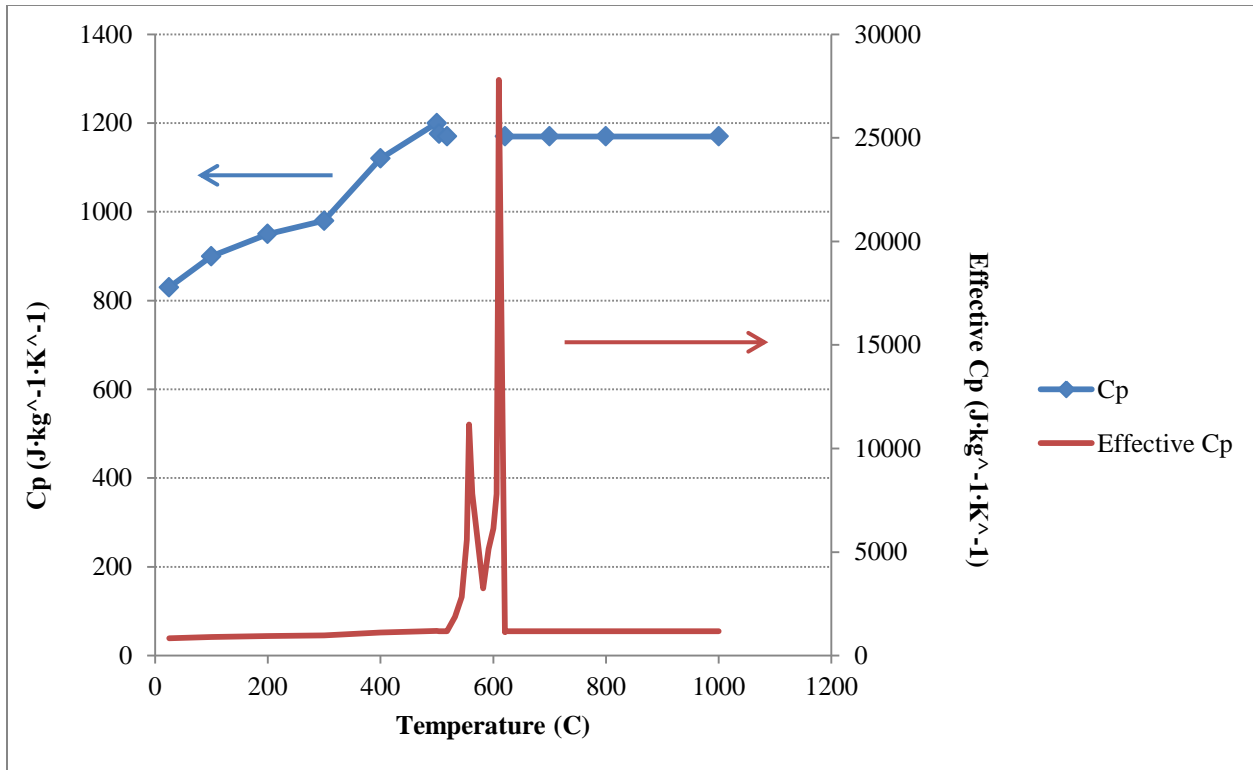


Figure 5.8: Effective specific heat as a function of temperature

As can be seen in Figure 5.7, there are two peaks in the graph: the first at approximately 610°C associated with the onset of growth of the primary phase; and the second, at approximately 557°C associated with growth of the primary eutectic phase. Both peaks represent problems numerically from a convergence/accuracy standpoint and would require a very fine mesh, small time-step for integration in time and large number of iterations per time step in order that they are resolvable. To avoid this problem, the evolution of fraction solid and therefore latent heat was assumed to be linear over the phase change temperature range. The resulting curve for the effective specific heat is shown in Figure 5.9.

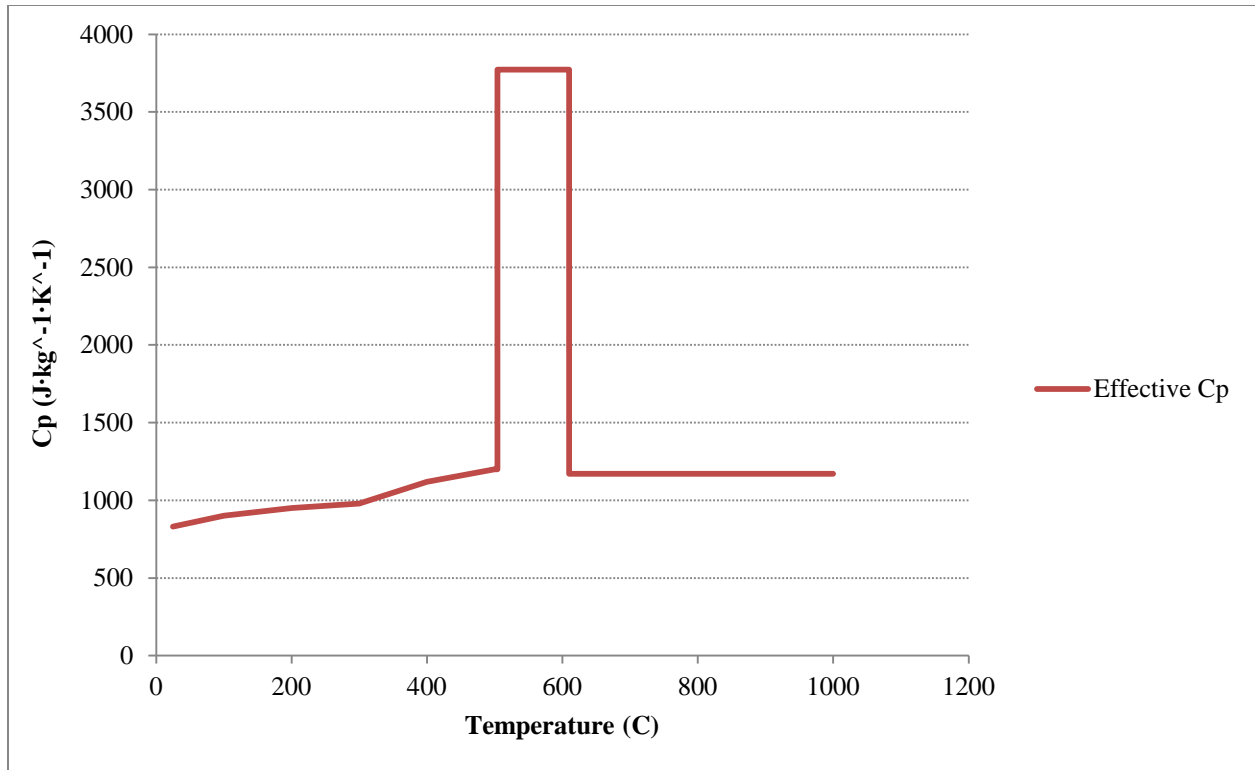


Figure 5.9: Effective specific heat as a function of temperature used for modeling

5.5. Initial Conditions

The initial conditions applied to each casting are shown in Table 5.2.

Table 5.2: Initial conditions of the castings

	Casting 1	Casting 2	Casting 3	Casting 4	Casting 5	Casting 6
Melt Initial Temperature (°C)	720	680	680	680	680	680
Chill Initial temperature (°C)	175	160	115	20	20	115

According to the experimental results, the melt temperature drops approximately 60 °C during the pouring process. Since the modeling does not include pouring process, the initial temperature of the melt was set to 60 °C less than the pouring temperature.

5.6. Boundary Conditions

Figures 5.10 and 5.11 schematically illustrate all of the sections where boundary conditions were defined for the two casting/chill geometries, and Figure 5.12 shows a close-up view of the chill/casting interface boundary.

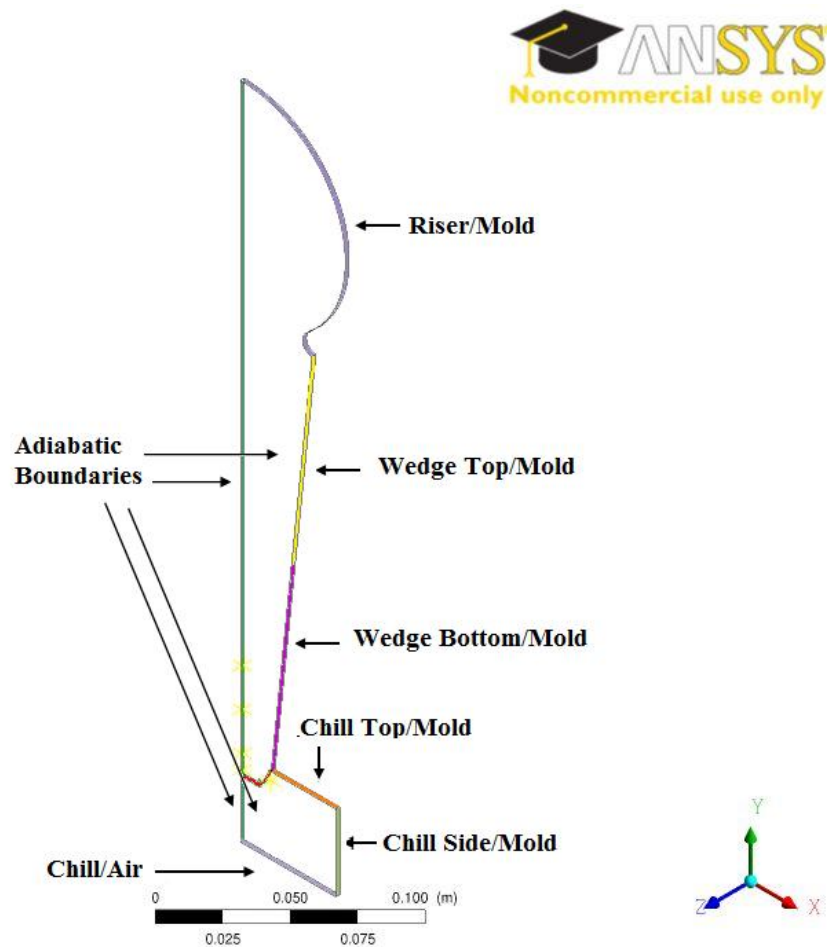


Figure 5.10: The schematic of the boundaries defined for the solid chill conditions

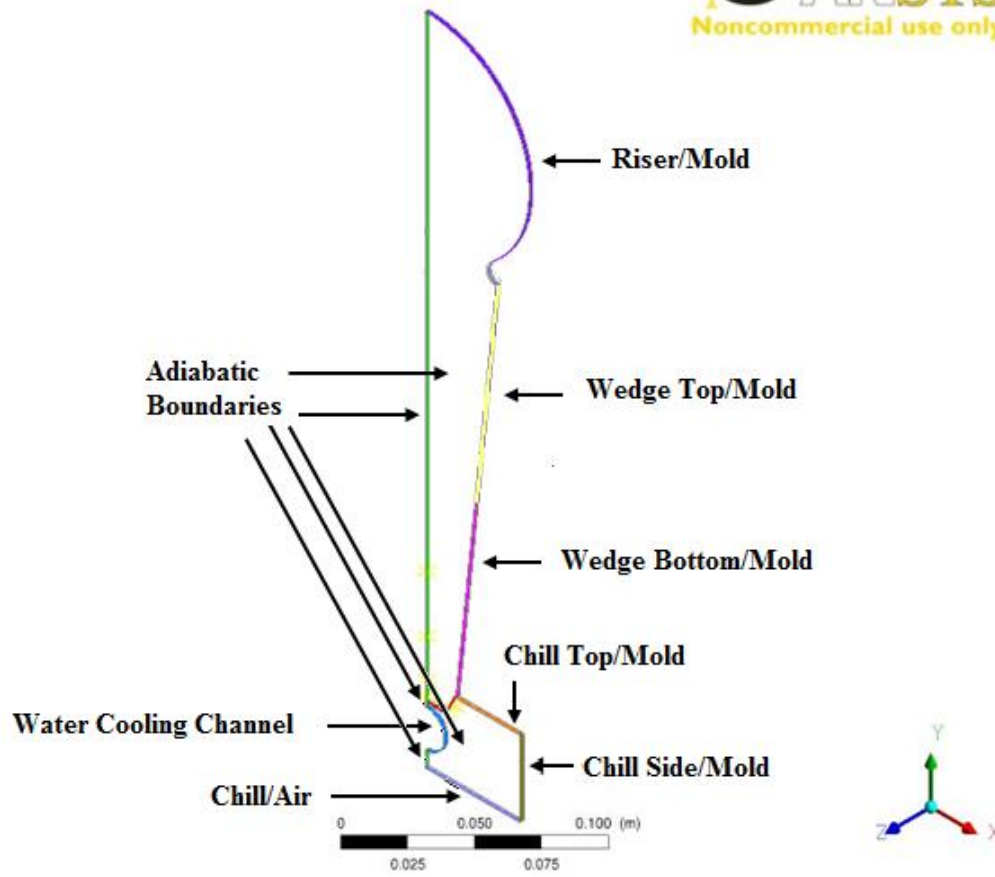


Figure 5.11: The schematic of the boundaries defined for the water cooled chill conditions

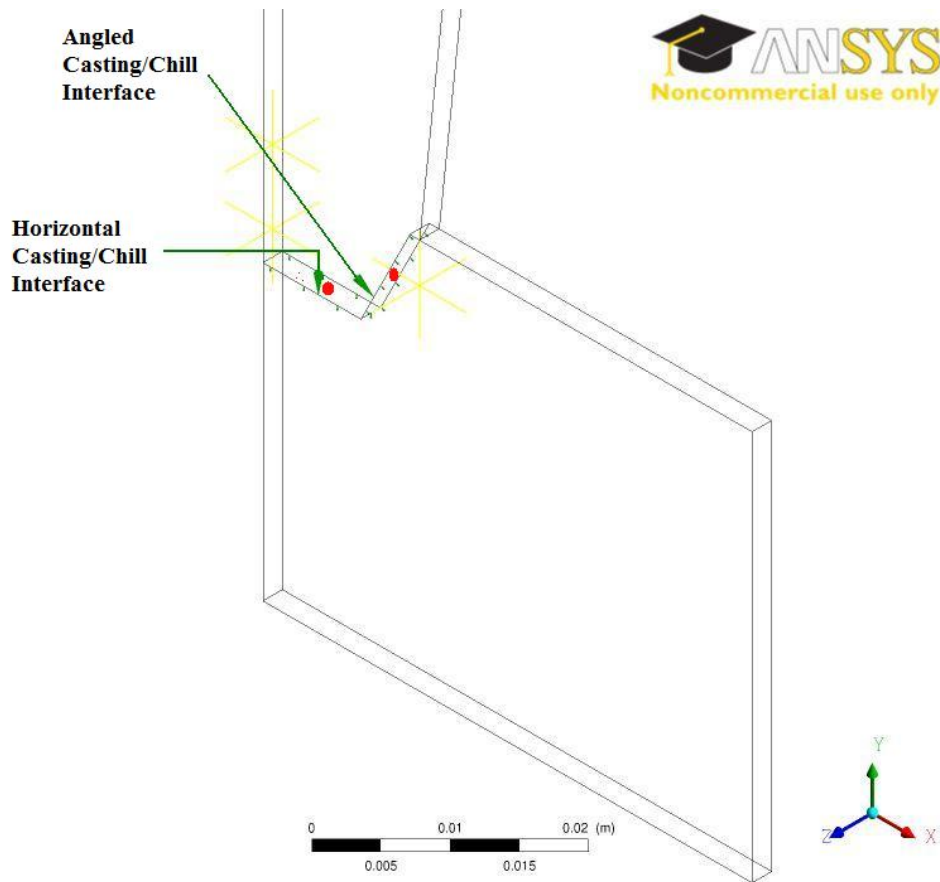


Figure 5.12: The schematic of the chill/casting interface for both the solid chill, and water cooled chill conditions

5.6.1. Chill/Casting Interface Boundary Conditions

The general form for the boundary condition used most widely to describe the interface between the casting and various mold components in casting processes, including chills, is given in Equation 5.5:

$$q = h_{Interface} (T_{S_i} - T_{S_j}) \quad (5.5)$$

Applied in this work, q is the heat flux ($\text{W}\cdot\text{m}^{-2}$) at the point on the surface of either the casting or chill face where the flux is being applied, $h_{interface}$ is the interfacial heat transfer coefficient

(IHTC) between the chill and the casting ($\text{W}\cdot\text{m}^{-2}\cdot\text{K}^{-1}$), T_{S_i} is the temperature (K) at the point on the surface for which the heat flux is being applied and T_{S_j} is the temperature on the opposite side of the interface, adjacent to the point being processed. The IHTC may be a function of temperature, time or the interface displacement (degree to which the interface forms a gap).

In the present study, the analysis of the experimental results with the model, presented in Chapter 6 revealed that a temperature dependent correlation for the IHTC was needed for the experiments with the solid chill and a time dependent correlation was needed for the experiments with the water-cooled chill. Unfortunately, in ANSYS CFX, the temperature dependent function for the IHTC, $h_{interface}(T)$, is based on an area average temperature for the surface being processed - i.e. $T = T_{avg, S_i}$. It was felt that this limitation could be a source of significant error in the present study, due to the large temperature gradient formed in the casting normal to the chill – i.e. referring to Figure 5.12, the average temperature along the horizontal face could be significantly different than the average temperature along the angled face. Because of this, the casting/chill interface was broken into two boundaries: a horizontal segment and an angled segment. Both boundaries adopt Equation 5.5 and the same IHTC correlation, which is presented in Chapter 6. When processing the casting boundary heat flux, depending on the face being processed, T_{S_i} and T_{S_j} are either the horizontal boundaries of the casting and chill, respectively, or the angled boundaries of the casting and chill, respectively, or visa-versa when processing the chill boundary heat flux.

The same two boundaries are used in the water-cooled chill model for the sake of convenience even though a single boundary would suffice as a time dependent IHTC is applied.

5.6.2. Casting/Mold Boundary Conditions

Normally, the interface between the casting and the mold would be treated in a similar fashion to casting/chill interface. In the present work, for the reasons previously described, the mold was not included in the analysis domain. To address the issue of temperature averaging described above the surface of the casting/mold was subdivided into three sections of equal length. The following boundary condition was applied to the Riser/Mold, Wedge Top/Mold, and Wedge Bottom/Mold surfaces, and is defined as:

$$q = h_{Casting / Mold} (T_{avg, S_i - Casting}) (T_{S_i - Casting} - T_{Mold}) \quad (5.6)$$

where $h_{Casting / Mold} (T_{avg, S_i - Casting})$ is the temperature dependent heat transfer coefficient (HTC) ($W \cdot m^{-2} \cdot K^{-1}$) at the surface of the casting, and is defined as a function of the average face temperature of the surface being processed – e.g i is either the Riser, Wedge Top, or Wedge Bottom at the point being processed and T_{Mold} is a specified function of time.

5.6.3. Chill/Mold Boundary Conditions

The governing equation for heat transfer at Chill Top/Mold and Chill Side/Mold boundaries is:

$$q = h_{Chill / Mold} (T_{avg, S_i - Chill}) (T_{S_i} - T_{Mold}) \quad (5.7)$$

where $h_{Chill / Mold} (T_{avg, S_i - Chill})$ is the temperature dependent heat transfer coefficient ($W \cdot m^{-2} \cdot K^{-1}$) and is defined as a function of the average face temperature of the surface being processed – e.g i

is either the chill top or chill side, $T_{S_i-Chill}$ is the surface temperature of the chill at the point being processed. T_{Mold} is the mold temperature and is defined as a function of time.

5.6.4. Chill/Air Boundary Conditions

In the experiments, there was an air gap between the sand mold and the bottom of the chill. The governing equation for the “Chill Bottom” boundary condition in all cases is:

$$q = h_{Chill / Air} (T_{avg, ChillBottom}) (T_{S_i-ChillBottom} - T_{Air}) \quad (5.8)$$

where $h_{Chill/Air}$ is a constant value of 5 ($W \cdot m^{-2} \cdot K^{-1}$), and the $T_{S_i-ChillBottom}$ is the surface temperature of the chill at the point being processed on the chill bottom – e.g. i is the bottom face of the chill, and T_{Air} is air temperature and defined as a function of time.

5.6.5. Adiabatic Surfaces

As is shown in Figures 5.10 and 5.11, the symmetry surfaces named are all assumed to be adiabatic surfaces, where:

$$q = 0 \quad (5.9)$$

5.6.6. Water Cooling Channel Boundary Conditions

The calculation of the heat transfer coefficient for the water cooling channel begins with the calculation of Reynolds number. For this calculation, the velocity of the water, $V(m \cdot s^{-1})$, was calculated as:

$$V = \frac{Q}{A} = \frac{0.05}{60 \cdot \pi \cdot (0.01)^2} = 2.7(m \cdot s^{-1}) \quad (5.10)$$

where Q is the flow rate ($m^3 \cdot s^{-1}$) of water, measured by means of the flow-meter in the experimental process, and A is the area (m^2) of the normal cross section of the cooling channel.

$$Re = \frac{\rho V D}{\mu} = \frac{1000 \cdot 2.7 \cdot 0.02}{0.001} = 5.3 \cdot 10^4 \quad (5.11)$$

where ρ is the density ($kg \cdot m^{-3}$) of water at $10^\circ C$, D is the diameter (m) of the cooling channel, and μ is the viscosity ($Pa \cdot s$) of water at $10^\circ C$. The laminar to turbulent transition in a pipe occurs when the Re exceeds 4000. Since the value obtained from Equation 5.11 is more than this limit, the water flow in the pipe is considered to be turbulent flow. Hence, the Nusselt number was calculated as:

$$Nu = 0.023 \cdot Re^{0.8} \cdot Pr^n \approx 3.4 \cdot 10^2 \quad (5.12)$$

where Pr is the Prandtl number:

$$Pr = \frac{\nu}{\alpha} = \frac{\text{Momentum diffusivity}(m^2 \cdot s)}{\text{Thermal diffusivity}(m^2 \cdot s)} = 9.47 \text{ for water at } 10^\circ C \quad (5.13)$$

and n is 0.4 when the walls are hotter than the bulk fluid and 0.33 when the walls are colder.

The heat transfer coefficient, h ($W \cdot m^{-2} \cdot K^{-1}$), was obtained from:

$$h = \frac{k_w}{D} \cdot Nu = \frac{0.51}{0.02} \cdot 3.4 \cdot 10^2 \approx 8.7 \cdot 10^3 \quad (5.14)$$

where k_w is the thermal conductivity ($\text{W}\cdot\text{m}^{-1}\cdot\text{K}^{-1}$) of water at 10°C .

5.7. Model Control Parameters

The execution times, range from 500 to 2000 s, with time step of 0.1 s, and an output frequency of 1 second. The maximum iteration for each time step was set to 5, and the maximum residual, which relates to the degree to which the solution has converged, was set to less than 10^{-4} . A Second Order Backward Euler Scheme was adopted for the integration in time. Typical simulation times ranges between 67 and 307 minutes.

6. Results and Discussion

In this section, the model predictions are compared to the experimental thermocouple results in order to validate the thermal models, and also to understand the behavior of the chill/casting interface, from a heat transport standpoint. The chill/casting behavior is different for the cases of the solid chill and the water-cooled chill. To fit the model predictions to the thermocouple measurements it was necessary to adjust four different parameters:

- Chill/casting interfacial heat transfer coefficient
- Casting/mold heat transfer coefficient
- Chill/mold heat transfer coefficient, and
- Mold-sink temperature evolution with time.

All these parameters were adjusted with a trial and error method.

As previously described in Chapter 5, the mold was not included in the computational analysis and was treated mathematically as a time variant heat sink.

Most of the effort to align the model results with the thermocouple responses was spent on adjusting the chill/casting interfacial heat transfer coefficient due to the fact that the dominant heat transfer process takes place through the chill/casting interface. The model has shown to be most sensitive to this parameter, as will be discussed in more detail in Chapter 7, Sensitivity Analysis.

The thermal model predictions and the experimental results have been compared from the beginning of the casting process up to the end of solidification at the location of the thermocouple farthest from the chill - i.e. the 50 mm thermocouple. The chill/casting interface was found to behave differently, for the case of the solid chill and the water-cooled chill in terms of the evolution of the interface thermal resistance.

6.1. Thermal Model Validation

The thermal model predictions and the experimental results from all thermocouples embedded in the casting and the chill have been compared. In each case, the solid lines represent the experimental results, and the dotted lines show the modeling results. In addition, on each figure, lines have been added to delineate the equilibrium liquidus and solidus temperatures for A319. The dashed lines show the solidus temperature and the dot/dash lines show the liquidus temperature. Figures 6.1 – 6.4 show the comparison for the solid chill castings, and Figures 6.5 – 6.6 compare the results for the water-cooled chill experiments.

As can be seen from a quick look at Figures 6.1 – 6.6, a general satisfactory agreement between the thermal model predictions and the experimental data has been obtained. For the casting thermocouples the variation of temperature with distance from the chill, and the evolution in cooling rate with time, have been relatively well reproduced. The model was also able to reproduce relatively accurately the experimental data measured in both the solid chill and the water-cooled chill.

One general exception to the overall good agreement occurs at the 30 mm position. Firstly, the 30 mm thermocouple data shows consistently higher temperatures compared to the model

predictions in all of the castings. This trend is also observed in casting 4, at the 10mm location. For the solid chill experiments this deviation persists until approximately 50% solid has formed or 550°C. For the water-cooled experiments the deviation persists until below the solidus. At longer times the agreement between the measurements and the model predictions at 30mm (and at 10mm in casting 4) is good with the trend being to better agreement with increasing time. Secondly, particularly at temperatures above the liquidus, the data is noisy. Moreover, once solidification starts the noise rapidly dissipates.

One possible explanation for this behavior is that the temperature at 30mm is being influenced by fluid flow— i.e. bulk transport of heat, which is inconsistent with the assumption made earlier that fluid flow, can be ignored. This would be consistent with the 30 and 50mm locations reading the same temperature and with the noise in the data present above the liquidus. The difference in behavior observed between the solid and water-cooled chill experiments with respect to this is more difficult to explain, but may be due to the higher sustained cooling rates with the water-cooled experiments resulting in a larger buoyancy driven flow, which in turn could affect heat transport to lower temperatures.

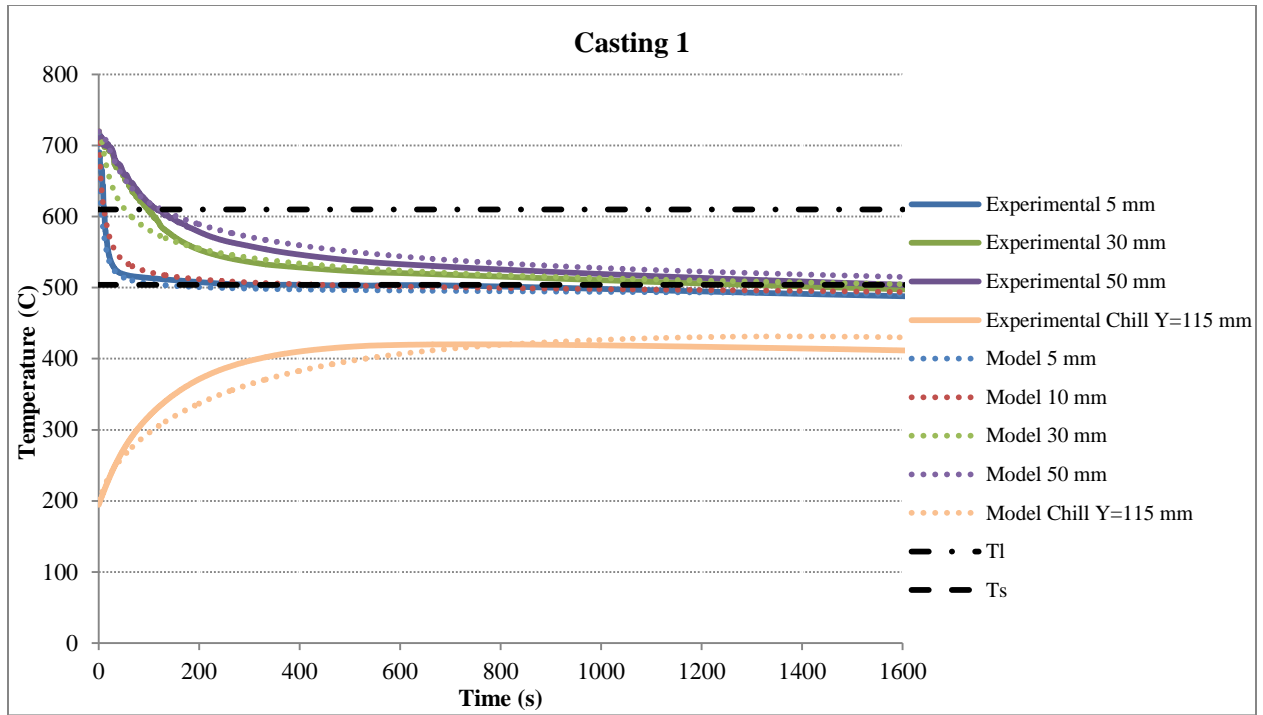


Figure 6.1: Comparison between the experimental data and model predictions

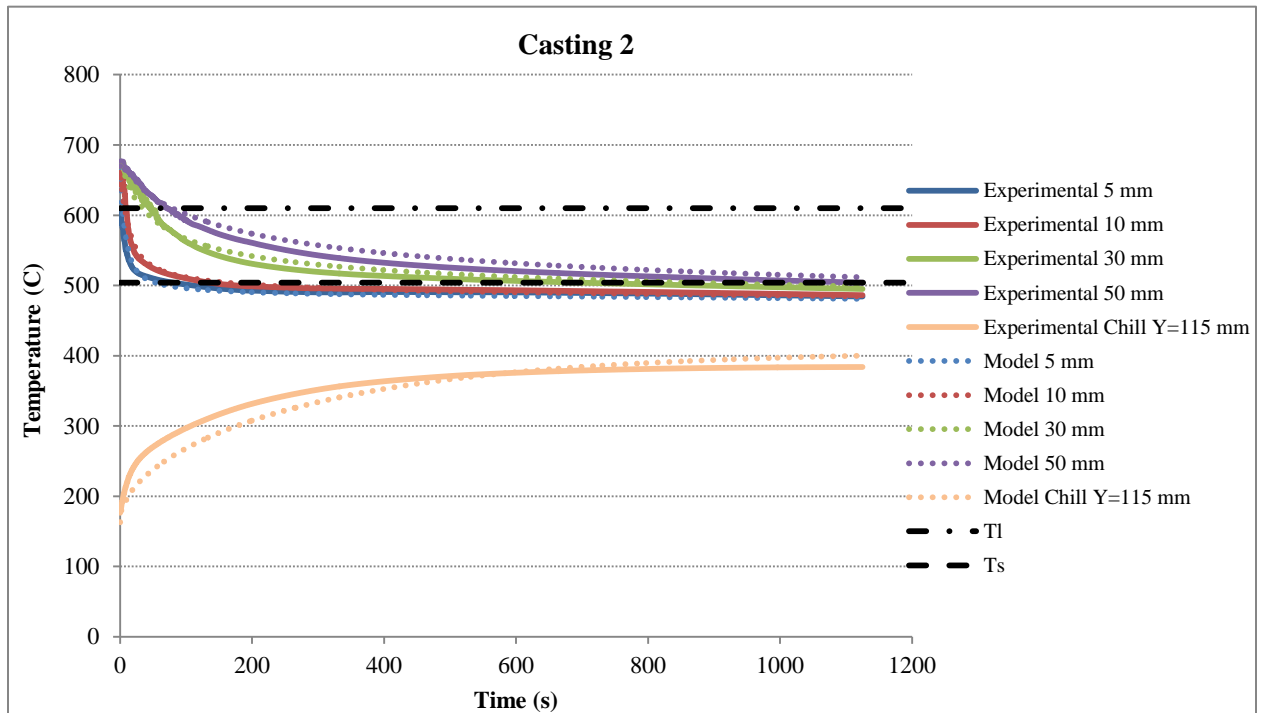


Figure 6.2: Comparison between the experimental data and model predictions

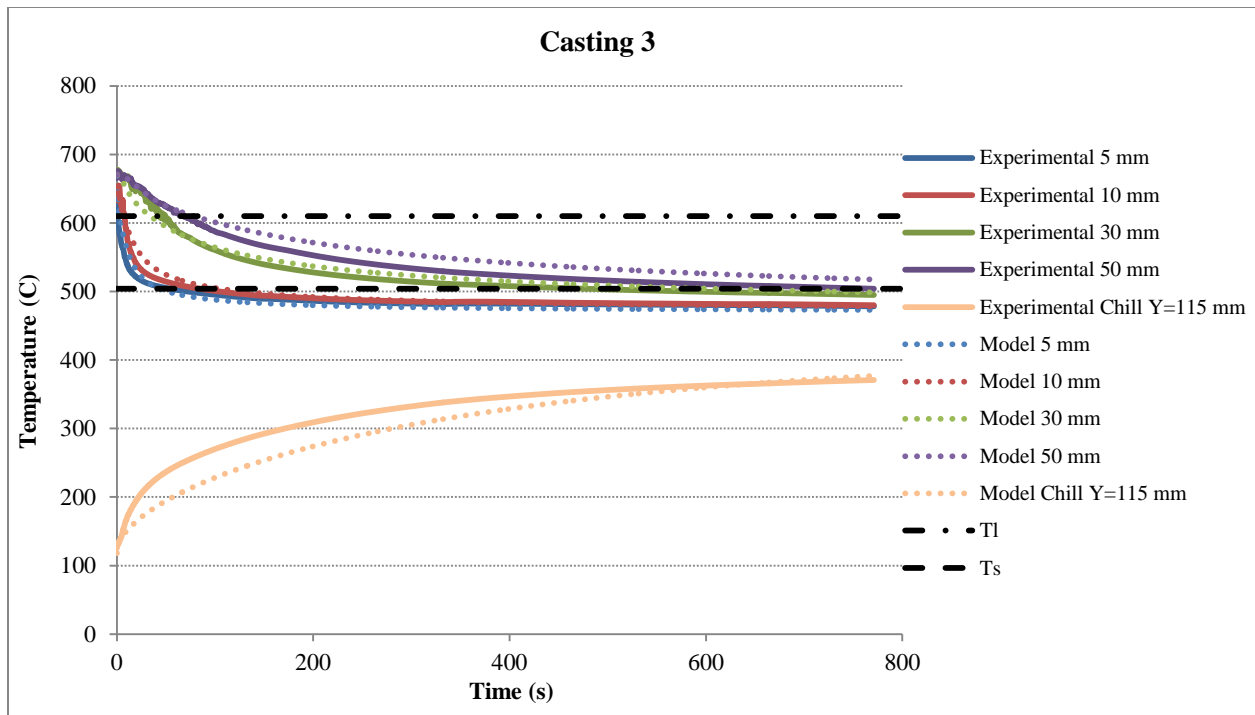


Figure 6.3: Comparison between the experimental data and model predictions

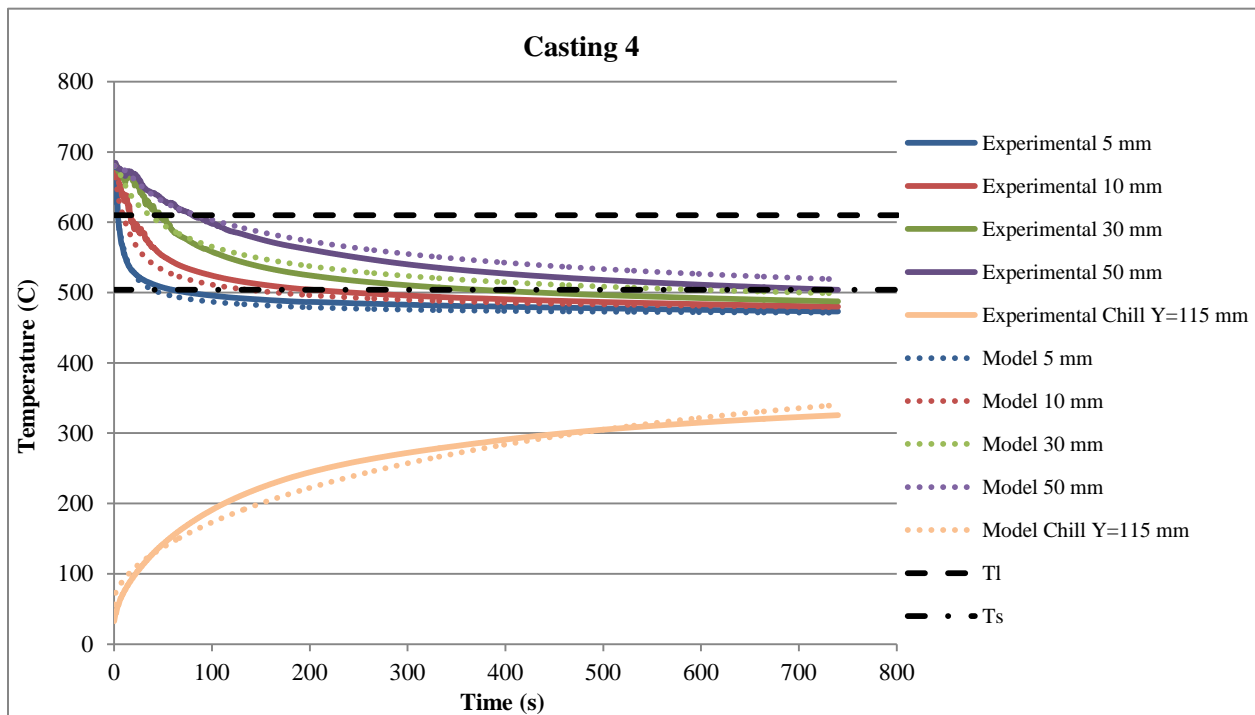


Figure 6.4: Comparison between the experimental data and model predictions

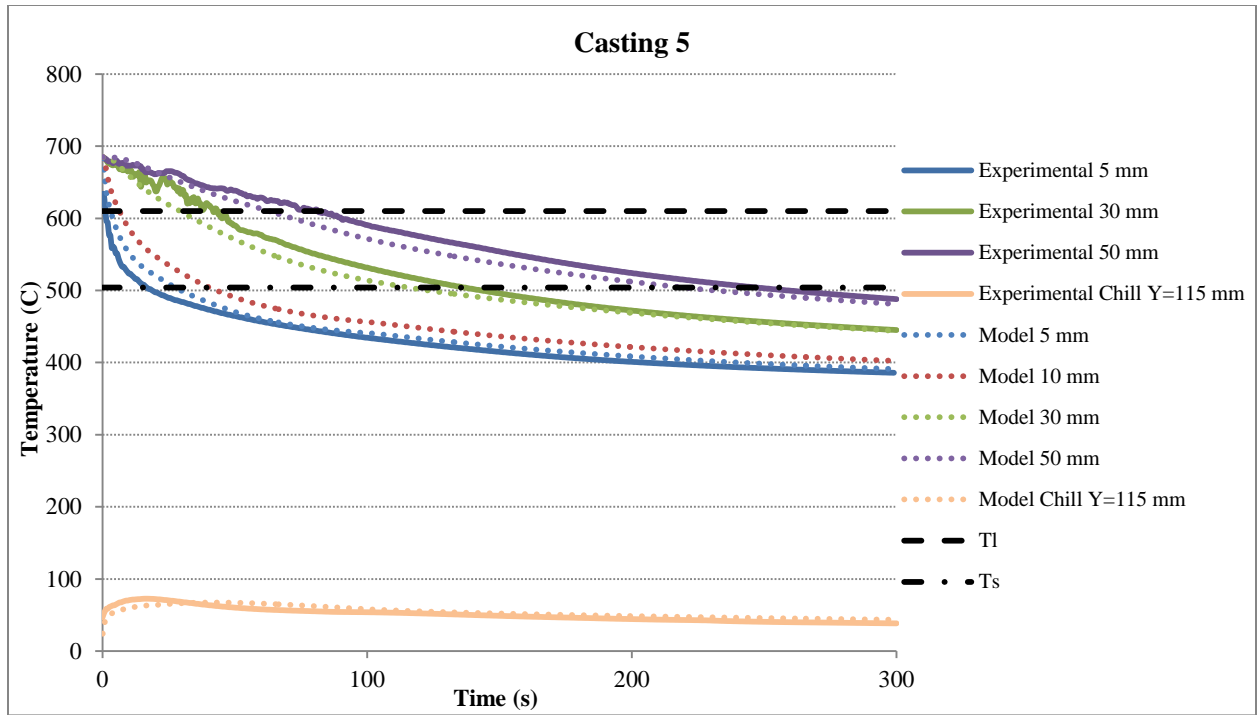


Figure 6.5: Comparison between the experimental data and model predictions

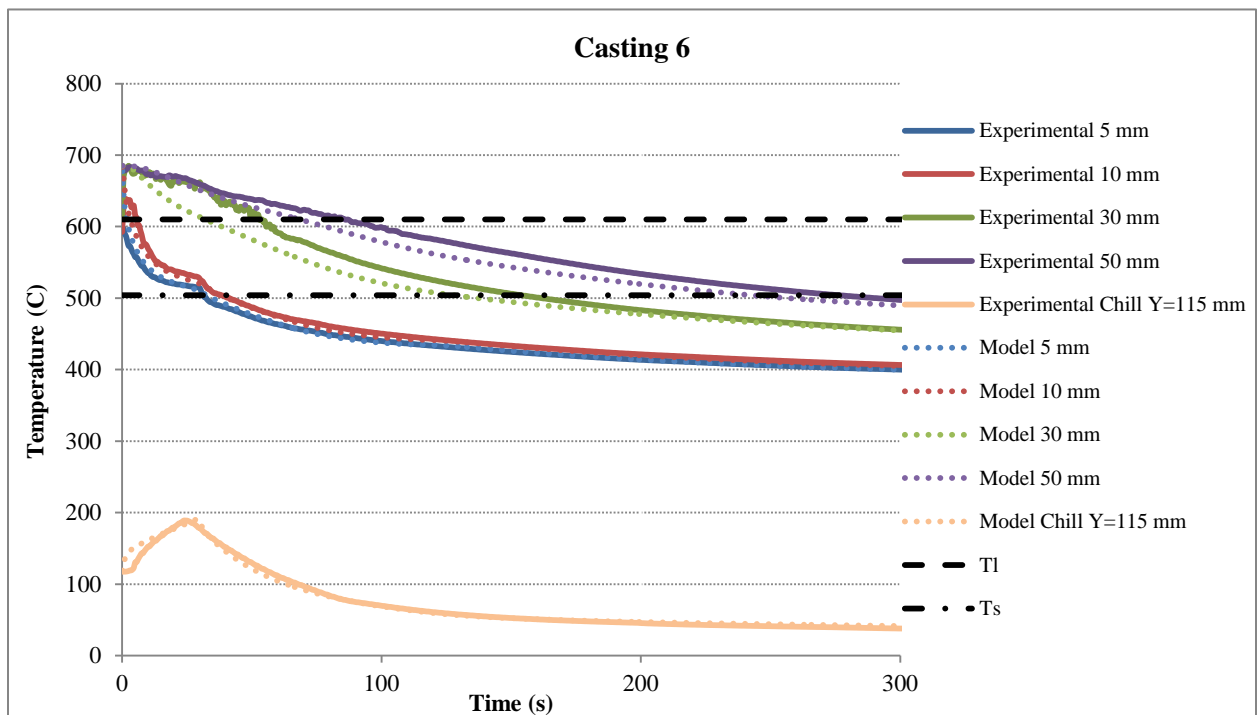


Figure 6.6: Comparison between the experimental data and model predictions

6.2. Fitting Parameters

6.2.1. Chill/Casting Interfacial Heat Transfer Coefficient

In the early stages of casting solidification at locations in proximity to the chill, transport of heat takes place mainly through the chill/casting interface. This is due to the fact that the sand mold has a low thermal conductivity and acts to a certain degree as an insulating material, whereas the copper is a strong heat conductor.

As previously alluded to, the behavior of this interface in the solid chill castings is different from the water-cooled chill conditions. As discussed previously in Chapter 2, there are three commonly used approaches to define the IHTC. It may be defined as a function of temperature, time or the interface displacement (degree to which the interface forms a gap). The third approach can only be applied in cases where a stress analysis is undertaken and the relative displacements of the appropriate components are calculated. In this research, which undertakes only a thermal analysis, a temperature dependent IHTC was found to be adequate to describe the evolution of the heat transfer for the cases in which a solid chill was used, and a time dependent IHTC was needed to describe the interface behavior and the heat transport in cases where the water-cooled chill was used.

Solid Chill Interfacial Heat Transfer Coefficient – Figure 6.7 compares the temperature dependent interfacial heat transfer coefficients needed to fit the model to the thermocouple data for the four solid chill experiments. The temperature on the x-axis of the plot represents the surface temperature of the casting at the interface, which is predicted by the model. Qualitatively, all the curves show the same behavior. They all start at a high value and remain

constant from the highest temperature plotted to T_L . They then all drop slightly from T_L to T_S , due to solidification occurring at the interface; and finally they all drop significantly from T_S to the interface temperature at which the modeling ends, as solidification proceeds into the casting. Also, there is a strong dependency of the IHTC on the amount of melt super heat; showing a trend to higher initial values with elevated pouring temperatures.

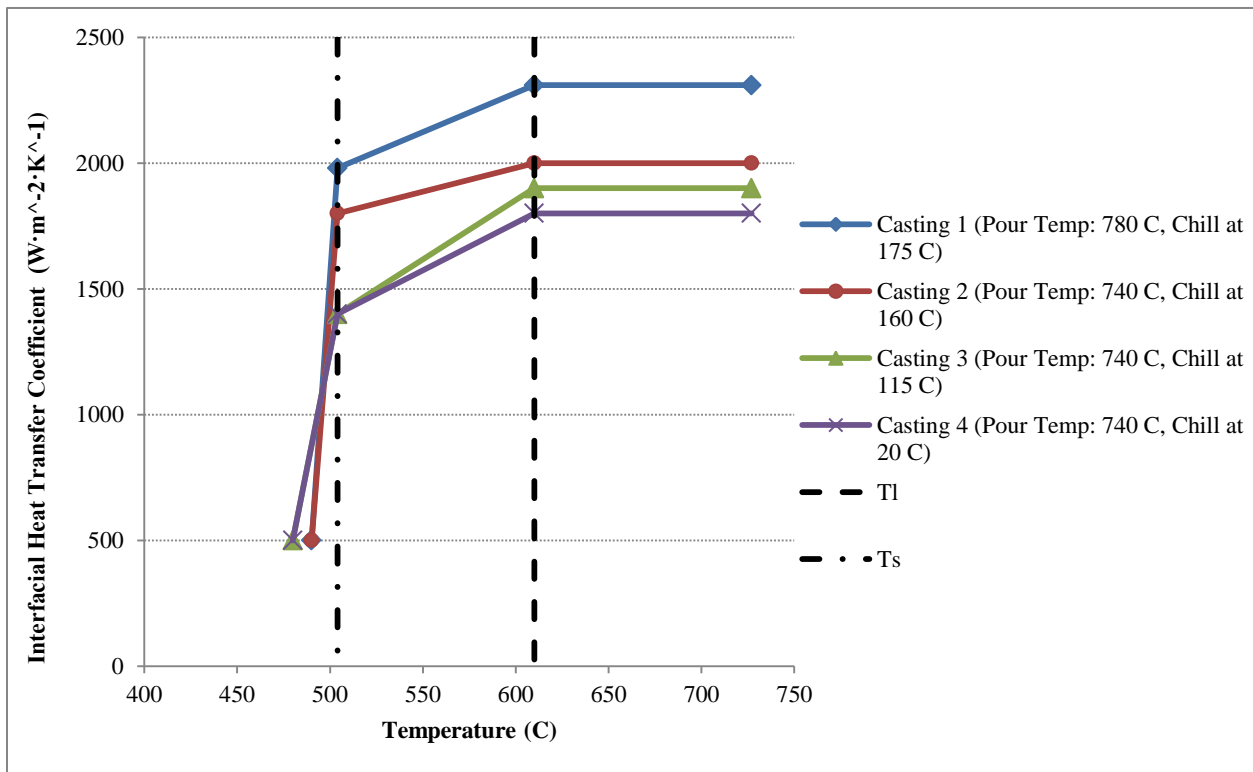


Figure 6.7: Temperature dependent melt-chill interfacial heat transfer coefficient for solid chill conditions

In order to better understand the mechanism of gap formation in the case of solid chills, the variations of interface temperatures in the casting and chill domains have been plotted as a function of time for casting 4 together with the variation in the IHTC input to the model. The results are shown in Figure 6.8 (a) and (b). Figure 6.8 (a) presents expanded view at short times and (b) the behavior over the entire time of the analysis. In reality, plotting the input IHTC

would be misleading, since CFX employs it as a function of the area average of temperature at a specific surface; hence, the trend will not be linear. To aid in the discussion a schematic diagram highlighting what are believed to be the three stages of interface behavior that are consistent with the model IHTC variation has also been drawn and is shown in Figure 6.9.

Stage 1 – Referring to Figure 6.8 (a), the IHTC is at its highest value from the beginning of the casting process until approximately 3 seconds elapsed time, when the casting temperature at the interface reaches to T_L . Figure 6.9 (a) illustrates a good contact between the casting and the chill during this stage, when the liquid metal is first poured into the mold cavity. The molten metal fills at least a portion of the asperities present on the chill surface due to its high fluidity, and hence; the IHTC remains at its highest value during Stage 1. Complete contact with the chill can not be obtained due to the melt surface tension effects. Higher super heats and higher chill initial temperatures result in better conformability with asperities and higher heat transfer, which is also consistent with the data shown in Figure 6.7.

Stage 2 – At the liquidus temperature - i.e. approximately 3 seconds elapsed time shown in Figure 6.8 (a) - the phase change from liquid to solid starts at the interface. During this stage, the contact between the casting and the chill begins to degrade and conformation to some of the chill asperities is lost as can be seen in Figure 6.9 (b). Referring to Figure 6.8 (a) and (b), it can be seen that the IHTC decreases rapidly from approximately 3 seconds to about 51 seconds when it reaches to solidus temperature.

Stage 3 – In Stage 3 shown in Figure 6.8 (b) after the casting at the interface reaches T_S , the rate of temperature change at the interface in the casting decreases significantly. However, the IHTC

continues to decrease at a significant rate albeit at a slower rate than during Stage 2. This regime of behavior is reflected in Figure 6.7 by the rapid drop in IHTC with temperature that occurs after T_S . It would appear that this represents the period of gap formation, as is shown in Figure 6.9 (c), when the rate of contraction of the casting exceeds the rate of chill expansion.

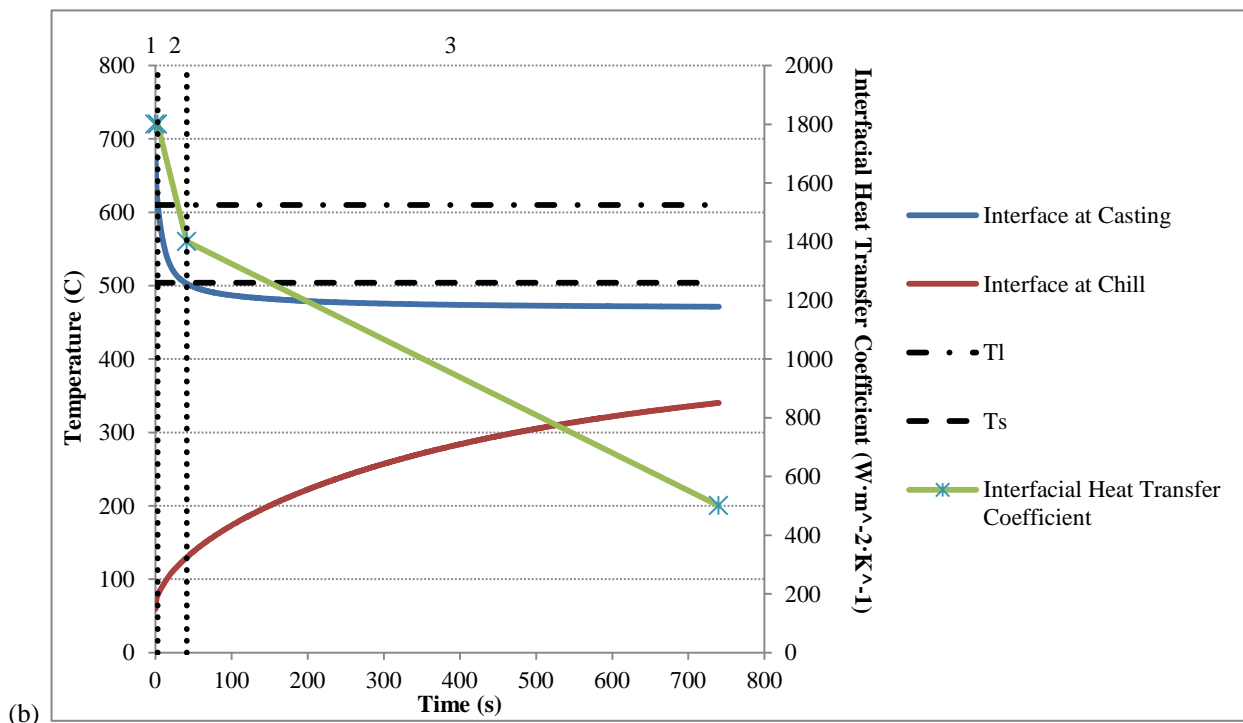
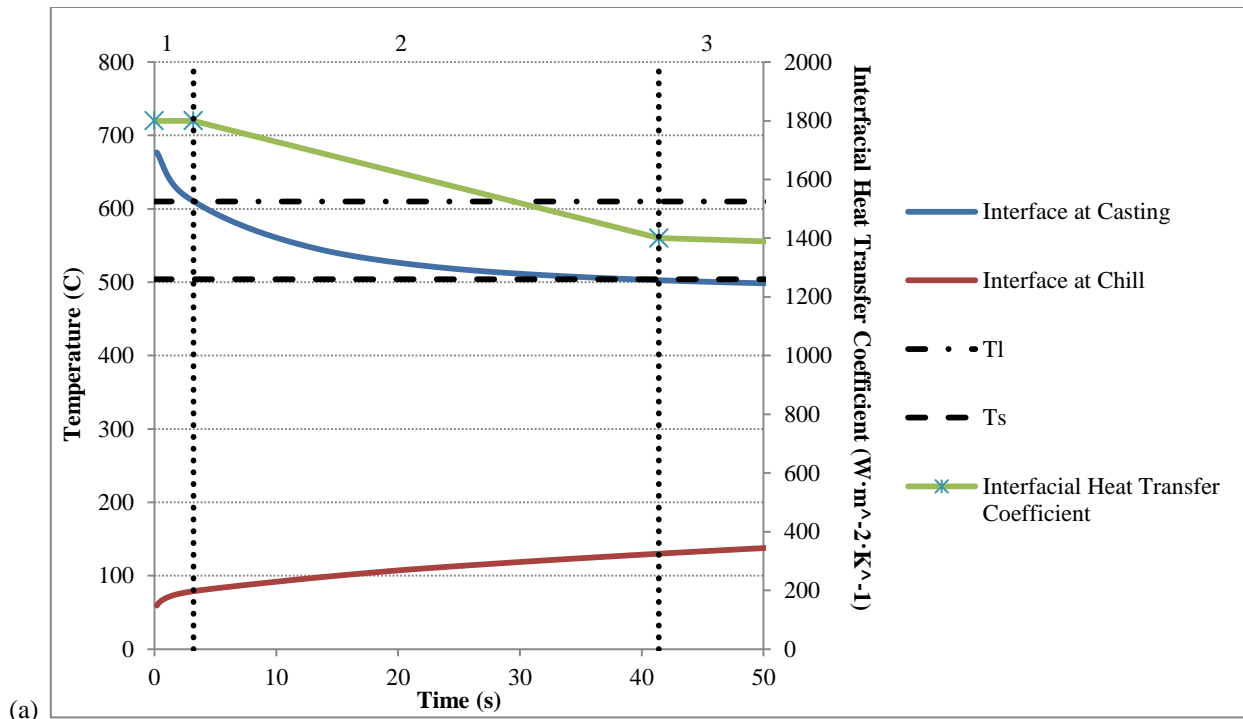


Figure 6.8: The temperature variation of the interface at casting and chill domains, and the related IHTC; (a) for the first 50 seconds, (b) for 740 seconds, casting 4

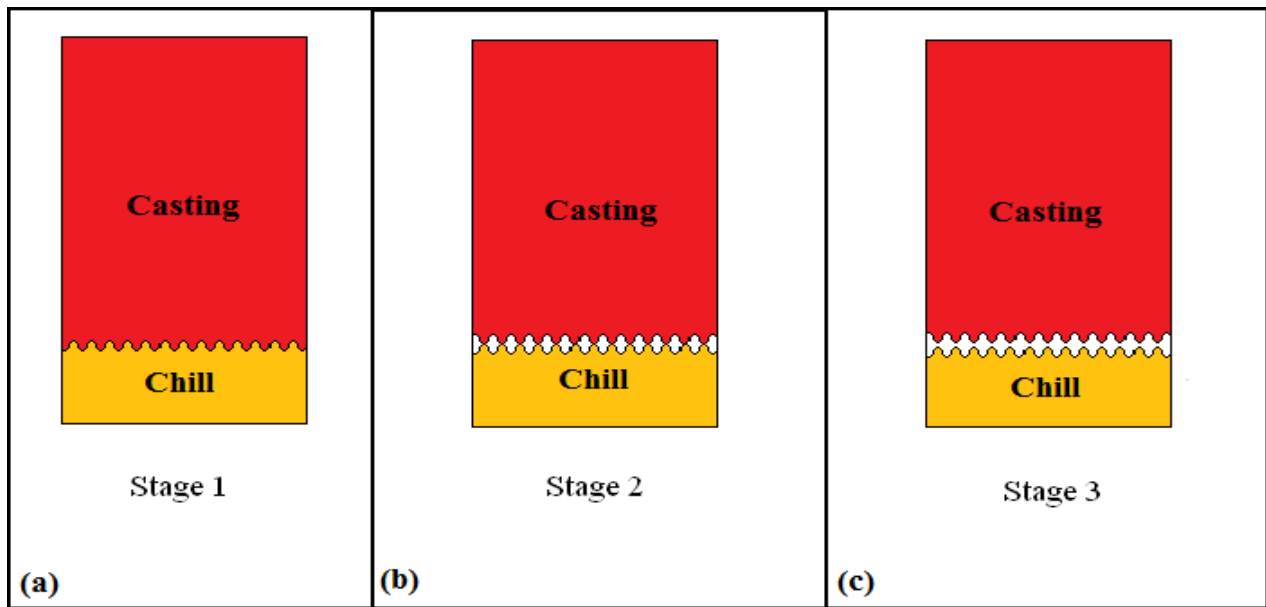


Figure 6.9: The schematic of the Casting/Chill interface behavior in solid chill conditions

Water-Cooled Chill/Casting Interfacial Heat Transfer Coefficient – Figure 6.10 shows the time dependent interfacial heat transfer coefficient applied to the two water-cooled chill models. Qualitatively, both the castings show the same behavior. They both start at a high value and remain constant from the beginning of the casting to the time at which the interface reaches the T_L . They then decrease rapidly up to the time at which the melt at the interface reaches the solidus temperature. This decrease is due to solidification occurring at the interface. Finally a further reduction of the IHTC with a slower rate happens up to the end of modeling time.

In order to better understand the mechanism of gap formation in the case of water-cooled chill conditions, the variation of interface temperature in the casting and chill domains has been plotted as a function of time for castings 5 and 6 together with the variation in the IHTC. The results are shown in Figure 6.11 and 6.12, for casting 5 and 6, respectively. To aid in the discussion, a schematic diagram showing the three stages in interface behavior that are consistent

with the model predicted IHTC variation have also been drawn for castings 5 and 6 in Figures 6.12 and 6.14, respectively.

Stage 1 – Referring to Figure 6.11 (a), the IHTC is at its highest value from the beginning of the casting process to 2 seconds, by which time the casting temperature at the interface has decreased from the pouring temperature to T_L . Figure 6.12 (a) shows good contact between the casting and the chill during this stage for the reasons described previously in Stage 1 for the solid chill.

Stage 2 – At the liquidus temperature - i.e. approximately 2 seconds elapsed time shown in Figure 6.11 (a) and (b) - the phase change from liquid to solid starts at the interface. During this stage, the contact between the casting and the chill begins to degrade and conformation to some of the chill asperities is lost, as can be seen in Figure 6.12 (b). Referring to Figure 6.11 (a) and (b), it can be seen that the IHTC decreases rapidly after 2 seconds elapsed time, when the casting at the interface is at T_L , to about 20 seconds when it reaches to solidus temperature.

Stage 3 – In Stage 3 shown in Figure 6.11 (a) and (b), after the casting at the interface reaches T_S , the rate of temperature decrease at the interface in the casting remains noticeably high, in comparison to what was observed with the solid chill. In addition, the IHTC remains constant from approximately 20 until 50 seconds and then begins to decrease rapidly, although slower than the rate in stage 2. The high heat extraction capacity of the water keeps the chill at a low temperature maintaining high heat extraction rates. It would appear that this results in a delay in gap formation until about 50 s, as is shown in Figure 6.12 (c), when an appreciable amount of

solidification has occurred in the casting and it begins to shrink away from the chill which remains relatively cool and does not expand or contract.

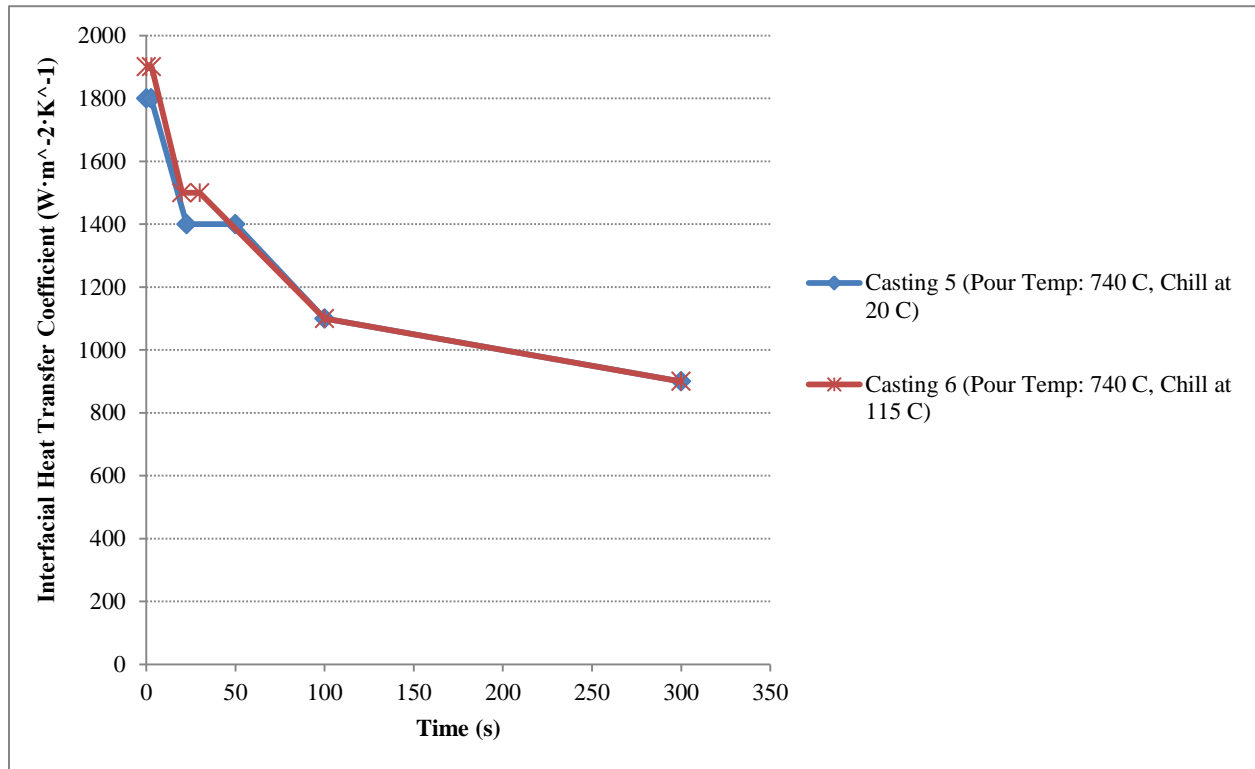


Figure 6.10: Time dependent melt/chill interfacial heat transfer coefficient for water-cooled conditions

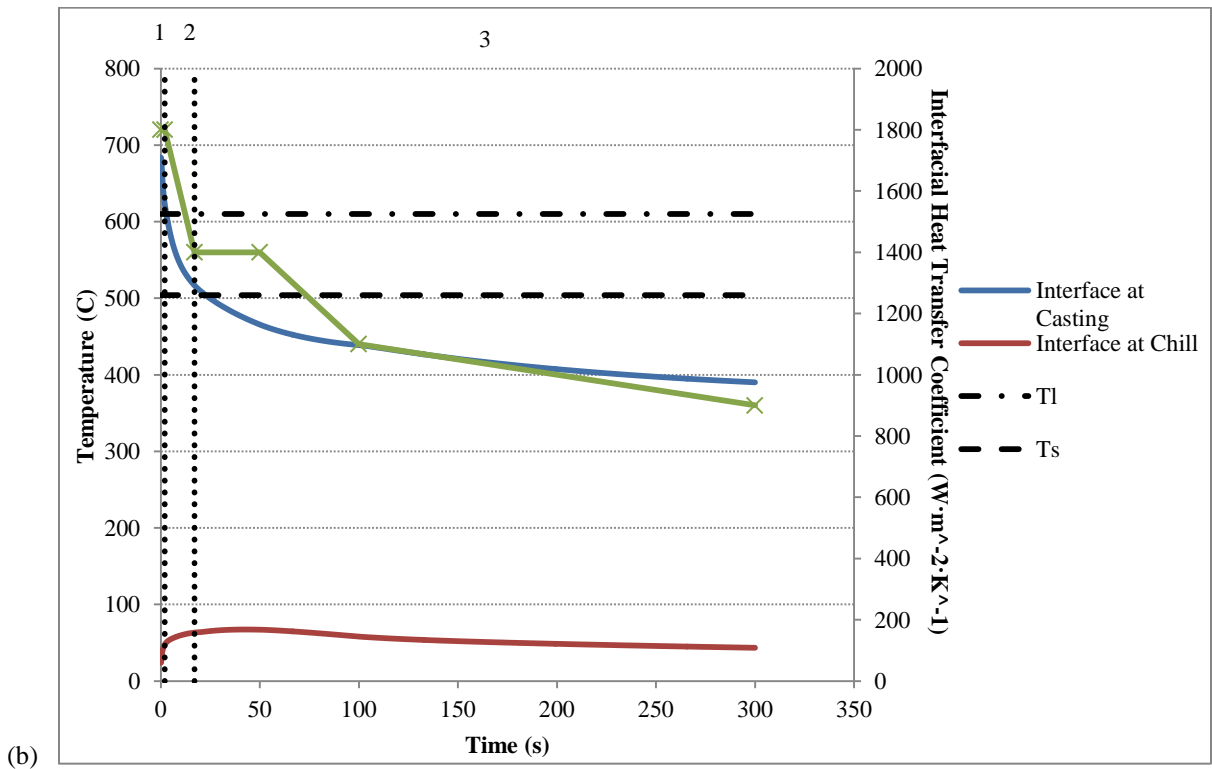
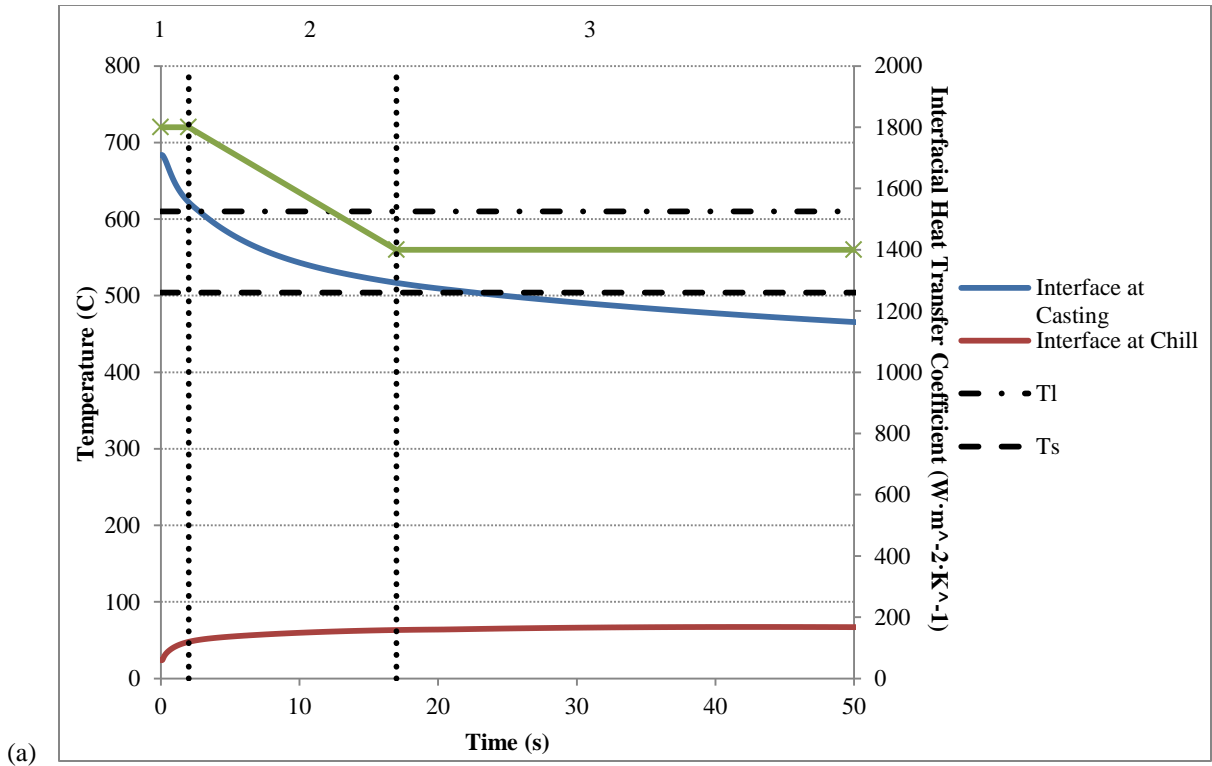


Figure 6.11: The temperature variation of the interface at casting domain, and the time dependent IHTC, casting 5

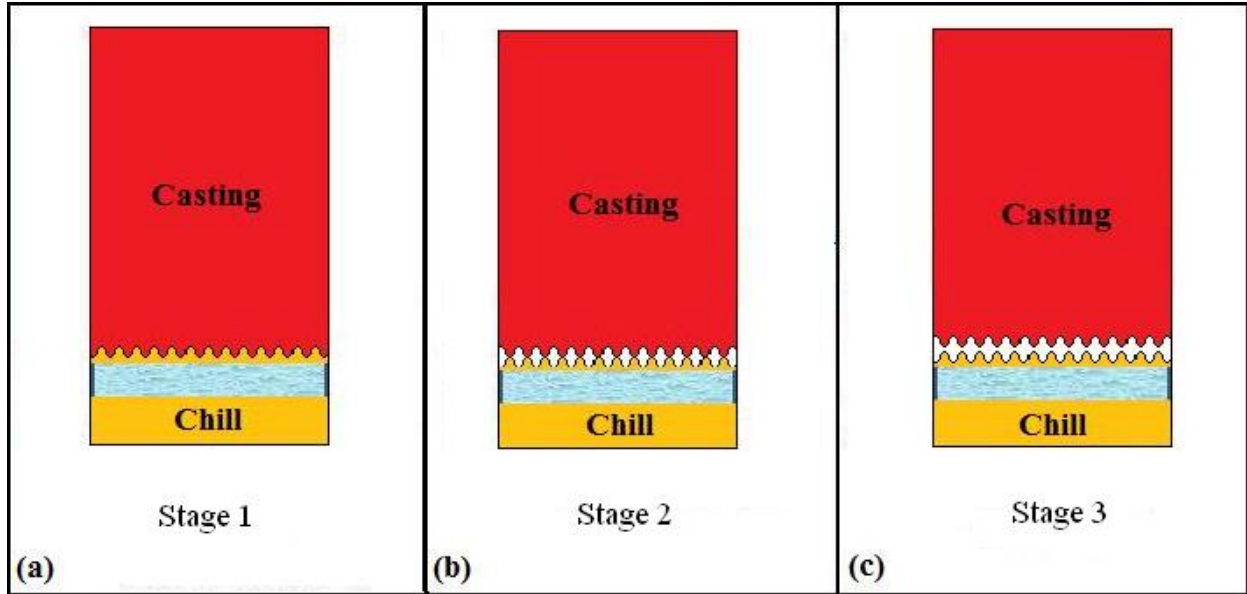


Figure 6.12: The schematic of the Casting/Chill interface behavior in standard water-cooled chill condition

Figure 6.13 shows the casting/chill resistance and interface temperature behavior in casting 6, in which the onset of water-cooling was delayed. The same three stages of behavior observed in the other castings are also observed in the delayed water-cooled casting and are shown schematically in Figure 6.14.

Referring to Figure 6.10, the initial interfacial heat transfer coefficient of the delayed water-cooled casting is predicted to be higher than that of the standard water-cooled casting. This is due to the higher initial chill temperature and lower initial cooling rate (associated with delayed water-cooling) which result in better initial contact or conformability of the chill and the molten metal.

There is one other difference observed between the standard water-cooled chill casting and the delayed water-cooled casting, which relates to the period of time that the IHTC remains constant

in stage 3. In the standard water-cooled casting this period of time is longer than in the delayed water-cooled casting. In the delayed water-cooled casting the end of the period of constant IHTC in stage 2, Figure 6.14 (b), corresponds to when the water is switched on and the chill begins to cool and shrink. The cooling of the chill and associated thermal contraction appears to accelerate the onset of gap formation relative to the standard water-cooled chill, which remains essentially at the same temperature and therefore does not shrink.

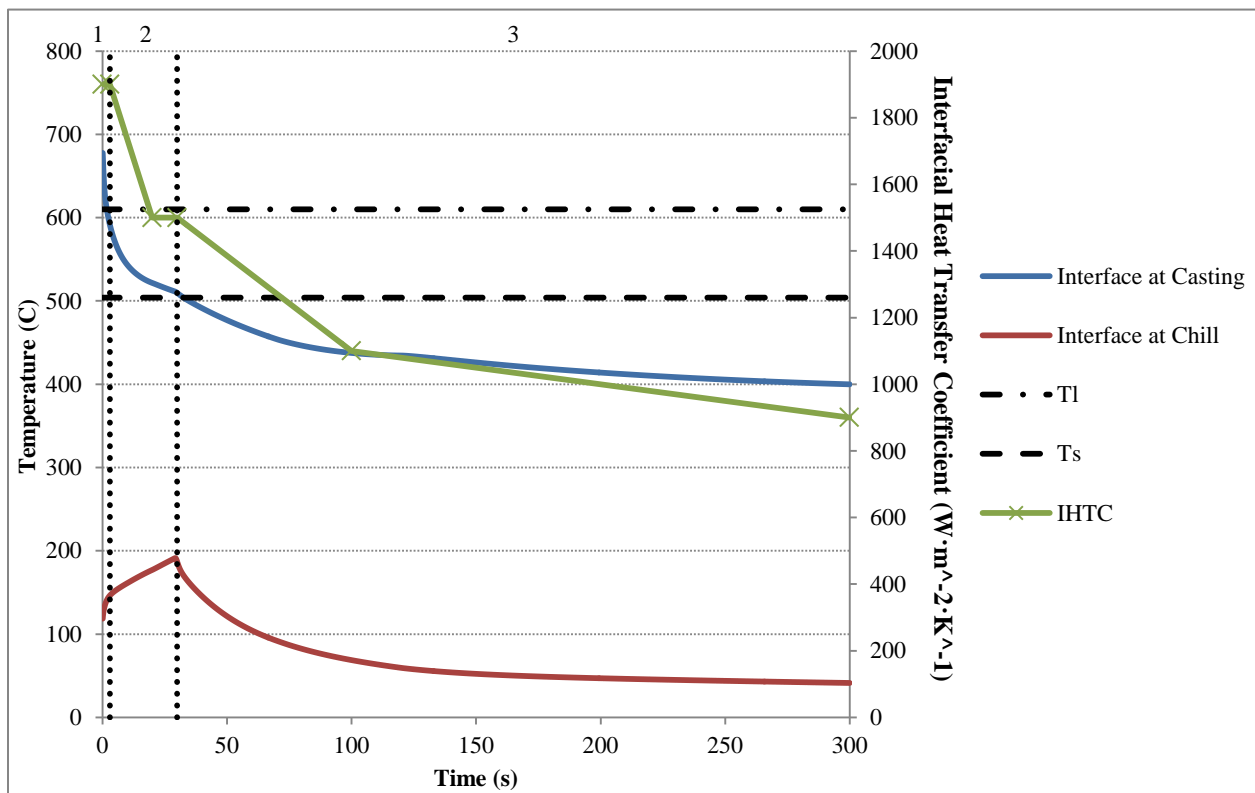


Figure 6.13: The temperature variation of the interface at casting domain, and the time dependent IHTC, casting 6

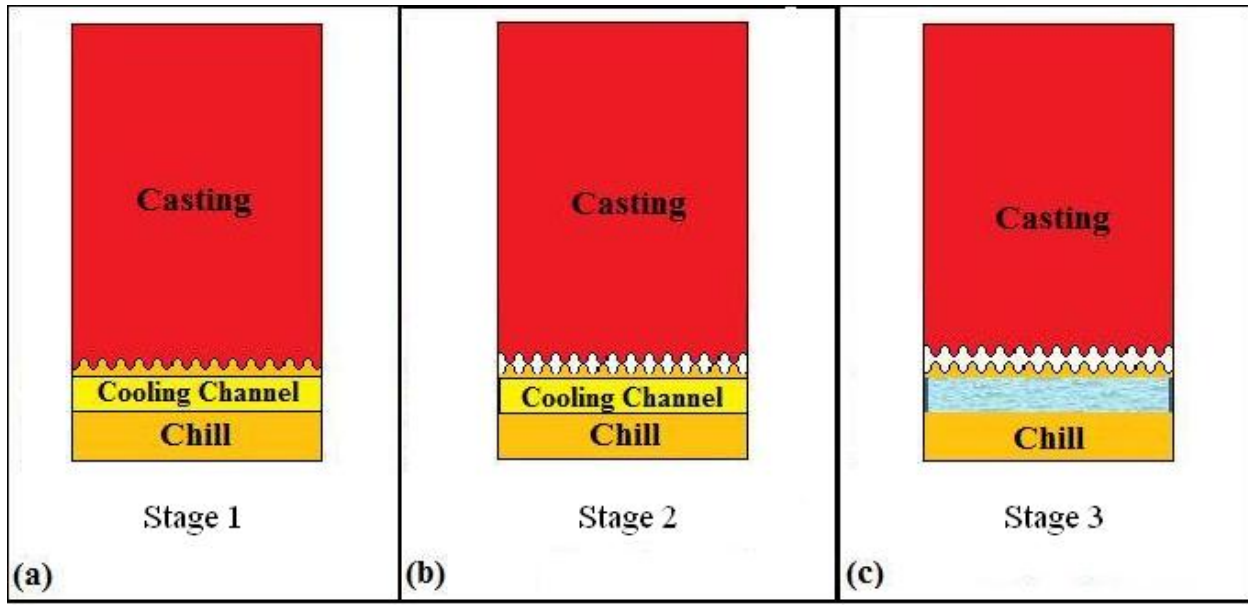
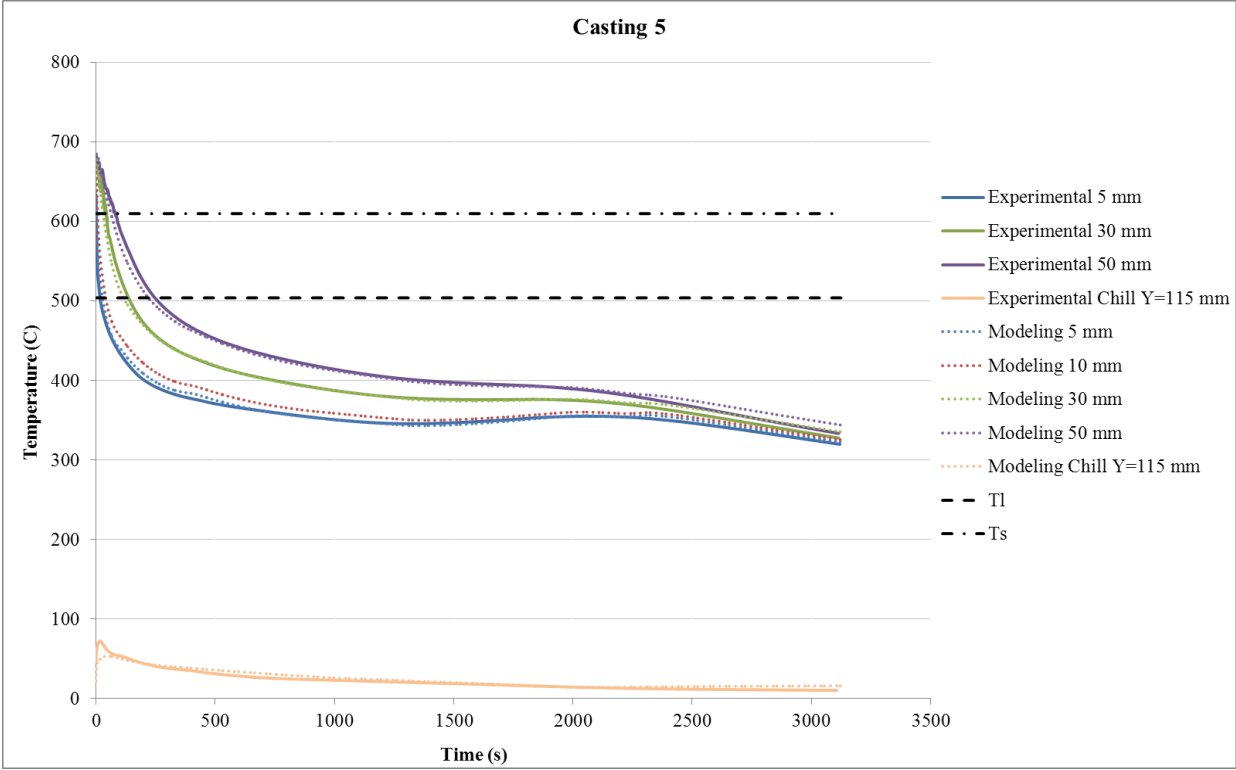


Figure 6.14: The schematic of the Casting/Chill interface behavior in delayed water-cooled chill condition

Comparison between the Interface Resistance of the Solid Chill and Water-Cooled Chill – To begin, it is important to articulate why the time dependent IHTC is needed to simulate the water-cooled chill experiments. Referring to Figure 6.15, which shows the measured and predicted variation in temperature with time in the casting and in the chill for casting 5, a moderate increase in casting temperature between 1200 and 2300 s at the 5 and 10 mm locations is observed. Using the model, the equivalent variation in the IHTC with temperature at the cast interface can be obtained and is shown in Figure 6.16 (this has been generated based on the IHTC variation with time input to the model). As can be seen the variation in the interface resistance with temperature yields multiple values of IHTC for the same temperature which can not be managed by a single temperature dependent function. Ultimately, this problem occurs in the two water-cooled castings because the rate of heat transfer is much higher due to the increased driving force (temperature difference across the interface), which is maintained by

cooling the chill with water. As a result, the increased development of the gap at longer times significantly reduces heat transport resulting in a temperature rebound in the casting.



6.15: Comparison between model prediction and experimental data for casting 5

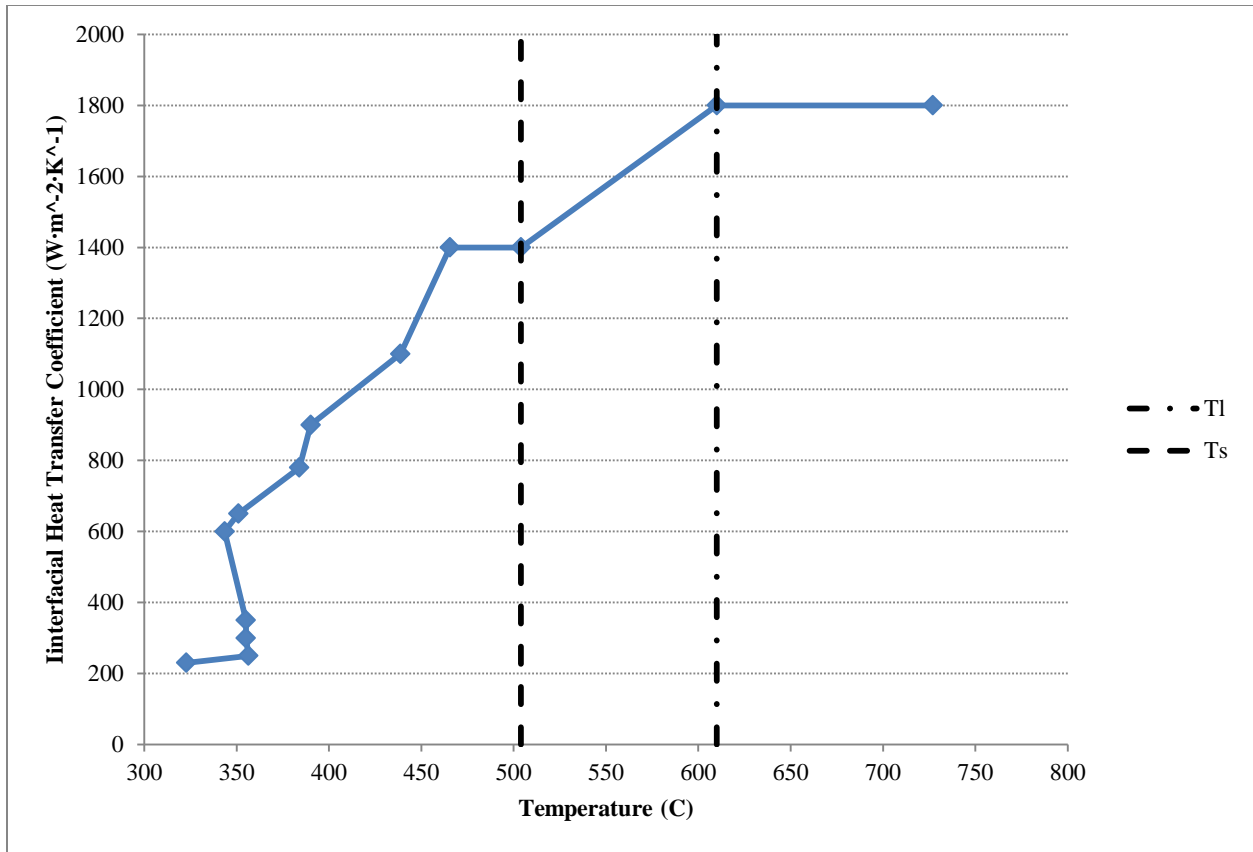
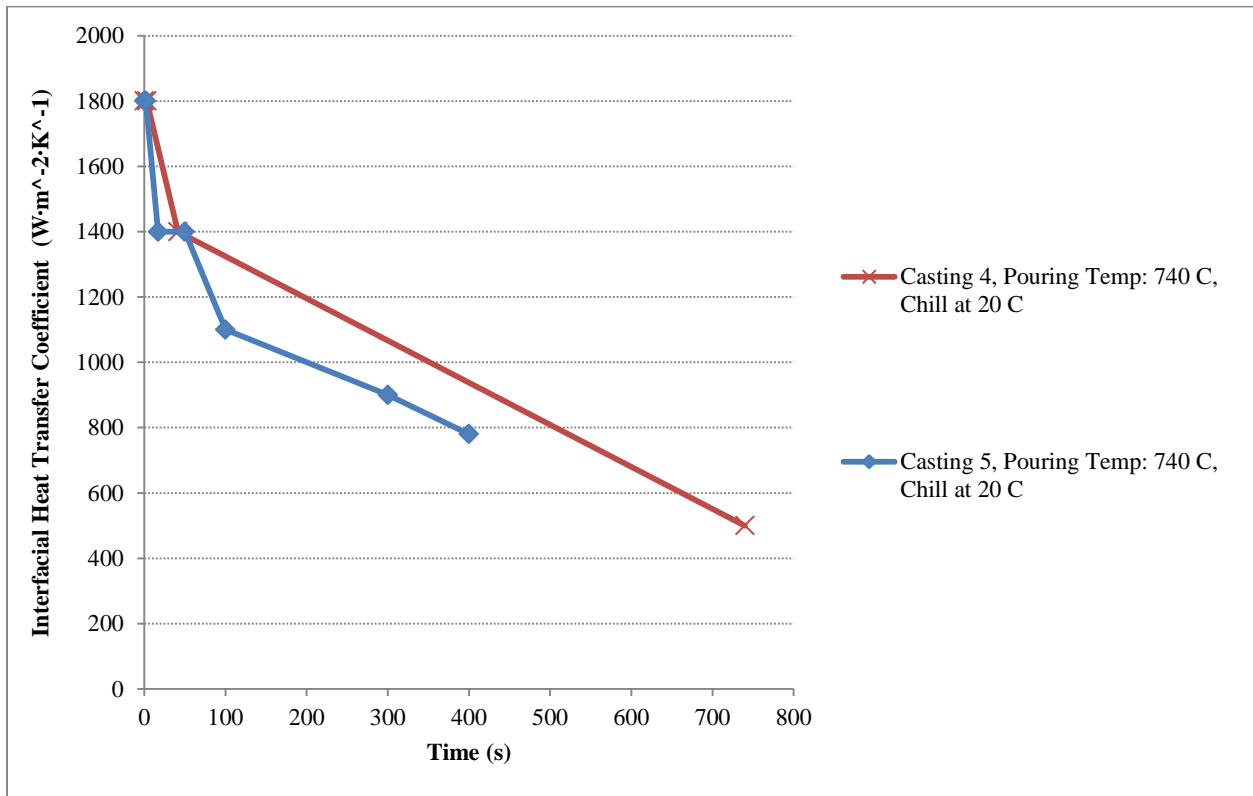


Figure 6.16: The variation of the applied IHTC with temperature

To further explore the difference between interface behavior in the solid and water-cooled chill castings, the variation in the IHTC with time for casting 4 and casting 5 have been compared and are shown in Figure 6.17. Casting 4 and casting 5 are chosen for comparison because they have the same casting conditions - i.e. the same pouring temperature and chill initial temperature.

As can be observed in Figure 6.17, the IHTC starts at the same value for both castings, but it decreases more rapidly with time in casting 5. This is probably due to the higher rate of gap formation in casting 5 resulting in bigger gap size and higher thermal resistance at the interface. In casting 5, the water maintains the chill at a low temperature; hence, the chill does not expand towards the interface when the solidifying casting is moving away from the interface. This

results in a higher thermal resistance at the interface and smaller interfacial heat transfer coefficient. In contrast, in the solid chill experiments the chill heats up significantly and the resulting expansion compensates to some degree for the casting contracting away from the interface due to solidification shrinkage.



6.17: Time dependent IHTC comparison Between casting 4 and casting 5

Presenting the data in a different way, Figure 6.18 shows the variation of IHTC with temperature for casting 4 and casting 5. Based on this graph, the two models predict the same heat transfer coefficient and evolution with temperature from the beginning of the casting process through the solidus temperature. This behavior is consistent with Stage 1 and 2 interface evolution as was previously proposed that it does not involve gap formation and substantial displacement of the casting and chill interfaces.

After the solidus temperature, the IHTC value for casting 5 remains higher than the IHTC applied to casting 4 at the same interface temperature. Referring to Figure 6.19, which shows the temperature variation with distance from the chill for the two castings, it reveals that the IHTC for the water-cooled chill casting is higher due to the fact that there has been less solidification in the water-cooled chill condition, resulting in a better contact between the casting and the chill.

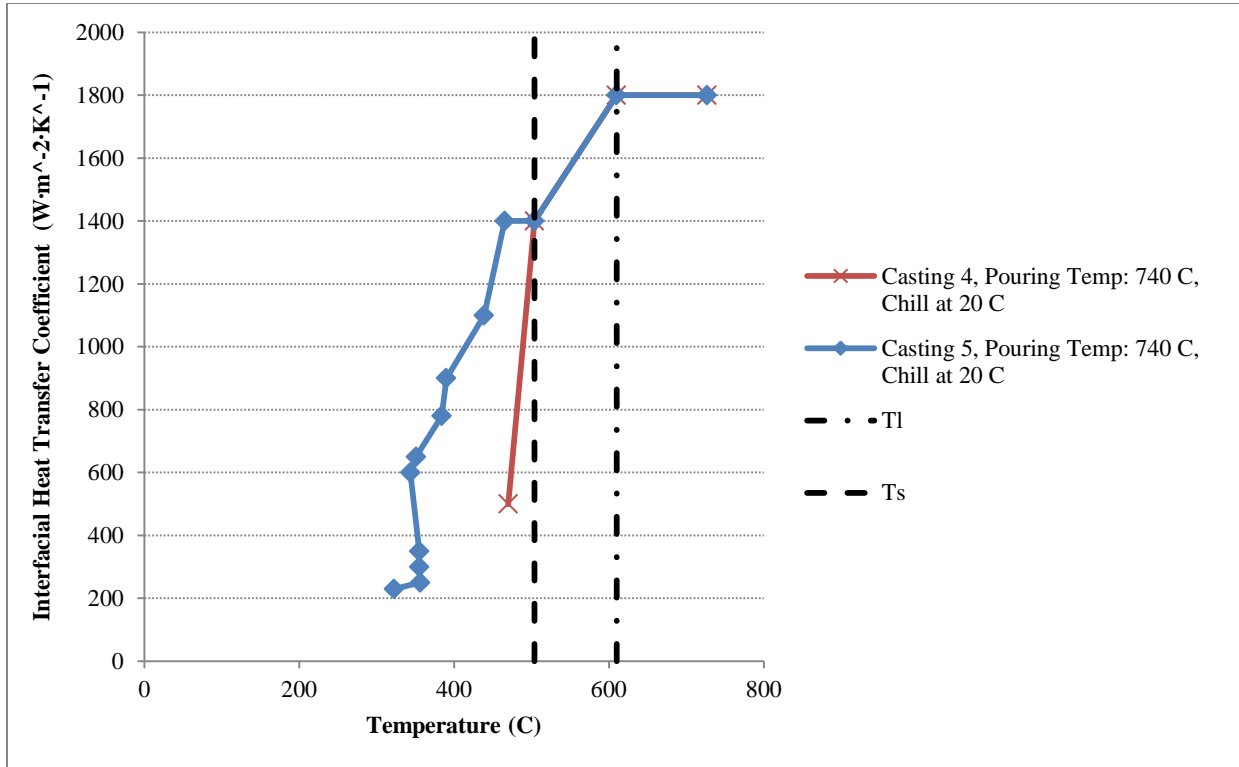
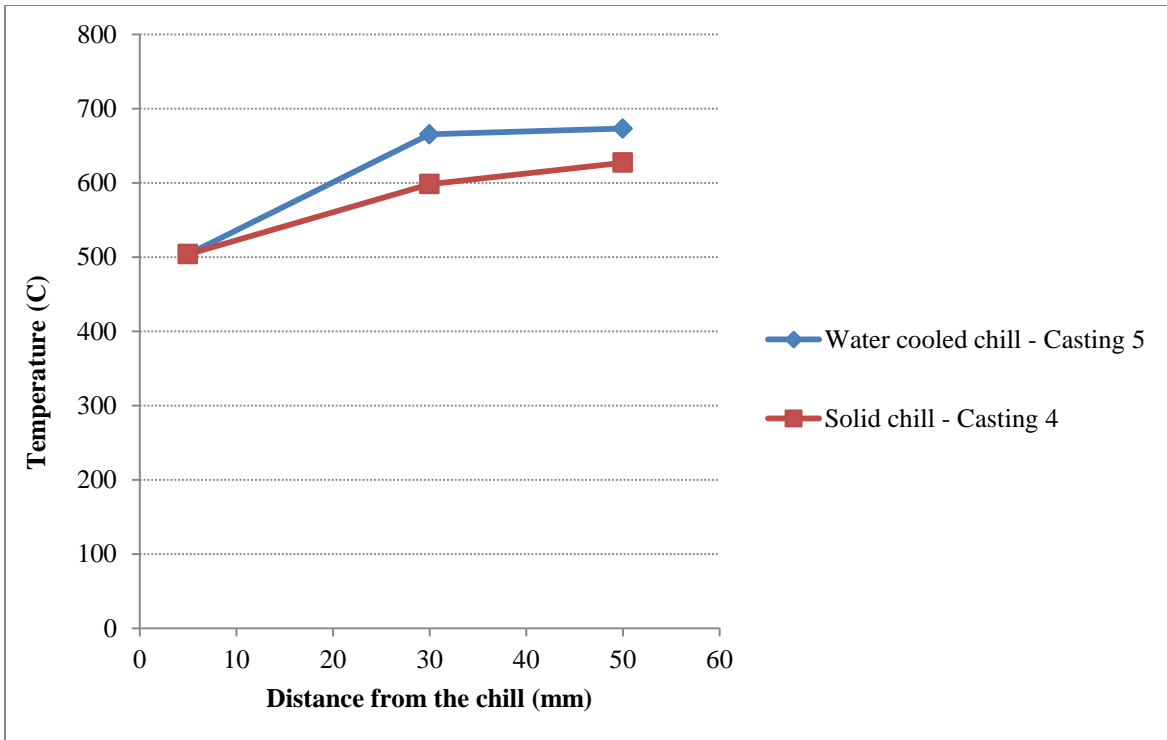


Figure 6.18: The variation of IHTC with temperature for casting 4 and casting 5



6.19: Temperature variation with distance from the chill

6.2.2. Casting/Mold Heat Transfer Coefficient

Figure 6.20 shows the heat transfer coefficient applied to the casting/mold boundary in all the models. When molten metal is first poured into the mold cavity, it makes a good contact with the mold surface, and the heat transfer coefficient is at its highest value. Then, the sand mold expands outward, since it is heated up by the metal. At this time, the liquid to solid phase change causes shrinkage in the metal and the casting starts to move inward. This is the instant when gap starts to form, leading to a steep decrease in the heat transfer coefficient, as is shown in Figure 6.20.

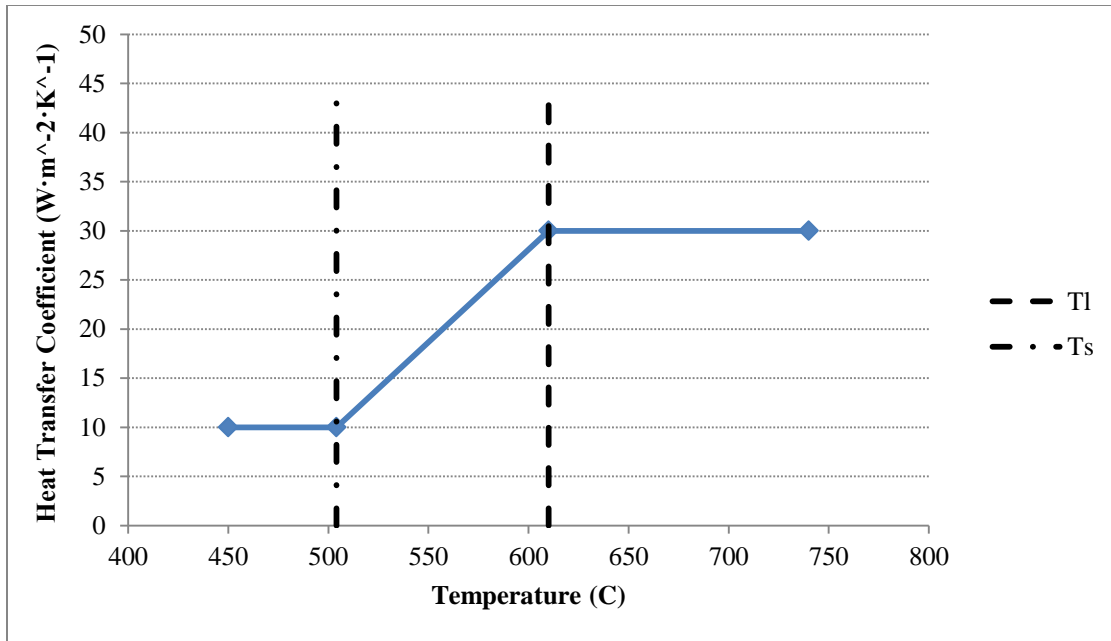


Figure 6.20: Temperature dependent casting/mold heat transfer coefficient

The temperature of the mold adjacent to the casting was defined as a function of time using a trial and error approach, as can be seen in Figures 6.21.

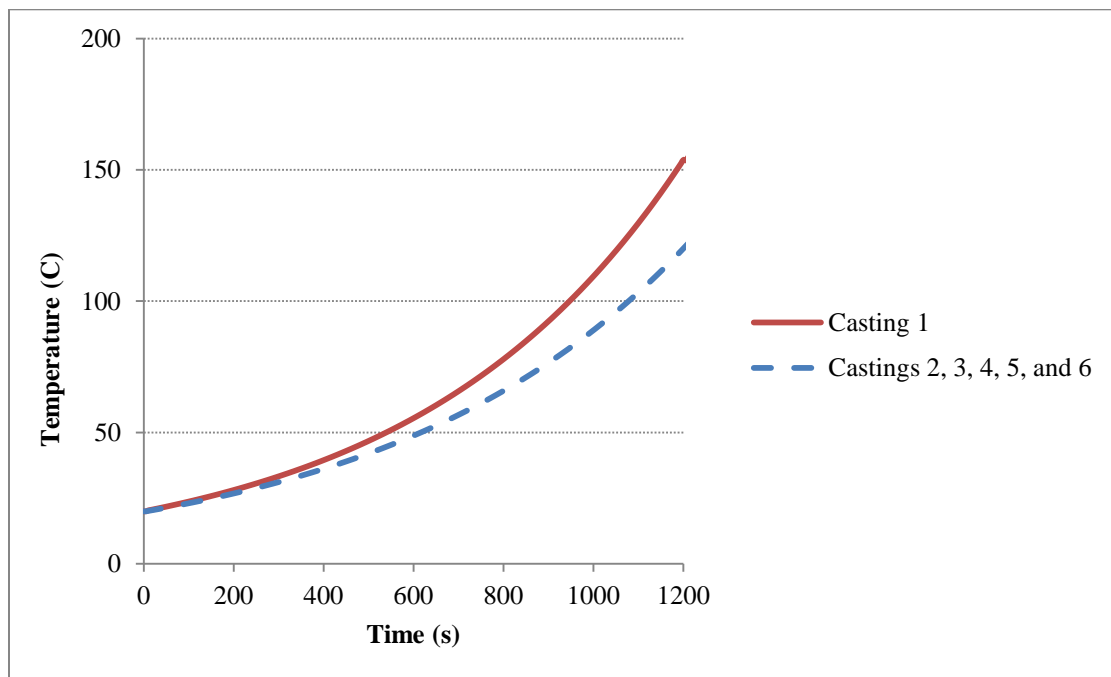


Figure 6.21: The temperature of the mold adjacent to the casting as a function of time ($T_{\text{casting/mold}}$)

It was assumed that the temperature of the mold increases exponentially, after the metal comes in contact with the mold. In the case of casting 1, a higher mold temperature was adopted, since the super heat in this casting is higher than the other experiments.

6.2.3. Chill/Mold Heat Transfer Coefficient

Figure 6.22 shows the heat transfer coefficient applied to the chill/mold boundary in all the simulations. When the chill heats up, it expands and so, makes better contact with the mold surface. Hence, the heat transfer coefficient increases. It was assumed that the increase in the heat transfer coefficient between the chill and the mold is linear.

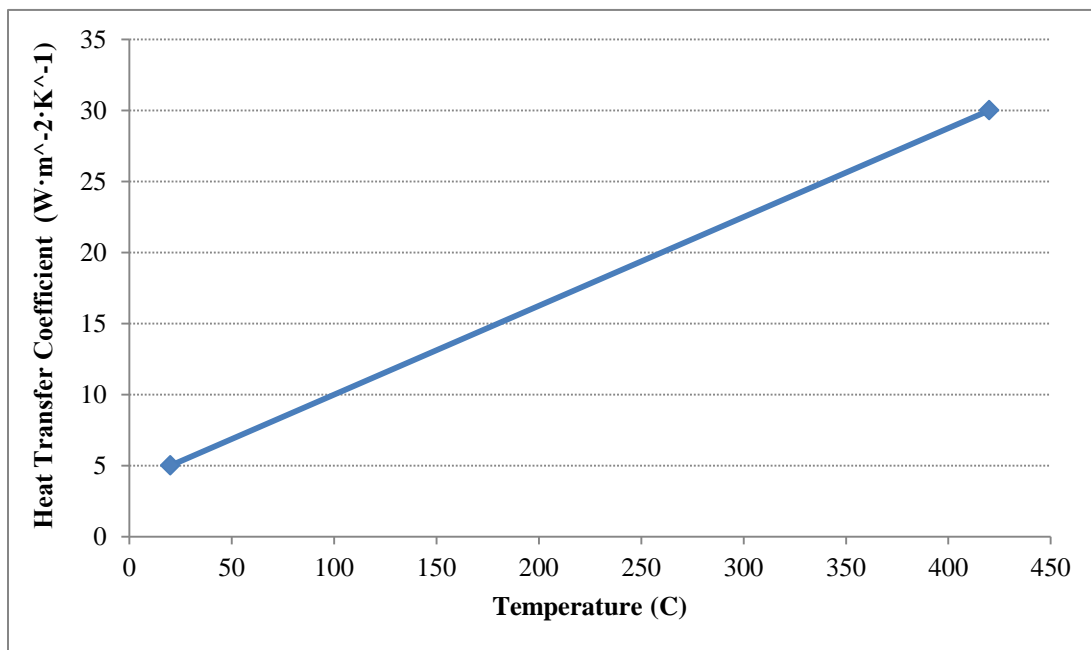


Figure 6.22: Temperature dependent chill/mold heat transfer coefficient

The temperature of the mold adjacent to the solid chill surface was defined as a function of time using trial and error approach, which is shown in Figure 6.23. It was assumed that during the

heat transfer between the hot chill and the sand mold, the temperature of the mold increases exponentially, and reaches a constant amount when the chill reaches its maximum temperature.

For the case of water-cooled chills, the mold temperature was set to 30 °C.

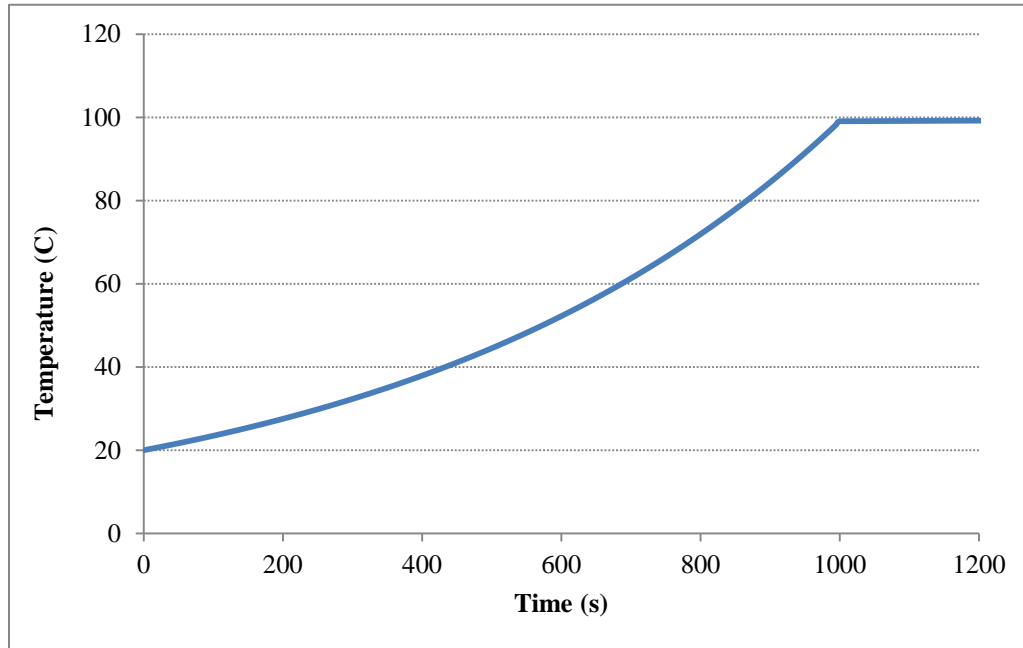


Figure 6.23: Temperature of the sand mold adjacent to the solid chill surface as a function of time ($T_{\text{Chill/Mold}}$)

7. Sensitivity Analysis

A sensitivity analysis was performed to determine the impact of key parameters on the predictions of the thermal model. The factors investigated include the mesh size, the size of the time step, the chill/casting interfacial heat transfer coefficient, casting/mold heat transfer coefficient, chill/mold heat transfer coefficient, and the temperature of the mold.

The mesh size and time step size were originally included in the analysis. The $\pm 30\%$ mesh size change and $\pm 50\%$ change in the time step size revealed no sensitivity in the thermal model predictions.

In order to reduce the computation time, the analyses were performed for conditions representing casting 1 and casting 5. Casting 1 was chosen because it has the combination of highest super heat and initial chill temperature, which resulted in the lowest cooling rate among all the castings. Casting 5 was also chosen because it represents the highest cooling rate among the castings.

The initial and boundary conditions described in Chapter 5 were employed as the baseline conditions. The investigated factors and the percentage of variations applied to them are summarized in Table 7.1.

Table 7.1: List of sensitivity analysis factors being investigated

Sensitive Factor	Variations
IHTC	$\pm 30\%$
Casting/Mold heat transfer coefficient	$\pm 30\%$
Chill/Mold heat transfer coefficient	$\pm 30\%$
Mold temperature	$\pm 30\%$

7.1. Chill/Casting Interfacial Heat Transfer Coefficient ($h_{\text{Chill/Casting}}$)

Figures 7.1 and 7.2 show the baseline simulation results and the simulation results for $\pm 30\%$ changes in the chill/casting interfacial heat transfer coefficient, for casting 1 and casting 5, respectively. In these figures, solid lines show the results for the base model, dashed lines represent the results for -30% change in $h_{\text{Chill/Casting}}$, and the dotted lines indicate the results for $+30\%$ change in $h_{\text{Casting/Mold}}$.

As can be observed from Figure 7.1 the thermal model for the case of the solid chill shows a low degree of sensitivity to the $\pm 30\%$ changes in the casting/chill interfacial heat transfer coefficient. An approximately $\pm 2.5\%$ deviation from the baseline results has been observed in the results with higher heat transfer coefficient resulting in higher cooling rate, and vice versa.

Turning to the results shown in Figure 7.2, the thermal model for casting 5 shows a high degree of sensitivity to the $\pm 30\%$ change made to the time dependent heat transfer coefficient ($h_{\text{Chill/Casting}}(t)$). A significant deviation of approximately $\pm 10\%$ from the base simulation results has been observed in the case of casting 5.

Both models are sensitive to the IHTC change, but the sensitivity is significantly higher in the case of the water-cooled chill –i.e. casting 5.

$$q = h(T_{\text{Casting}} - T_{\text{Chill}}) \quad (7.1)$$

According to Equation 7.1, which was previously discussed in Chapter 5, there are two limiting factors affecting the heat flux, q . For the solid chill, the limiting factor is the driving force for heat transfer –i.e. $(T_{\text{Casting}} - T_{\text{Chill}})$, since the temperature difference between the casting and the

chill is relatively small, and a change in the interface heat transfer coefficient does not lead to a significant change in the modeling results. The limiting factor for the standard water-cooled chill is the heat transfer coefficient –i.e. h , since the temperature difference between the casting and the chill is significantly high, and the model is highly sensitive to a small change in the heat transfer coefficient.

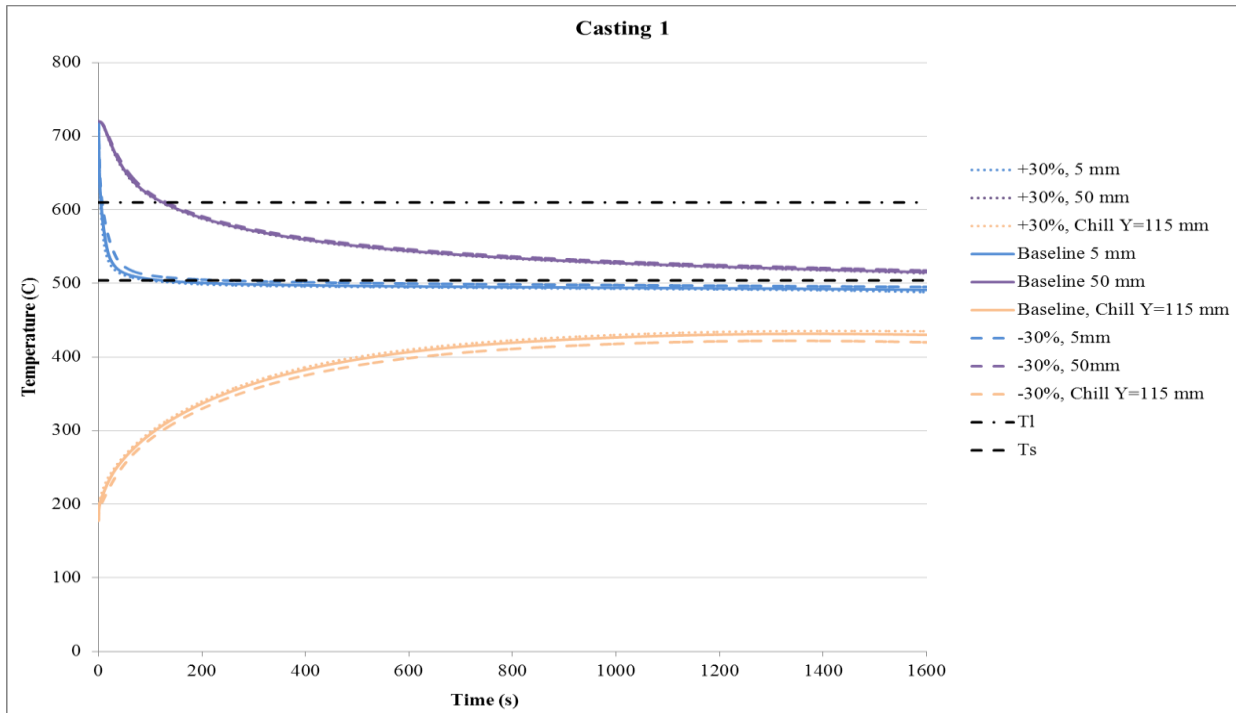


Figure 7.1: Sensitivity of thermal model to the temperature dependent chill/casting interfacial heat transfer coefficient

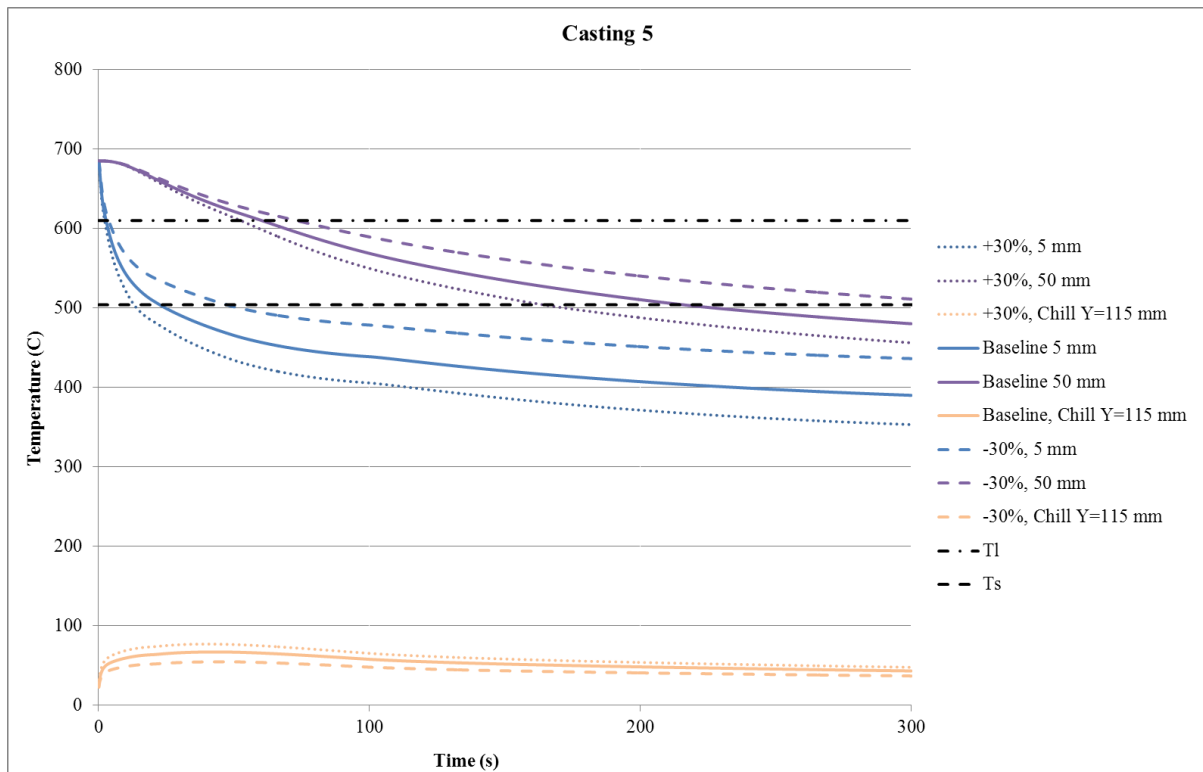


Figure 7.2: Sensitivity of the thermal model to the time dependent chill/casting interfacial heat transfer coefficient

7.2. Casting/Mold Heat Transfer Coefficient ($h_{\text{Casting/Mold}}(T)$)

Figures 7.3 and 7.4 show the baseline simulation results and the simulation results for $\pm 30\%$ changes in the temperature dependent casting/mold heat transfer coefficient ($h_{\text{Casting/Mold}}(T)$) for casting 1 and casting 5, respectively. In these figures, the solid lines show the results for the base model, dashed lines represent the results for -30% change in $h_{\text{Casting/Mold}}(T)$, and the dotted lines indicate the results for $+30\%$ change in $h_{\text{Casting/Mold}}(T)$.

As can be seen from Figure 7.3, at shorter times, the thermal model is relatively insensitive to the change in casting/mold heat transfer coefficient. However, a moderate sensitivity can be observed at longer times in both casting and chill monitor points. This happens because the solid

chill heats up more quickly at lower casting/mold heat transfer coefficient, limiting its ability to extract heat from the casting. At higher casting/mold heat transfer coefficient, however, more heat is extracted by conduction through the sand mold, hence, the model reports lower temperatures than the baseline results at both casting and chill domains.

Figure 7.4 shows that the model for water-cooled chill casting is relatively insensitive to the casting/mold heat transfer coefficient. This is due to the high heat extraction capacity of water-cooled chill that minimizes the effects of other boundaries.

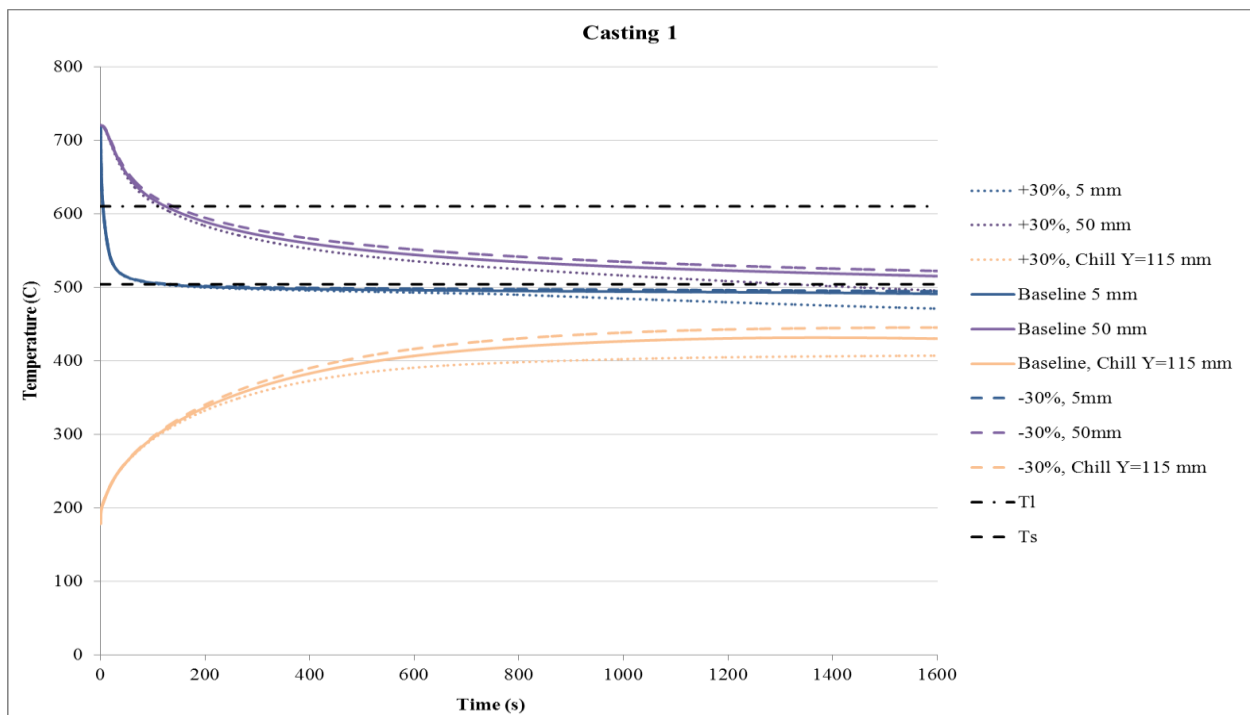


Figure 7.3: Sensitivity of the thermal model to the temperature dependent casting/mold heat transfer coefficient

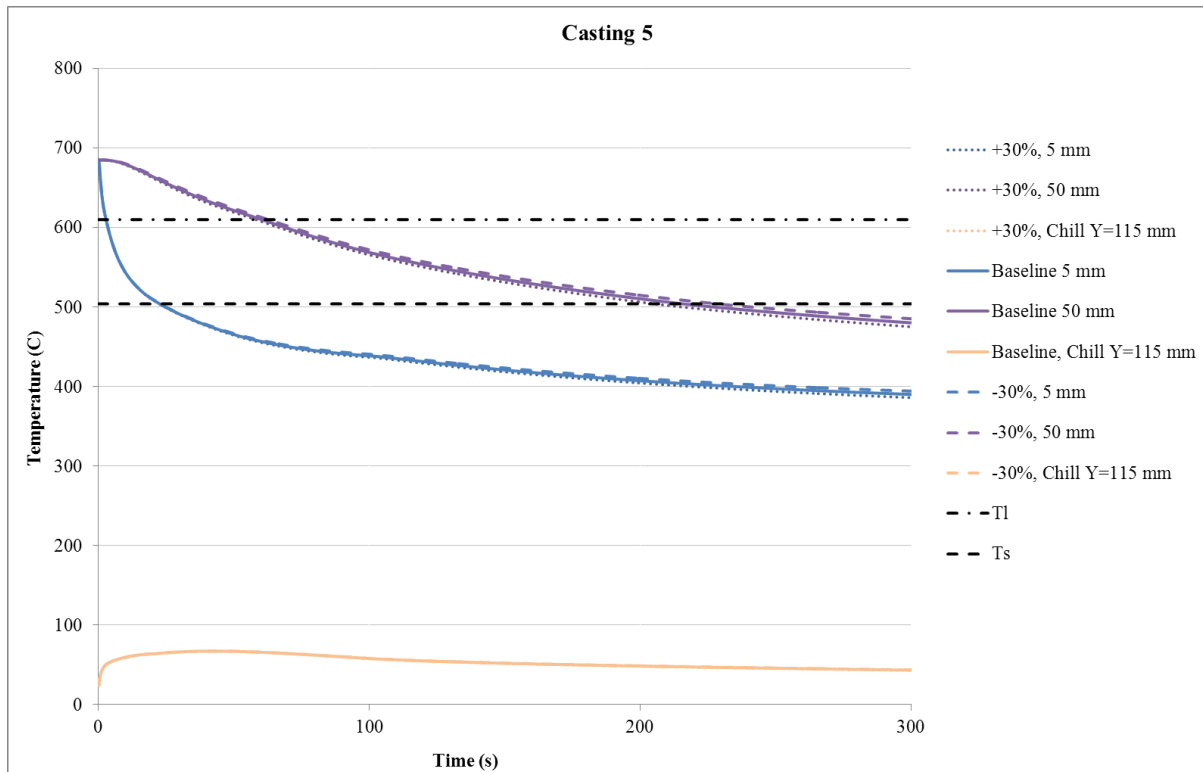


Figure 7.4: Sensitivity of the thermal model to the temperature dependent casting/mold heat transfer coefficient

7.3. Chill/Mold Heat Transfer Coefficient ($h_{\text{Chill/Mold}}(T)$)

Figures 7.5 and 7.6 show the baseline simulation results and the simulation results for $\pm 30\%$ changes in the temperature dependent chill/mold heat transfer coefficient ($h_{\text{Chill/Mold}}(T)$) for casting 1 and casting 5, respectively. In these figures, solid lines show the results for the base model, dashed lines represent the results for -30% change in $h_{\text{Chill/Mold}}(T)$, and the dotted lines the results for $+30\%$ change in $h_{\text{Chill/Mold}}(T)$.

As can be observed in Figure 7.5, the model shows a small degree of sensitivity at locations 5 and 50 mm from the chill in the casting at longer times. Also, an approximately 7.5% change from the baseline results has occurred in the solid chill temperature, since the transport of heat from the solid chill is limited by conduction through the sand mold.

Figure 7.6 shows that the model developed for casting 5 is insensitive to the chill/mold heat transfer coefficient, since the dominant mechanism of heat transfer takes place through the water cooling channel, and minimizes the effect of chill/mold heat transfer coefficient.

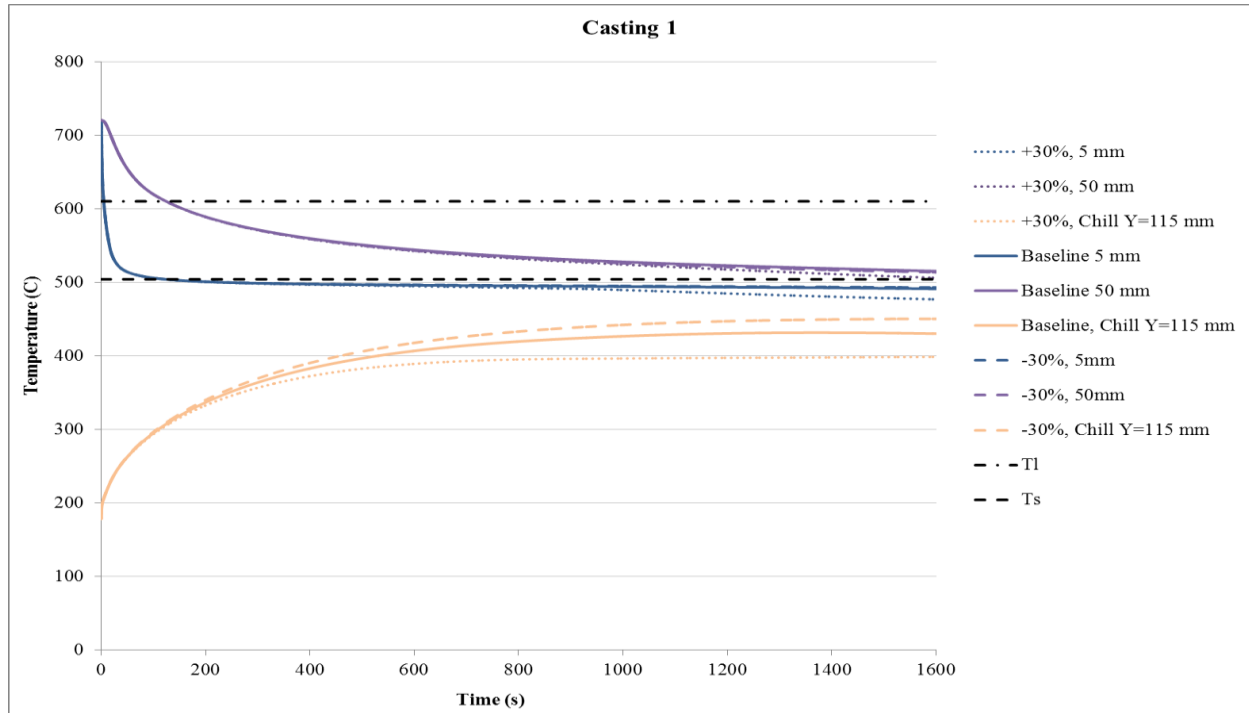


Figure 7.5: Sensitivity of the thermal model to the temperature dependent chill/mold heat transfer coefficient

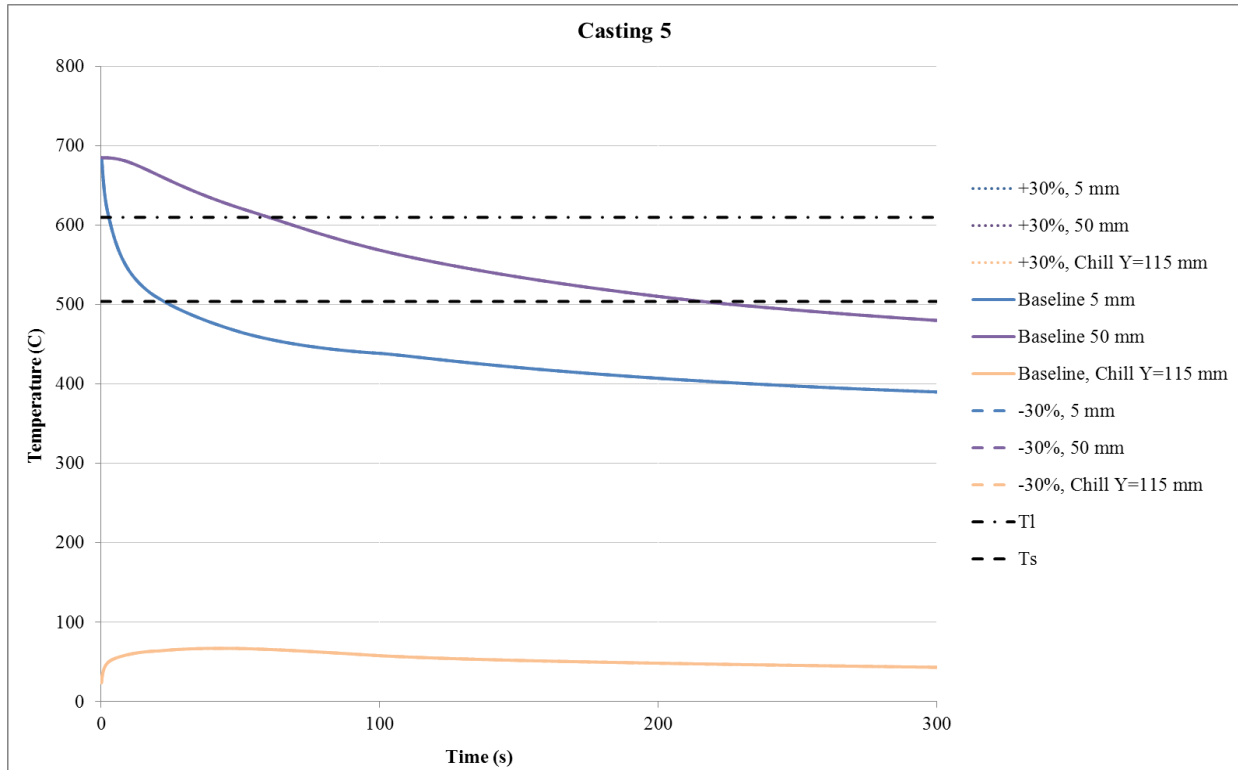


Figure 7.6: Sensitivity of the thermal model to the temperature dependent chill/mold heat transfer coefficient

7.4. Mold Temperature

Figures 7.7 and 7.8 show the baseline simulation results and the simulation results for $\pm 30\%$ changes in the mold temperature for casting 1 and casting 5, respectively. In these figures, solid lines show the results for the base model, dashed lines represent the results for -30% and the dotted lines the results for $+30\%$ change in mold temperature.

As can be observed in Figure 7.7, the model shows a very low degree of sensitivity at longer times for both of the $\pm 30\%$ changes in mold temperature, which is due to the reduction in the driving force for heat transport from the solid chill to the sand mold. Figure 7.8 shows that the model for the water-cooled chill casting is totally insensitive to the mold temperature.

Considering these results, it seems quite convincing that ignoring the sand mold geometry in the models to reduce the computational size, has been a good assumption.

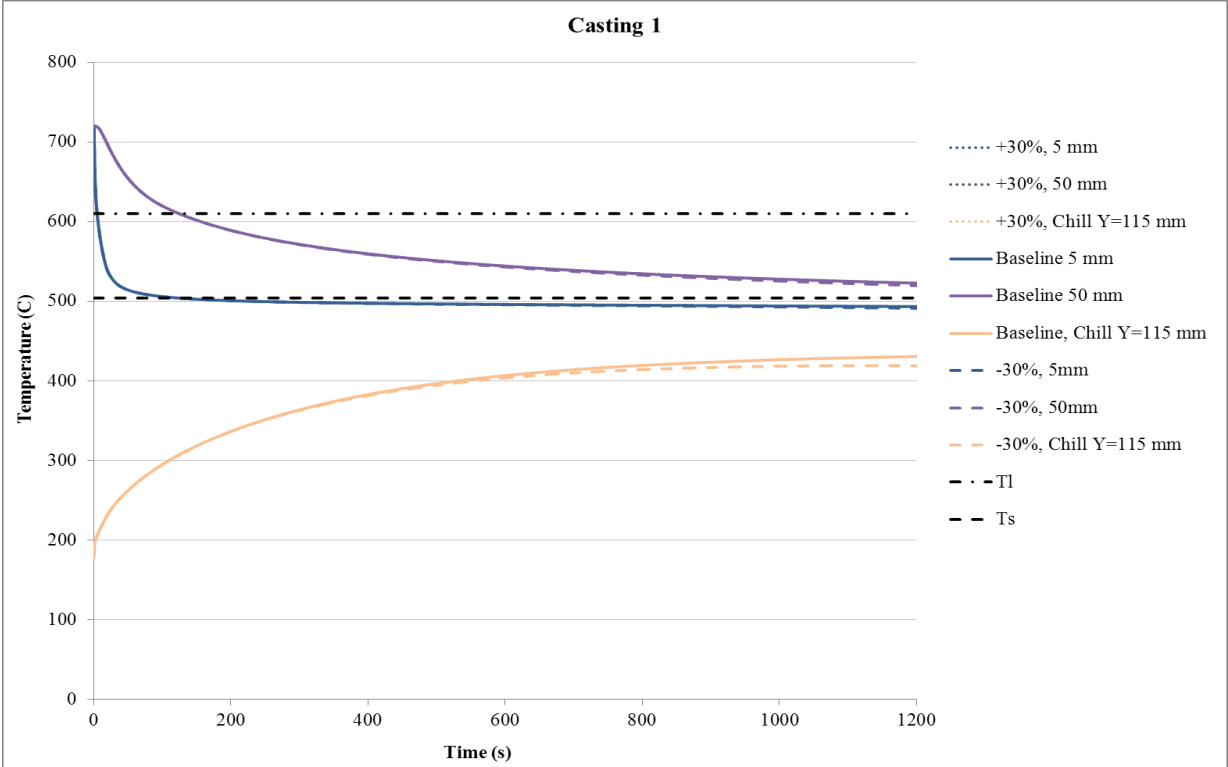


Figure 7.7: Sensitivity of the thermal model to the sand mold temperature

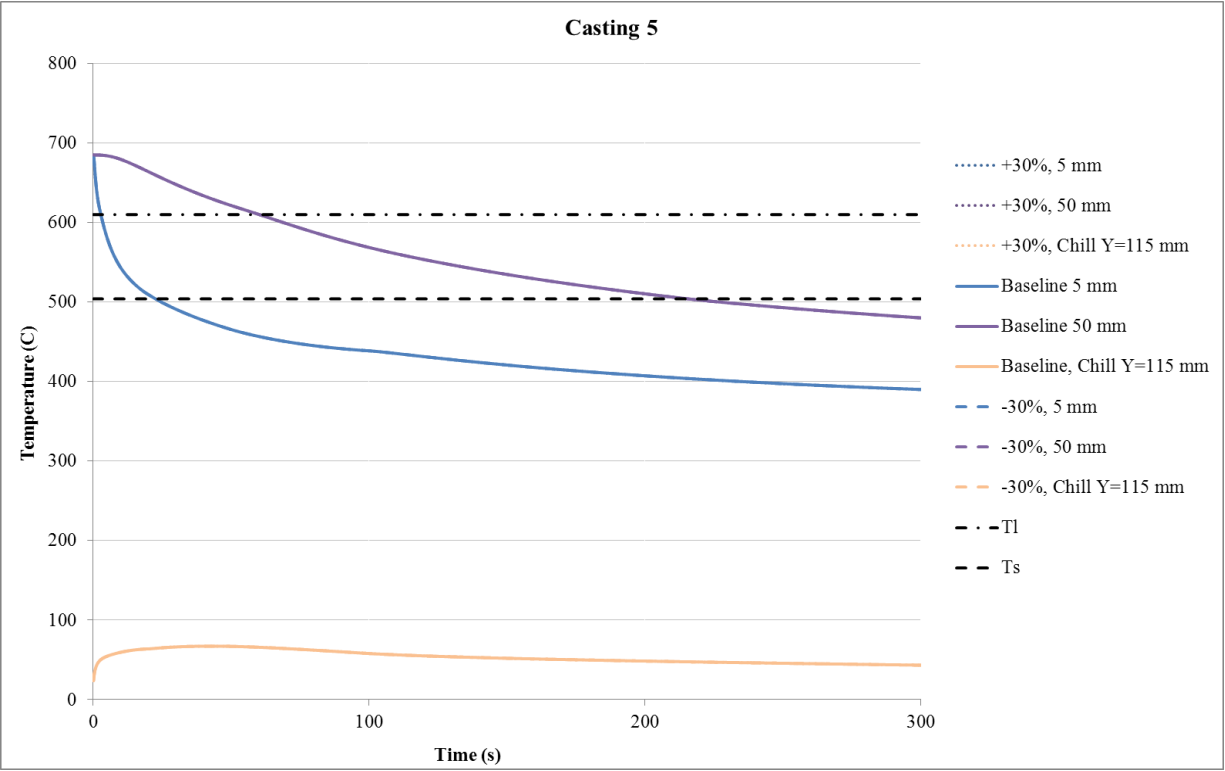


Figure 7.8: Sensitivity of the thermal model to the sand mold temperature

8. Summary and Conclusion

8.1. Conclusions

This research focused on the quantitative determination of the effectiveness of a water-cooled chill in making a balance between fine microstructure and proper mold filling for A319 alloy. Using the standard Nematik wedge-chill sand mold for assessment, a total of six castings with different cooling conditions were performed. A mathematical model has been developed in order to simulate thermal behavior of the casting/chill interface and also predict temperature variations with time in the casting and the chill.

The performance metrics quantified in this research included cooling rate variation as a function of time and distance from the chill, the associated microstructure length scale (SDAS) variation with distance from the chill and a quantitative assessment of the behavior of the interface heat transfer (between the chill and casting).

The main conclusions from this work are summarized as follows:

1. Generally, the microstructure of the solidified casting becomes progressively coarser with increasing distance from the chill. Also, the comparison between the results for the water-cooled chill casting and the solid chill casting have clearly shown that the SDAS sizes for the standard water-cooled chill condition are significantly lower than that of the solid chill case.

2. Water-cooling was found to have a significant effect on the cooling rate, while superheat was found to have a moderate effect and chill initial temperature only a small effect.
3. In both chill formats the IHTC decreased due to loss of contact at the interface and formation of a gap. The evolution in the IHTC with temperature and time is different for the two chill formats due to differences in the thermal expansion of the chill and contraction of the casting.
4. Switching the water on with a 10 seconds delay was shown to be effective in transitioning from an initial low cooling rate to a high cooling rate. The results show that this method has the potential to both avoid cold shuts and miss-runs at the areas close to the chill, and improve the cast microstructure farther into castings remote from the chill.
5. In comparison to the solid chill technology, the water-cooled technology allows for maintaining significant heat transfer even during gap formation due to large temperature difference between the casting and the chill.
6. The optimization of water-cooled chill technology will require effort to be applied to minimizing gap formation.

8.2. Recommendations for Future Work

In this research, the efficacy of a water-cooled chill in terms of its ability to make a balance between proper mold filling and fine microstructure was assessed quantitatively for A319 alloy sand casting. Although the microstructural evaluation and also development of a thermal model, predicting the casting/chill interface behavior have been included in the research, there is still some additional research required to aid the completion of the assessment. The additional research areas include:

1. A thermal stress analysis to quantitatively predict the formation of the gap at the casting/chill interface.
2. The analysis should be expanded to a more complicated geometry, which better represents the real engine block geometry.

References

- [1] D.O. Ovono, I. Guillot, D. Massinon, The microstructure and precipitation kinetics of a cast aluminium alloy, *Scr. Mater.* 55 (2006) 259-262.
- [2] V. Firouzdor, M. Rajabi, E. Nejati, F. Khomamizadeh, Effect of microstructural constituents on the thermal fatigue life of A319 aluminum alloy, *Materials Science and Engineering: A.* 454 (2007) 528-535.
- [3] D.M. Stefanescu, *ASM Handbook: Casting*, Asm Intl, 1992.
- [4] G. García-García, J. Espinoza-Cuadra, H. Mancha-Molinar, Copper content and cooling rate effects over second phase particles behavior in industrial aluminum-silicon alloy 319, *Mater Des.* 28 (2007) 428-433.
- [5] R.I. Mackay, D. Cusinato, J.H. Sokolowski, Chemistry optimisation to improve casting durability of engine blocks, (2009).
- [6] E.J. Martínez D, M.A. Cisneros G, S. Valtierra, J. Lacaze, Effect of strontium and cooling rate upon eutectic temperatures of A319 aluminum alloy, *Scr. Mater.* 52 (2005) 439-443.
- [7] M.J. Caton, J.W. Jones, J.M. Boileau, J.E. Allison, The effect of solidification rate on the growth of small fatigue cracks in a cast 319-type aluminum alloy, *Metallurgical and Materials Transactions A.* 30 (1999) 3055-3068.
- [8] K. Gall, N. Yang, M. Horstemeyer, D.L. McDowell, J. Fan, The debonding and fracture of Si particles during the fatigue of a cast Al-Si alloy, *Metallurgical and Materials Transactions A.* 30 (1999) 3079-3088.
- [9] H.R. Ammar, A.M. Samuel, F.H. Samuel, Porosity and the fatigue behavior of hypoeutectic and hypereutectic aluminum–silicon casting alloys, *Int. J. Fatigue.* 30 (2008) 1024-1035.
- [10] C.H. Caceres, M.B. Djurdjevic, T.J. Stockwell, J.H. Sokolowski, The effect of Cu content on the level of microporosity in Al-Si-Cu-Mg casting alloys, *Scr. Mater.* 42 (1999).
- [11] S.G. Shabestari, H. Moemeni, Effect of copper and solidification conditions on the microstructure and mechanical properties of Al–Si–Mg alloys, *J. Mater. Process. Technol.* 153 (2004) 193-198.
- [12] M. Dash, M. Makhlof, Effect of key alloying elements on the feeding characteristics of aluminum-silicon casting alloys, *Journal of Light Metals.* 1 (2001) 251-265.
- [13] G. Nicoletto, G. Anzelotti, R. Konečná, X-ray computed tomography vs. metallography for pore sizing and fatigue of cast Al-alloys, *Procedia Engineering.* 2 (2010) 547-554.

- [14] J. Linder, M. Axelsson, H. Nilsson, The influence of porosity on the fatigue life for sand and permanent mould cast aluminium, *Int. J. Fatigue*. 28 (2006) 1752-1758.
- [15] H.R. Ammar, A.M. Samuel, F.H. Samuel, Effect of casting imperfections on the fatigue life of 319-F and A356-T6 Al-Si casting alloys, *Materials Science and Engineering: A*. 473 (2008) 65-75.
- [16] S. Fintová, G. Anzelotti, R. Konečná, G. Nicoletto, Casting Pore Characterization by X-Ray Computed Tomography and Metallography, *Archive of Mechanical Engineering*. (2010) 263-273.
- [17] R.M. Glenn Byczynski, THE NEMAK COSWORTH CASTING PROCESS - INNOVATION, (2009).
- [18] S. Shabestari, M. Malekan, Thermal analysis study of the effect of the cooling rate on the microstructure and solidification parameters of 319 aluminum alloy, *Can. Metall. Q.* 44 (2005) 305-312.
- [19] S. Hayashi, J. Miyake, M. Koyama, K. Sakaguchi, Method for manufacturing a cylinder head of cast aluminum alloy for internal combustion engines by employing local heat treatment. (1987).
- [20] B. Zhang, D.R. Poirier, W. Chen, Microstructural effects on high-cycle fatigue-crack initiation in A356. 2 casting alloy, *Metallurgical and Materials Transactions A*. 30 (1999) 2659-2666.
- [21] R. Atwood, S. Sridhar, W. Zhang, P. Lee, Diffusion-controlled growth of hydrogen pores in aluminium-silicon castings: In situ observation and modelling, *Acta materialia*. 48 (2000) 405-417.
- [22] M.J. Caton, J.W. Jones, J.E. Allison, The influence of heat treatment and solidification time on the behavior of small-fatigue-cracks in a cast aluminum alloy, *Materials Science and Engineering: A*. 314 (2001) 81-85.
- [23] E.L. Rooy, *Properties and Selection: Nonferrous Alloys and Special-Purpose Materials*, 1992.
- [24] R.I. Mackay, J.H. Sokolowski, Effect of Si and Cu concentrations and solidification rate on soundness in casting structure in Al-8211; Si-8211; Cu alloys, *International Journal of Cast Metals Research*. 23 (2010) 7-22.
- [25] T.J. Smith, H. Sehitoglu, E. Fleury, H.J. Maier, J. Allison, Modeling high-temperature stress-strain behavior of cast aluminum alloys, *Metallurgical and Materials Transactions A*. 30 (1999) 133-146.

- [26] M.J. Caton, J.W. Jones, H. Mayer, S. Stanzl-Tschegg, J.E. Allison, Demonstration of an endurance limit in cast 319 aluminum, *Metallurgical and Materials Transactions A*. 34 (2003) 33-41.
- [27] M. Malekan, S. Shabestari, Computer-aided cooling curve thermal analysis used to predict the quality of aluminum alloys, *Journal of thermal analysis and calorimetry*. 103 (2011) 453-458.
- [28] C.C. Lee, K.N. Chiang, W.K. Chen, R.S. Chen, Design and analysis of gasket sealing of cylinder head under engine operation conditions, *Finite Elements Anal. Des.* 41 (2005) 1160-1174.
- [29] R.W. Grenkowitz, M.J. Braskich, A.D. Ackerman, Gravity precision sand casting of aluminum and equivalent metals. (1997).
- [30] S. Sulaiman, A. Hamouda, Modeling of the thermal history of the sand casting process, *J. Mater. Process. Technol.* 113 (2001) 245-250.
- [31] M.C. Flemings, Solidification processing, *Metallurgical and Materials Transactions B*. 5 (1974) 2121-2134.
- [32] I. SCOPE, Production and Inspection of Quality Aluminum and Iron Sand Castings, *Handbook of metallurgical process design*. 24 (2004) 349.
- [33] M.C. Flemings, Solidification processing, 1974, New York, London and Sydney.: McGraw-Hill Book Co.
- [34] H. Arami, R. Khalifehzadeh, M. Akbari, F. Khomamizadeh, Microporosity control and thermal-fatigue resistance of A319 aluminum foundry alloy, *Materials Science and Engineering: A*. 472 (2008) 107-114.
- [35] M. Bamberger, I. Minkoff, M. Stupel, Some observations on dendritic arm spacing in Al-Si-Mg and Al-Cu alloy chill castings, *J. Mater. Sci.* 21 (1986) 2781-2786.
- [36] N.D. DiMatteo, S.R. Lampman, K. Metals, *Knovel Plastics & Rubber Library, ASM Handbook, Volume 19: Fatigue and Fracture, ASM International, 1996.*
- [37] G.E. Dieter, D. Bacon, *Mechanical Metallurgy, McGraw-Hill New York, 1986.*
- [38] P. Li, P. Lee, D. Maijer, T. Lindley, Quantification of the interaction within defect populations on fatigue behavior in an aluminum alloy, *Acta Materialia*. 57 (2009) 3539-3548.
- [39] L. Dietrich, J. Radziejewska, The fatigue damage development in a cast Al-Si-Cu alloy, *Mater Des.* 32 (2011) 322-329.

- [40] D. Casellas, R. Pérez, J.M. Prado, Fatigue variability in Al–Si cast alloys, *Materials Science and Engineering: A*. 398 (2005) 171-179.
- [41] S. Shabestari, M. Malekan, Assessment of the effect of grain refinement on the solidification characteristics of 319 aluminum alloy using thermal analysis, *J. Alloys Compounds*. 492 (2010) 134-142.
- [42] J. Campbell, Solidification modelling: current limitations and future potential, *Materials science and technology*. 7 (1991) 885-894.
- [43] P. Lee, A. Chirazi, D. See, Modeling microporosity in aluminum-silicon alloys: a review, *Journal of Light Metals*. 1 (2001) 15-30.
- [44] Q.G. Wang, P.E. Jones, Prediction of fatigue performance in aluminum shape castings containing defects, *Metallurgical and Materials Transactions B*. 38 (2007) 615-621.
- [45] K.D. Carlson, Z. Lin, C. Beckermann, Modeling the effect of finite-rate hydrogen diffusion on porosity formation in aluminum alloys, *Metallurgical and Materials Transactions B*. 38 (2007) 541-555.
- [46] O. Lashkari, L. Yao, S. Cockcroft, D. Maijer, X-ray microtomographic characterization of porosity in aluminum alloy A356, *Metallurgical and Materials Transactions A*. 40 (2009) 991-999.
- [47] Q.G. Wang, D. Apelian, D.A. Lados, Fatigue behavior of A356/357 aluminum cast alloys. Part II-Effect of microstructural constituents, *Journal of Light Metals*. 1 (2001) 85-97.
- [48] K.D. Carlson, Z.P. Lin, C. Beckermann, G. Mazurkevich, M. Schneider, Modeling of Porosity Formation in Aluminium Alloys, 519 (2006) 1699-1706.
- [49] K. Kubo, R.D. Pehlke, Mathematical modeling of porosity formation in solidification, *Metallurgical and Materials Transactions B*. 16 (1985) 359-366.
- [50] Q.G. Wang, P.N. Crepeau, C.J. Davidson, J.R. Griffiths, Oxide films, pores and the fatigue lives of cast aluminum alloys, *Metallurgical and Materials Transactions B*. 37 (2006) 887-895.
- [51] J. Jordon, M. Horstemeyer, N. Yang, J. Major, K. Gall, J. Fan, D. McDowell, Microstructural inclusion influence on fatigue of a cast A356 aluminum alloy, *Metallurgical and Materials Transactions A*. 41 (2010) 356-363.
- [52] J.G. Kaufman, E.L. Rooy, *Aluminum Alloy Castings: Properties, Processes, and Applications*, Asm Intl, 2004.

- [53] L. Yao, S. Cockcroft, J. Zhu, C. Reilly, Modeling of Microporosity Size Distribution in Aluminum Alloy A356, *Metallurgical and Materials Transactions A*. (2011) 1-12.
- [54] A. Reis, Y. Houbaert, Z. Xu, R. Van Tol, A. Santos, J. Duarte, A. Magalhães, Modeling of shrinkage defects during solidification of long and short freezing materials, *J. Mater. Process. Technol.* 202 (2008) 428-434.
- [55] M.F. Ibrahim, E. Samuel, A.M. Samuel, A.M.A. Al-Ahmari, F.H. Samuel, Metallurgical Parameters Controlling the Microstructure and Hardness of Al-Si-Cu-Mg Base Alloys, *Mater Des.* (2010).
- [56] M. Tash, F.H. Samuel, F. Mucciardi, H.W. Doty, Effect of metallurgical parameters on the hardness and microstructural characterization of as-cast and heat-treated 356 and 319 aluminum alloys, *Materials Science and Engineering: A*. 443 (2007) 185-201.
- [57] P. Mohanty, J. Gruzleski, Grain refinement mechanisms of hypoeutectic Al--Si alloys, *Acta materialia*. 44 (1996) 3749-3760.
- [58] A. Greer, A. Bunn, A. Tronche, P. Evans, D. Bristow, Modelling of inoculation of metallic melts: application to grain refinement of aluminium by Al-Ti-B, *Acta Materialia*. 48 (2000) 2823-2835.
- [59] R. I. Mackay, J. Sokolowski, **Experimental observations of dendrite coarsening & Al-Si eutectic growth in progressively quenched structures of Al-Si-Cu casting alloys**, 2 (2008).
- [60] F. Samuel, A. Samuel, P. Ouellet, H. Doty, Effect of Mg and Sr additions on the formation of intermetallics in Al-6 wt pct Si-3.5 wt pct Cu-(0.45) to (0.8) wt pct Fe 319-type alloys, *Metallurgical and Materials Transactions A*. 29 (1998) 2871-2884.
- [61] C. Muojekwu, I. Samarasekera, J. Brimacombe, Heat transfer and microstructure during the early stages of metal solidification, *Metallurgical and Materials Transactions B*. 26 (1995) 361-382.
- [62] J. Wang, P.D. Lee, R.W. Hamilton, M. Li, J. Allison, The kinetics of Fe-rich intermetallic formation in aluminium alloys: In situ observation, *Scr. Mater.* 60 (2009) 516-519.
- [63] J.A. Dantzig, M. Rappaz, *Solidification*, EFPL Press, 2009.
- [64] D.J. Browne, Z. Kovacs, W.U. Mirihanage, Comparison of nucleation and growth mechanisms in alloy solidification to those in metallic glass crystallisation—relevance to modeling, *Transactions of the Indian Institute of Metals*. 62 (2009) 409-412.
- [65] D.A. Porter, K.E. Easterling, *Phase Transformations in Metals and Alloys*, CRC, 1992.

- [66] P. Thevoz, J. Desbiolles, M. Rappaz, Modeling of equiaxed microstructure formation in casting, *Metallurgical and Materials Transactions A*. 20 (1989) 311-322.
- [67] W. Kurz, D.J. Fisher, *Fundamentals of solidification*, Trans Tech Publications Ltd, Trans Tech House, 4711, Aedermansdorf, Switzerland, 1986.244. (1986).
- [68] A. Samuel, F. Samuel, A metallographic study of porosity and fracture behavior in relation to the tensile properties in 319.2 end chill castings, *Metallurgical and Materials Transactions A*. 26 (1995) 2359-2372.
- [69] J. Guo, W. Cao, M. Samonds, The application of integrated computational material engineering (ICME) in metal casting simulation, 33 (2012).
- [70] L. Yao, S. Cockcroft, C. Reilly, J. Zhu, Factors Affecting the Nucleation Kinetics of Microporosity Formation in Aluminum Alloy A356, *Metallurgical and materials transactions.A, Physical metallurgy and materials science*. 43 (2012) 1004-1016.
- [71] A.S.M.M. Handbook, Vol. 11 Failure Analysis and Prevention, ASM Int. (1986).
- [72] K. Mills, *ASM Handbook: Fractography*, Asm Intl, 1987.
- [73] S. Kulkarni, K. Radhakrishna, Prediction of solidification time during solidification of aluminum base alloy castings cast in CO 2-sand mold, *The International Journal of Advanced Manufacturing Technology*. 34 (2007) 1098-1110.
- [74] N.J. Themelis, *Transport and Chemical Rate Phenomena*, Gordon and Breach, 1995.
- [75] C. Hallam, W. Griffiths, A model of the interfacial heat-transfer coefficient for the aluminum gravity die-casting process, *Metallurgical and Materials Transactions B*. 35 (2004) 721-733.
- [76] H. Sehitoglu, T. Smith, X. Qing, H.J. Maier, J.A. Allison, Stress-strain response of a cast 319-T6 aluminum under thermomechanical loading, *Metallurgical and Materials Transactions A*. 31 (2000) 139-151.
- [77] M. Bamberger, B. Weiss, M. Stupel, Heat flow and dendritic arm spacing in chill-cast Al–Si alloys, *Materials science and technology*. 3 (1987) 49-56.
- [78] T.S.P. Kumar, K.N. Prabhu, Heat flux transients at the casting/chill interface during solidification of aluminum base alloys, *Metallurgical and Materials Transactions B*. 22 (1991) 717-727.

- [79] M.A. Gafur, M.N. Haque, K.N. Prabhu, Effect of chill thickness and superheat on casting/chill interfacial heat transfer during solidification of commercially pure aluminium, *J. Mater. Process. Technol.* 133 (2003) 257-265.
- [80] M. Shneider, W. Schaefer, E. Sjolander, S. Seiffeddine, I. Svensson, Simulation of microstructure and mechanical properties of aluminum components during casting and heat treatment, 33 (2012).
- [81] W. Griffiths, A model of the interfacial heat-transfer coefficient during unidirectional solidification of an aluminum alloy, *Metallurgical and Materials Transactions B.* 31 (2000) 285-295.
- [82] S. Kulkarni, K. Radhakrishna, Evaluation of metal–mould interfacial heat transfer during the solidification of aluminium–4.5% copper alloy castings cast in CO₂–sand moulds, *Materials Science-Poland.* 23 (2005) 821-838.
- [83] J.E. Spinelli, I.L. Ferreira, A. Garcia, Evaluation of heat transfer coefficients during upward and downward transient directional solidification of Al–Si alloys, *Structural and Multidisciplinary Optimization.* 31 (2006) 241-248.
- [84] Y. Heichal, S. Chandra, Predicting thermal contact resistance between molten metal droplets and a solid surface, *Journal of heat transfer.* 127 (2005) 1269.
- [85] T. Rajan, K. Narayan Prabhu, R. Pillai, B. Pai, Solidification and casting/mould interfacial heat transfer characteristics of aluminum matrix composites, *Composites Sci. Technol.* 67 (2007) 70-78.
- [86] G. Wang, E. Matthys, On the heat transfer at the interface between a solidifying metal and a solid substrate, *Melt-Spinning, Strip casting, and Slab casting.* TMS Pub., Warrendale, PA. (1996).
- [87] T. Loulou, E. Artyukhin, J. Bardon, Estimation of thermal contact resistance during the first stages of metal solidification process: I—experiment principle and modelisation, *Int. J. Heat Mass Transfer.* 42 (1999) 2119-2127.
- [88] K. Ho, R.D. Pehlke, Metal-mold interfacial heat transfer, *Metallurgical and Materials Transactions B.* 16 (1985) 585-594.
- [89] M. Prates, H. Biloni, Variables affecting the nature of the chill zone, *Metallurgical and Materials Transactions B.* 3 (1972) 1501-1510.
- [90] W. Griffiths, The heat-transfer coefficient during the unidirectional solidification of an Al-Si alloy casting, *Metallurgical and Materials Transactions B.* 30 (1999) 473-482.

- [91] Z. Guo, N. Saunders, E. Hepp, J.P. Schillé, Modelling of Material Properties-A Viable Solution to the Lack of Material Data in Casting Simulation,.
- [92] H.M. Şahin, K. Kocatepe, R. Kayıkcı, N. Akar, Determination of unidirectional heat transfer coefficient during unsteady-state solidification at metal casting–chill interface, Energy conversion and management. 47 (2006) 19-34.
- [93] C.A. Santos, J. Quaresma, A. Garcia, Determination of transient interfacial heat transfer coefficients in chill mold castings, J. Alloys Compounds. 319 (2001) 174-186.
- [94] K. Ho, R. Pehlke, Mechanism of heat transfer at a metal-mold interface, Transactions of the American Foundrymen Society. 92 (1984) 587-598.
- [95] J. Isaac, G. Reddy, G. Sharma, Experimental investigation of the influence of casting parameters on the formation and distribution of air gap during the solidification of castings in metallic molds, Transactions of the American Foundrymen Society. 93 (1985) 29-34.
- [96] F. Chiesa, Measurement of the thermal conductance at the mold/metal interface of permanent molds, AFS Trans. 98 (1990) 193-200.
- [97] C. Kang, Y. Kim, Model experiments for the determination of the heat-transfer coefficient and transition thermal analysis in the direct rolling process, J. Mater. Process. Technol. 84 (1998) 210-224.
- [98] M. Pokorny, C. Monroe, C. Beckermann, L. Bichler, C. Ravindran, Prediction Of Hot Tear Formation In A Magnesium Alloy Permanent Mold Casting, International Journal of Metalcasting. 2 (2008) 41-52.
- [99] K.C. Mills, Recommended Values of Thermophysical Properties for Selected Commercial Alloys, Woodhead Publishing, 2002.